

UNIVERSITY OF OKLAHOMA
GRADUATE COLLEGE

ANALYSIS AND DESIGN OF REFLECTARRAY ANTENNAS
FOR RADAR SYSTEM APPLICATIONS

A DISSERTATION
SUBMITTED TO THE GRADUATE FACULTY
in partial fulfillment of the requirements for the
Degree of
DOCTOR OF PHILOSOPHY

By
YU PAN
Norman, Oklahoma
2014

ANALYSIS AND DESIGN OF REFLECTARRAY ANTENNAS
FOR RADAR SYSTEM APPLICATIONS

A DISSERTATION APPROVED FOR THE
SCHOOL OF ELECTRICAL AND COMPUTER ENGINEERING

BY

Dr. Yan Zhang

Dr. S. Lakshmivaran

Dr. Robert Palmer

Dr. Guifu Zhang

Dr. Jessica Ruyle

©Copyright by YU PAN 2014
All Rights Reserved.

Acknowledgements

I would like to express my sincerest gratitude to my thesis advisor, Professor Yan Zhang. Without his inspiration, guidance, support and encouragement this thesis would not have been possible.

I am also grateful to my other committee members: Professor S. Lakshmi-varahan, Professor Robert Palmer, Professor Guifu Zhang, and Professor Jessica Ruyle.

I would like to thank the Advanced Radar Research Center (ARRC) at University of Oklahoma, its former director Professor Robert Palmer, and the support team at the ARRC, especially Redmond Kelley and John Meier, for making an excellent research environment, which I enjoyed throughout my Ph.D. research at the ARRC and OU.

I would like to thank Dr. Zhengzheng Li, Dr. Qing Cao, Dr. Shang Wang and Dr. Yuezhou Li for their help in the early stage of the thesis work. I would also like to thank Xining Yu for his technical assistance during the antenna measurements. I have also enjoyed many discussions with Dr. Shaya Karimkashi, which have been very fruitful.

Special thanks go to the following persons for the discussions and help in this dissertation: Dr. Fanxing Kong, Dr. Yinguang Li, Dr. Lei Lei, Hernan Suarez, Sudantha Perera, Jingxiao Cai, Ramesh Nepal and Zaidi Zhu.

Finally, I would like to thank my parents, my wife Wenjie, and my son Norman, and my whole family for their constant love and support.

Contents

Acknowledgements	iv
List Of Tables	viii
List Of Figures	ix
Abstract	xiii
1 Introduction	1
1.1 Introduction of Antenna	1
1.2 Introduction of Reflectarray	2
1.3 Types of Reflectarrays	5
1.3.1 Passive Reflectarrays	5
1.3.2 Reconfigurable Reflectarray	6
1.3.3 Shaped Beam and Multi-Beam Reflectarrays	8
1.4 Dissertation Organization	9
2 Broadband Low-cost Reflectarray for Multi-mission Radar Ap- plications	12
2.1 Introduction	12
2.2 Bandwidth Limitation of Reflectarray	14
2.2.1 Bandwidth Limitation of Microstrip Element	16
2.2.2 Bandwidth Limitation by Differential Spatial Phase Delay	20
2.3 Broadband, Single Layer Element Design	26

2.4	Antenna Array Design	33
2.4.1	Horn Pattern Characterization	35
2.4.2	Reflectarray Efficiency	37
2.4.3	Reflectarray Phase Distribution	38
2.5	Antenna Array Simulation	40
2.6	Antenna Array Measurements	45
2.7	Conclusion	47
3	Analysis of Blockage Effects in a Center-fed Reflectarray	48
3.1	Introduction	48
3.2	Analysis Of Blockage Effects	49
3.2.1	Zero Blockage	49
3.2.2	Data-link Blockage	51
3.2.3	Reflectarray-located Blockage	51
3.2.4	Obstacle-located Blockage	52
3.2.5	Integrated Blockage	52
3.3	Simulation and Measurement Results	52
3.4	Reflectarray with Tilted Main Beam	59
3.5	Conclusion	63
4	A Reflectarray Design with Reduced Cross-Polarization for Polarimetric Radar	64
4.1	Introduction	64
4.2	Definitions of Cross-Polarization	68
4.3	Element Design	71
4.4	Surface Current Simulation	74
4.5	Cross-Polarization Suppression Using Gapped Ring Elements . . .	77

4.6	Reflectarray Design Example	80
4.7	Conclusion	88
5	An X/Ku Dual-band Reflectarray Design with Cosecant Squared Shaped Beam	89
5.1	Introduction	89
5.2	Unit Cell Design	92
5.3	Coupling Effects	95
5.4	Beam Synthesis	100
5.4.1	Phase-Only Synthesis of Reflectarray	100
5.4.2	An Analytical Technique for Cosecant Squared Beam Shaping	103
5.5	Array Design and Simulation	104
5.6	Array Measurements	108
5.6.1	X-Band Measurement Results for the Dual-Layer Reflectarray	108
5.6.2	Ku-Band Measurement Results for the Dual-Layer Reflec- tarray	112
5.7	Conclusion	115
6	Conclusions	116
6.1	Summary	116
6.2	Recommendations for Future Research	118
	Reference List	121
	Appendix A	
	List of Acronyms and Abbreviations	133

List Of Tables

2.1	Dimensions and parameters of the broadband patch element design	18
2.2	Dimensions and parameters of the reflectarray	28
3.1	Summary of the simulation and measurement results for blockage analysis	58
4.1	Dimensions and parameters of the low cross-polarization double-ring reflectarray	72
4.2	Simulated cross-polarization level of the two reflectarrays with non-gapped and gapped double ring elements	84
5.1	Dimensions and parameters of the X-band and Ka-band unit cell design	94

List Of Figures

1.1	Antenna structures of the reflector and reflectarray	3
2.1	1 dB gain bandwidth of antenna	15
2.2	S parameters of narrow band and broadband microstrip patch antenna	17
2.3	Configuration of the stacked dual-layer microstrip patch antenna .	19
2.4	Measurement results of the narrow band dual-polarized patch antenna	21
2.5	Measurement results of the broadband stacked patch antenna . .	22
2.6	Geometry for the reflectarray for phase delay calculation	23
2.7	Bandwidth limitation of reflectarray	25
2.8	Broadband single layer reflectarray: element configuration	27
2.9	Waveguide simulation (WGS) approach for reflection phase calculation	30
2.10	Broadband single layer reflectarray: reflection phase	31
2.11	Phase curve comparison between WGS and MS methods	32
2.12	Simulated reflection phase curves for different incidence angle . .	34
2.13	The coordinate system used in the reflectarray design	35
2.14	Feed horn pattern simplified using $\cos^q(\theta)$ function	36
2.15	Reflectarray efficiency	38
2.16	Reflectarray geometry for phase distribution calculation	39
2.17	Phase distribution on the broadband single layer reflectarray . . .	40
2.18	Reflection phases of the ring element obtained in HFSS and CST	41

2.19	Simulated normalized radiation pattern at 13.325 GHz	43
2.20	Fabricated broadband single layer reflectarray	45
2.21	Reflectarray measurement setup for E-plane cut	46
2.22	Measured normalized radiation patterns at 13.325 GHz	47
3.1	Different schemes for modeling blockage effects in a reflectarray .	50
3.2	Simulation results using the blockage analysis approaches	53
3.3	Simulation results using the blockage analysis approaches	54
3.4	Test setup of the reflectarray with a wood and acrylic structure .	55
3.5	Comparison between the simulation and measurement results . . .	57
3.6	Phase distribution on the reflectarray with a tilted beam	59
3.7	Prototype of the reflectarray with a tilted beam	60
3.8	Simulated and measured radiation patterns of the reflectarray with a tilted beam at 12.5 GHz and 13.325 GHz	61
3.9	Simulated and measured radiation patterns of the reflectarray with a tilted beam at 13.5 GHz	62
3.10	Measured wideband gain of the reflectarray with a tilted beam . .	63
4.1	Various reflectarray elements	65
4.2	Coordinate systems for cross polarization definitions	67
4.3	Double-ring element design for lower cross-polarization	71
4.4	Simulated reflection phases of the double-ring element	73
4.5	Simulated reflection phases of the double-ring element with differ- ent radiuses ratio I/O	73
4.6	Simulated surface currents of the non-gapped double-ring elements with periodic boundary conditions	75
4.7	Gaps are cut on the rings to change the directions of surface currents.	77

4.8	Simulated surface currents of the new gapped double-ring elements with PBC	79
4.9	Comparison of the simulated radiation patterns of the 2 by 2 reflectarrays with non-gapped and gapped double-ring elements . .	81
4.10	Simulated farfield radiation patterns of the full size reflectarrays with non-gapped and gapped double ring elements	83
4.11	Fabricated reflectarray with gapped double-ring elements	84
4.12	Measured farfield radiation patterns of the full size reflectarrays with non-gapped and gapped double ring elements	86
4.13	Measured normalized cross-polarization level at broadside direction (E-plane).	87
5.1	Schematic and geometry of the dual-band reflectarray unit cell . .	93
5.2	The surface current density on the dual-band reflectarray unit cells	96
5.3	The unit cell of the Ku-band double ring are simulated at 15 GHz with presence of X-band cross-dipole	97
5.4	Simulated reflection phases of the X-band cross-dipole element at 10 GHz and Ku-band double-ring element at 15 GHz	99
5.5	The reflection phases of the Ku-band double ring are simulated at 15 GHz with presence of X-band cross-dipole of different dipole lengths	100
5.6	Synthesized phase distribution and pattern for the X-band 15×1 linear array	105
5.7	Synthesized phase distribution and pattern for the Ku-band 32×1 linear array	106

5.8	Required phase distributions on the dual-layer reflectarray to generate the desired cosecant squared shaped beam for X-band cross-dipole array and Ku-band double-ring array	107
5.9	Topology of the dual-layer dual-frequency reflectarray	109
5.10	Simulated radiation patterns of the dual-layer reflectarray at X-band and Ku-band	110
5.11	Simulated 3D cosecant squared shaped beam of the dual-layer reflectarray at Ku-band	111
5.12	Photograph of the dual-layer prototype reflectarray	111
5.13	Measured radiation patterns at X-band for the dual-layer reflectarray	113
5.14	Measured radiation patterns at Ku-band for the dual-layer reflectarray	114
6.1	Proposed reflectarray unit cell design using liquid-tunable technology	120
6.2	The tube is filled with liquid metal slug to change the effective capacitance of the unit cell	121

Abstract

In recent years reflectarray has received more and more attention and it has been considered as a suitable candidate to replace the traditional reflectors due to its high-gain, low profile and low cost features. Reflectarray also eliminates the lossy feed network and costly transmitting and receiving modules when comparing with phased array antenna. It is desired to implement these functionalities with simple and effective techniques.

Narrow bandwidth is the main issue which restricts the applications of the microstrip antennas, including the microstrip reflectarray. A broadband single-layer reflectarray is introduced as the solutions to the issue of narrow bandwidth. A combination of two types of element configurations, including (i) ring elements and (ii) circular patch elements with ring boundary, enlarges the reflection phase range to more than 360° and thus enables the broadband operation of reflectarray.

Blockage effect is another issue with the center-fed reflectarray. Certain obstacles, such as the feed horn, subreflector, and their supports, exist in reflectarray antennas. When these obstacles are in front of the reflectarray, the reflected wave is blocked, and the feed's absorption also weakens the reflected power. An accurate prediction of this blockage effect in reflectarray design is essential. Five modeling schemes to account for the blockage effects in a reflectarray are described and also compared in terms of simulation time and consumed computing resource. In addition, another reflectarray with mainbeam direction steered 18° off broadside is also introduced to mitigate the blockage effect.

Low cross-polarization performance is required for some reflectarray applications. For example, in dual-polarized weather radar the precipitation detection

relies on complete isolation of orthogonal components of the fields, and thus negligible levels of cross-polarized radiation along the beam axis need to be maintained. A reflectarray design with suppressed cross-polarization is introduced in this dissertation. The directions of the surface currents can be changed by cutting gaps on the double-ring elements, so that the co-polar components of the surface currents enhance each other while the cross-polar components cancel each other, and thus a low cross-polarization level can be achieved.

An X/Ku dual-band microstrip reflectarray with cosecant squared shaped beams has also been developed. The two operation frequency bands, 10 GHz and 15 GHz, are very close to each other. Thus the radiation interference between the two bands is taken into consideration and design is optimized to suppress the interference as much as possible. A dual-layer structure with cross-dipoles on the top layer and double-rings on the lower layer is adopted to suppress the interband couplings. Moreover, the dual-band elements are arranged in an interleaved manner in order to minimize element blockage. In addition, a phase-only synthesis technique is also introduced to obtain the two cosecant squared shaped beams for each operation frequency band.

In summary, this dissertation presents a series of new research developments for reflectarray antennas. The results should have many applications for the modern wireless communications and radar systems.

Chapter 1

Introduction

1.1 Introduction of Antenna

An antenna is defined by Webster's Dictionary as "a usually metallic device (as a rod or wire) for radiating or receiving radio waves". The IEEE Standard Definitions of Terms for Antennas defines the antenna as "a means for radiating or receiving radio waves" [1]. Antennas are essential parts in wireless communication systems. They have been designed in all kinds of shapes and sizes in many applications, from civilian systems to military systems, such as personal communication, mobile base stations, satellite communication and radar detection.

In general, antennas are frequency-dependent devices. Antennas in each application mentioned above have their designed operating frequency band. Only within the specific frequency band, the antenna radiates or receives signals. Many recent antenna systems require a wide bandwidth or even multi-band operability, to enable the transmitting or receiving at different frequencies for a single antenna design.

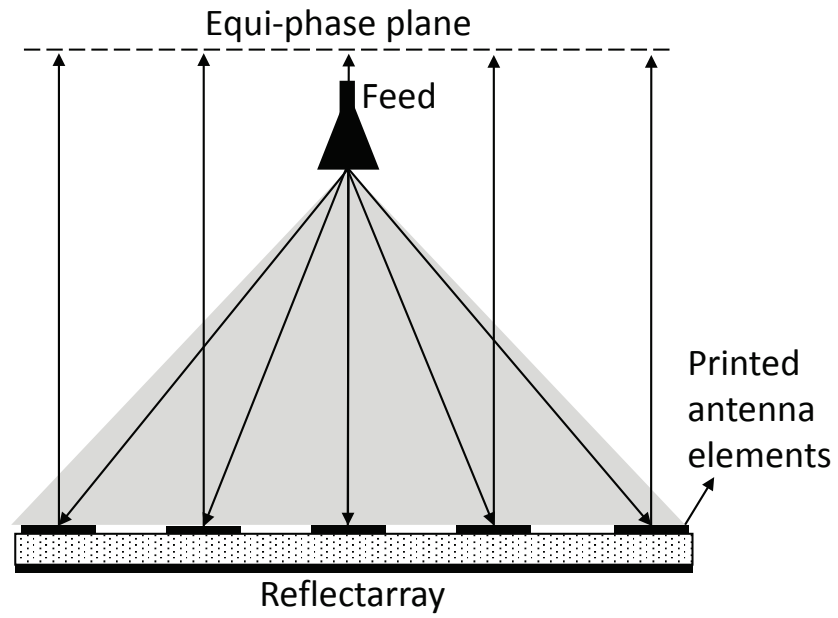
The directivity and gain describe an antenna's capability of radiating power at a certain direction. The directivity of an antenna has been defined as "the ratio of the radiation intensity in a given direction from the antenna to the radiation intensity averaged over all directions" [2]. In reality, the total radiation power over all directions is not known, or difficult to access. Therefore, a second

function *gain* is introduced. The gain G resembles the directivity, except for the total radiated power that has been replaced by the total accepted power.

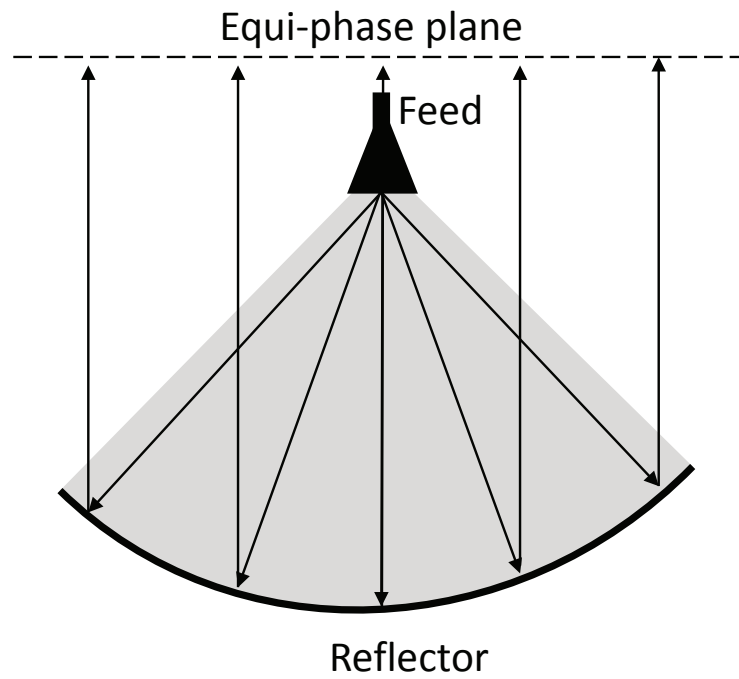
In many applications, such as satellite communication or radar detection, a high gain antenna is desired to focus the radiation energy in some directions and suppress it in others, in order to maximize the signal at the receiver. Generally, increasing the illuminated aperture and forming arrays of individual radiators are the two approaches to achieve high gain antennas. A good design of the antenna can relax system requirements and improve overall system performance.

1.2 Introduction of Reflectarray

The main focus of this thesis research will be analysis and design of reflectarray antennas. A reflectarray consists of a planar array of printed radiating elements and a centered or offset illuminating feed source as shown in Figure 1.1 (a). The concept of reflectarray came from the operation of the conventional parabolic reflector. As shown in Figure 1.1 (b), with a feed placed at its focal point, the reflector antenna utilizes its unique curvature to reflect and form a equi-phase front plane, where a focused beam or a contour beam can be formed [3]. Similarly, printed radiating elements on a reflectarray surface can be predesigned with electrical phases, and when the feed antenna spatially illuminates the reflectarray, the elements will re-radiate and scatter the incident field with the specific electrical phases to form a planar phase front in the far-field distance [4]. In other words, the curvature design in parabolic reflector is transformed to the predesigned phases of all elements on the reflectarray, in order to compensate path differences between the feed and array surface.



(a)



(b)

Figure 1.1: Antenna structures of (a) reflectarray and (b) reflector.

The reflectarray antenna was first implemented in 1962 by Malech, and its comprehensive description was published by Berry et al. in 1963 [5, 6]. They constructed a reflecting surface composed of arrays of elementary antennas, in order to combine the features of the reflector and array type antennas. Berry et al. used waveguide with shorted back as the reflectarray elements, and the required phase shift for each element is achieved by adjusting the position of the short circuit in the waveguide.

In last 30 years, with the advent of inexpensive, faster and larger-memory computers, efficient software tools, and improved microstrip fabrication techniques, the reflectarray technology has been experiencing great advancement in terms of both the type of elements and the analysis methods. The bulky structure of the waveguide reflectarray was eliminated by the adoption of microstrip elements by Malagisi in 1978 [7]. In this design, microstrip patches loaded with stubs of varied lengths were used for adjusting the reflection phase, until today this element type is still a popular design option and is being investigated and improved by researchers and engineers.

Another reflectarray design was conceived by Phelan in 1977 [8]. This design used 4-arm spiralphase elements, and switching diodes were introduced in the spiral elements to control the phase of reflected circularly polarized waves.

The microstrip reflectarrays have many advantages compared to the parabolic reflectors and electronically scanned phased array antennas. First, the microstrip reflectarrays have small size, lightweight, compact profile and low cost. Second, it not only eliminates the loss of the complex feed network in the phased array, but the transmit/receive modules are also not required and thus the cost is further lowered.

In reflectarray, phase control of single element is the key feature of the antenna design. In the past years, many designs have been developed to achieve more flexible, broadband and reconfigurable phase control. Basically, the elements' phase control schemes define the types of reflectarray. In following sections, different types of reflectarray element design will be introduced. The new features of reflectarrays, such as reconfigurable reflectarray and reflectarrays with contoured or shaped beams will also be discussed in this chapter.

1.3 Types of Reflectarrays

Generally, the reflectarrays can be classified as passive reflectarrays, reconfigurable reflectarrays and reflectarrays with shaped beam or multi-beam. However, this classification is not so distinct and some reflectarrays can be classified into multiple classes.

1.3.1 Passive Reflectarrays

Most of the initially developed microstrip reflectarrays consisted of only passive cells. To realize the phase control, different phase shifting mechanisms were developed, including variable stub length, variable patch size or variable rotation angle. In a reflectarray with variable stub length, for example, a microstrip patch antennas are loaded with open-circuit stubs and phase shifting is achieved by changing the length of the stubs connected to the edge [9]. Aperture coupled microstrip patch antenna is also used as reflectarray elements, for which the reflection phase is determined from the length of the open circuited transmission line at the feed substrate which is coupled between the patch antenna and the antenna substrate through the aperture on the ground plane [10–12].

Another common type of passive reflectarray is the reflectarray with variable-sized microstrip patches. This design utilized varying patch sizes for reflection phase control, instead of varying stub lengths. Therefore, the spurious radiation from the microstrip stub can be eliminated in the element design with variable resonant lengths. The element type of this design can be patches (rectangular or circular) [13, 14], crossed dipoles [15] or rings [14, 16]. However, the narrowband performance of the microstrip patch is concerned in variable-sized element design. In order to overcome the inherent narrowband constraint of microstrip patch antenna, stacked element configuration and multi-layered array configuration were designed for reflectarray for wideband or dual-band applications [12, 17–20].

Elements with variable rotation angles were also used to introduce phase shifting on circularly polarized reflectarrays. The phase of the co-polarized wave upon circularly polarized wave incidence is linearly dependent on the element rotation angles [8]. Different element types, including rotating patches [21], dipoles [22] and gapped-ring elements [19, 23, 24] were designed to utilize this principles.

1.3.2 Reconfigurable Reflectarray

Recently, the reconfigurable reflectarrays have gained a lot of research interest. They have the advantage of being able to steer the beam electronically. Several techniques, such as varactor diodes, PIN diodes, Micro-electro-mechanical-systems (MEMS) devices and tunable dielectrics were employed to provide the phase shifting capability of the array elements. Designs employing the varactor diodes [25–27], PIN diodes switches [28] and the combinations of both [29] have been proposed in recent years. By loading a microstrip patch with an

electronically-controlled varactor, its resonant frequency can be changed, the usable frequency range of the patch element can be extended. The resultant frequency agility, when applied to the reflectarray, can be used to change the phase response of each element, thus the reflectarray can generate steered beams electronically [26]. A reflectarray with broadband unit cell using double square rings and four varactors is designed in [30], which exhibits a over 380° phase agility and can scan up to 40° off broadside.

According to the reported results of the reconfigurable reflectarray, a reflectarray using Radio Frequency (RF) MEMS technology is believed to be the most promising solution in terms of large power handling, high linearity and low drive power consumption [31,32]. To achieve reconfigurability, the reflectarray elements are loaded with variable MEMS capacitors, and the resonance of such elements shifts towards lower frequencies with increasing capacitances values. Therefore, by controlling the MEMS capacitance, the reflection phase of the element at a given frequency can be dynamically reconfigured. For example, a reflectarray design reported in [33] provides a range of phase tuning of approximate 190° . In order to overcome the limitations of dynamic phase range and bandwidth, a monolithic MEMS-based reflectarray cell has been developed in [31], which incorporates 5-bit digital control, and allows reconfiguration of the reflection phase over the 360° range. However, the design requires ten MEMS devices for one unit cell, the cost concern shall be taken into account if the design is implemented for a larger array.

Nematic liquid crystal (LC) and ferroelectric film can also be used as the phase shifters in a reflectarray, which exploit the voltage controlled dielectric anisotropy property of the materials [34–36]. Advantages of the phase shifting based on this LC approach include low cost, simplicity of the biasing arrangement, ease of

fabrication and integration, and unlike semiconductor devices, no limitation is imposed on the upper operating frequency [34]. Moreover, the switching speed is believed to be faster due to the reduction in the physical thickness of the LC layer [34]. For example, in [34] by applying a low frequency AC bias voltage of 10 V, a 165° phase range with a loss of 4.5 - 6.4 dB at 102 GHz and a 130° phase range with a loss of 4.3-7 dB at 130 GHz were obtained. However, to design a fully operational beam scanning reflectarray, two critical characteristics of this LC phase shifter need further improvement, including the phase range and the reflection loss. Besides LC and ferroelectric film, a liquid-tunable unit cell design was also proposed to realize the phase control operation [37,38]. The structure of the liquid-tunable unit cell consists of a capillary tube inserted in the substrate layer, and by moving the liquid metal slugs within the capillary tubes, the phase response of the unit cell can be tuned.

1.3.3 Shaped Beam and Multi-Beam Reflectarrays

Reflectarrays can also be designed with a shaped beam to cover a predefined region and they differ from the pencil beam reflectarrays, which only cover specific areas. In reflectarrays, the amplitude of the reflected field at each element is determined by the radiation field of the feed antenna. Once the feed source and the feed location is determined, the amplitude of the reflected field on the element surface is fixed. Hence, only the phase of the reflective field can be changed to synthesize a shaped beam. The phase-only synthesis method based on “Intersection Approach” is used for the contoured beam reflectarray with a large number of elements for Direct Broadcast Satellite (DSB) applications [39–41]. A synthesis method that uses the modified Taylor expressions for circular reflectarray to provide good non- Φ -symmetric patterns is also proposed [42].

Moreover, the reflectarrays can also be designed to produce simultaneous multiple beams using single or multiple feeds. A multi-beam functionality for the DSB application for the coverage of South America and the Florida regions with one feed was realized in [43]. In [41], a dual-polarization reflectarray with two independent beams, one for each H or V polarization, was designed to replace a conventional reflector in a spacing satellite application. The designed reflectarray can generate a contoured beam for H-polarization for an European coverage, and a pencil beam for V-polarization to illuminate the East Coast in North America. Another example for multi-beam reflectarray is the one presented in [44], which uses multiple feeds to generate three simultaneous shaped beam for Local Multipoint Distribution Service (LMDS) application.

1.4 Dissertation Organization

The contents covered in this dissertation include a single-layer wide band reflectarray, reflectarray performance improvement, including the blockage estimation and mitigation and the cross-polarization suppression, and a dual-band reflectarray with cosecant squared shaped beam. The rest of the dissertation is organized as follows.

Chapter 2 presents the design of a broadband, low-cost single-layer reflectarray. The basic operation mechanism of the reflectarray is briefly introduced. The narrow bandwidth behavior of the microstrip reflectarray is discussed. A novel method of using two types of elements to increase the reflection phase variation range is introduced.

In Chapter 3, the blockage effects in a center-fed reflectarray, as a possible source of higher sidelobe level in Chapter 2, will be studied. The effect of the

blockage from feed and support structure and the blockage modeling schemes will first be discussed. The radiation patterns of a center-fed reflectarray using different modeling schemes will then be compared, especially on the sidelobe level, beamwidth and cross-polarization level, the three critical measures of antenna radiation patterns. Moreover, other factors, such as subreflectors and support struts, is also included to further improve the accuracies of predictions. Finally, the reflectarray with a tilted main beam is proposed as a solution to mitigate the blockage effect.

In Chapter 4, an effective method for cross-polarization suppression in reflectarray is proposed and investigated. Changing the directions of surface current on antenna elements is found to be effective on suppressing the cross-polarization components of the radiated fields. A reflectarray design using gapped double-ring elements is proposed. With the gapped double-ring design, the surface currents on the inner ring and outer ring will be enhanced at the co-polarization radiation direction and also cancel each other at cross-polarization radiation, resulting in a low cross-polarization level.

Chapter 5 introduces a design of a dual-layer, dual-frequency reflectarray antenna with cosecant squared shaped beams. The designed reflectarray can be potentially used in Ground-Based Sense and Avoid (GBSAA) radars. The element design of each operation frequency will be presented first. The proposed cross-dipole and double-ring element designs, which are arranged in an interleaved manner, are optimized to minimize the blockage of the incident waves. Then the coupling effects between the two close operational bands are investigated. The phase-only synthesis method to generate the desired shaped beams and the implementation for an array design are discussed. Finally, the measured reflectarray performances are discussed and compared with simulation results.

Finally, a summary of the research accomplishments of this dissertation and recommendations for further studies are provided in Chapter 6.

Chapter 2

Broadband Low-cost Reflectarray for Multi-mission Radar Applications

2.1 Introduction

Recently, multi-functional phased array radars (MPAR) has received wide-spread attention in the radar community. Currently, different types of radars are in operation to provide weather and aircraft surveillance, and each radar type is dedicated to a single mission. To continue to provide multiple services and reduce the cost of radar network, the MPAR project was established since 2003. With the single network of MPAR, it is possible to reduce the total number of radars by approximately one-third, which would provide significant long-term cost savings [45]. Also, the advanced capabilities of the MPAR include the electronic steering with rapid scanning and adaptable control, which would lead to accurate precipitation estimation, improved weather forecasts as well as enhanced aircraft surveillance [45, 46].

Cost and complexity of the phased array antennas are one of the biggest risks when transforming a traditional reflector-dish antenna based radar system to multi-functional, array antenna based systems. Multiple efforts have been conducted on the MPAR project, including the cylindrical polarimetric phased-array radar (CPPAR) developed by the Advanced Radar Research Center of the University of Oklahoma [47–51]. CPPAR is a small-scale proof of concept

demonstrator capable of producing polarimetric phased array measurements of weather. It is a solution for cost-effective risk mitigation for the development of the future MPAR antenna array system.

For the phased array antenna, the possible configurations include linear array, regular planar array, circular and cylindrical array. A linear array operates with one degree of freedom. The regular planar array usually contains microstrip feed network, which is complex and lossy. The cylindrical array design [50] used stacked-patch radiating elements for a wide bandwidth (2.7 - 3.1 GHz). A dual strip-line series feed with aperture coupling is used to enable the frequency steering of the elevation beam. Strip-line feeds are also well isolated to achieve < -30 dB cross-polarization levels. Comparing to the dual-polarized phased array antenna with individual transmit/receive (TR) modules, the frequency steering array benefits a massive reduction in the cost of the backend electronics. However, the problem of relying on commutative scanning for azimuth and frequency scanning for elevation cannot be ignored for the multi-missions.

Another possible candidate for future array antenna is the reflectarray antenna. The concept of reflectarray antenna has attracted significant research interest as it offers a potentially alternative solution to both reflector antenna and traditional antenna arrays. The reflectarray combines some of the best features of parabolic reflectors and the conventional antenna arrays. It has a low physical profile and reduced fabrication costs compared to conventional parabolic reflector as well as the cylindrical array antenna. It also eliminates the complexities and losses associated with beam-forming networks and expensive TR modules of phased array antennas [4]. It is also possible to scan the main beam with phase-synthesized patterns.

In a reflectarray, the individual elements are designed to scatter the incident field with a proper phase required to form a planar phase front. The phase control at each element is achieved by using several methods. One of the favorable methods is to use variable-sized patches [13], rings [14] or dipoles [52]. Patches loaded with stub [9] and rings with variable rotation angles [21] are also implemented for phase adjustment. Variable-sized elements are usually preferable in reflectarray due to simplicity. However, the maximum range of phase variation that can be achieved is on the order of 330° for thickness smaller than a tenth of wavelength [4]. This intrinsic narrow bandwidth behavior of microstrip element is the main reason of the narrow bandwidth performance of the reflectarray. Another factor limiting the bandwidth performance of a microstrip reflectarray is the differential spatial phase delay resulting from different path lengths of the incident rays from the feed to each reflectarray element and is the most restrictive in the case of large-sized reflectarrays [53]. Although this can be solved by stacking double and triple layers of patches of different sizes [12, 18], multi-layer configurations are costly and difficult to be manufactured. In this chapter, a broadband low-cost single-layer reflectarray design will be presented and a novel method of using two types of elements to increase the phase variation range [54] will be introduced.

2.2 Bandwidth Limitation of Reflectarray

Bandwidth is a fundamental antenna parameter, which describes the range of frequencies within which the antenna can properly radiate or receive energy. Usually the antenna bandwidth refers to the range of frequencies where the pattern or gain are within an acceptable value of those at the center frequency [2]. The

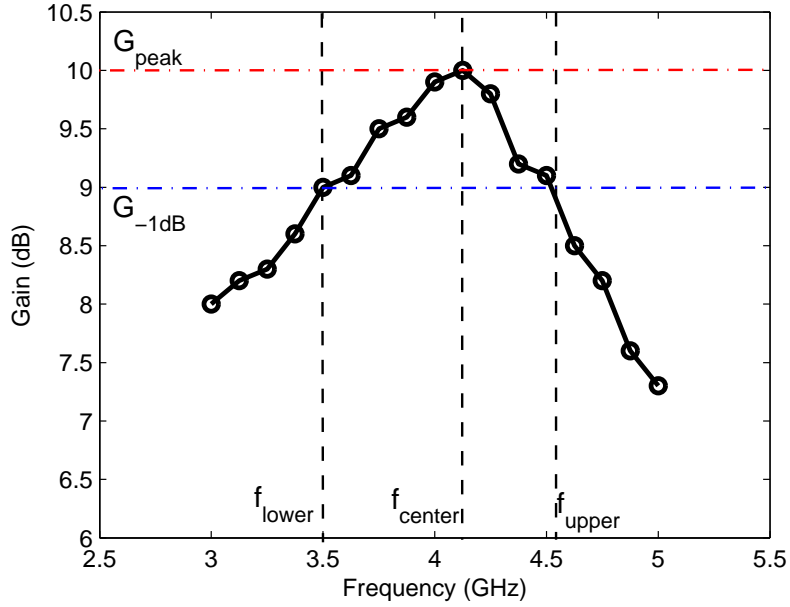


Figure 2.1: 1 dB gain bandwidth of an antenna.

bandwidth is usually expressed as the percentage of the frequency difference over the center frequency of the bandwidth:

$$\begin{cases} BW_{narrowband} = \frac{f_{upper} - f_{lower}}{f_{center}} \\ BW_{broadband} = \frac{f_{upper}}{f_{lower}} \end{cases} \quad (2.1)$$

The 1 dB gain bandwidth is usually used as the standard antenna bandwidth. It is the frequency bandwidth change when antenna gain drops from peak to -1 dB lower, as depicted in Figure 2.1.

Antennas with a BW of **20%** or more are usually referred to as broadband antennas. Some common types of broadband antennas are bowtie, biconical and blade dipole antennas. For common horn and spiral antennas, typically the BW are larger than **100%**. Those antennas with a bandwidth greater than **50%** are referred to as ultra-wideband antennas. The microstrip patch antennas are

notoriously narrowband; the bandwidth of rectangular microstrip antennas are typically 3% [53].

A reflectarray is a flat microstrip array antenna that can be mounted onto the supporting structure with a low cost and without significant additional mass. While the reflectarray antenna has many advantage over conventional parabolic reflectors and has already found applications in satellite communications, space exploration, radar and remote sensing [4], the printed microstrip reflectarray suffers from one major shortcoming which is their limited bandwidths which are no match to that of a parabolic reflector. It is often stated that the bandwidth of a microstrip reflectarray is limited primarily by two factors: the bandwidth of the microstrip element, and the differential spatial phase delay over the surface of the flat reflector [4, 6, 18, 53, 55, 56]. Those two factors will be discussed in following sections, respectively.

2.2.1 Bandwidth Limitation of Microstrip Element

Microstrip antennas have been applied in many communication applications such as aircraft, satellite and radars. Microstrip antennas have many attractive features of low profile, light weight, conformability to planar and nonplanar surfaces, easy and inexpensive fabrication using modern printed-circuit technology [2, 57]. However, one major operational disadvantage of microstrip antennas is their narrow bandwidth, which is typically only a fraction of a percent or at most a few percents. An explanation of the inherent narrow bandwidth behavior of microstrip antennas is provided by the well known supergain concepts by Chu [58], which related antenna size to its bandwidth; the microstrip antenna occupies

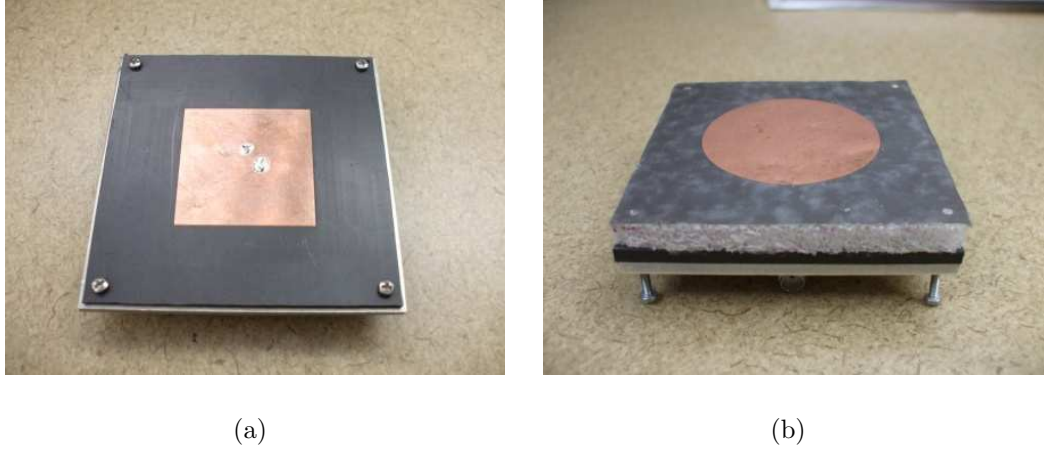


Figure 2.2: The individual S-band, probe-fed microstrip patch antenna element designs. (a): narrow band element design. (b): stacked two-layer broadband element design.

less volume (especially when thin substrates are desired for some compact antenna designs) and hence gives less bandwidth comparing to the cavity backed antennas [59].

Many significant advancements in improving the bandwidth of microstrip antennas have been proposed [60–66], such as using gap-coupled parasitic patches, as well as stacked two-layer or even three-layer patches. We have designed a dual-polarization dual-layer broadband microstrip antenna elements for the reconfigurable and scalable TR module for the MPAR concept [48].

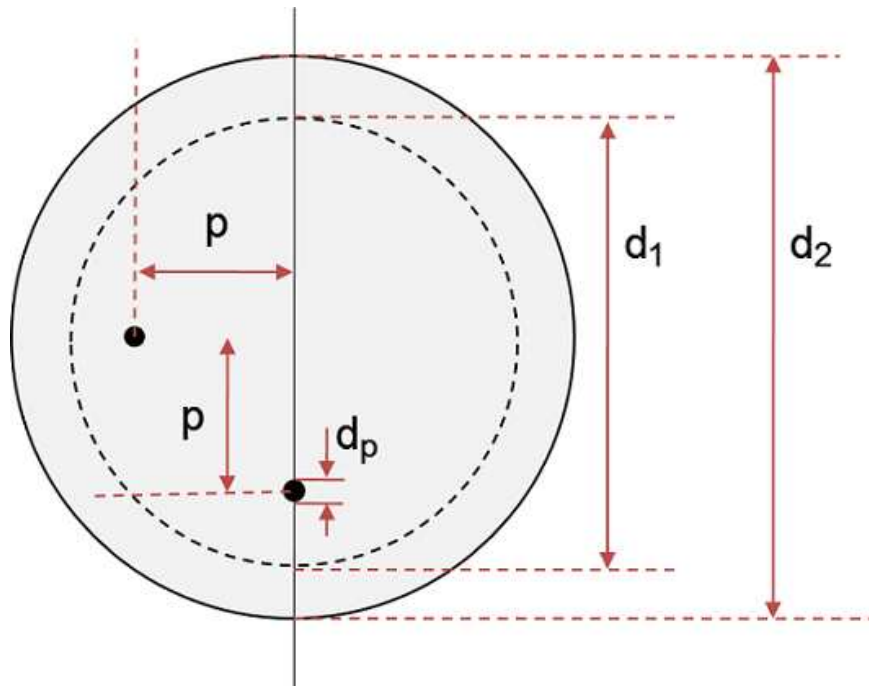
For the antenna used in the TR module, two versions of square patch element are designed and fabricated. One is a narrow band square patch resonating at 2.705 GHz (the operating frequency of a dual-polarized KOUN radar), the other is a broadband element with circular patch shape, designed for a maximized bandwidth in the 2.7-2.9 GHz frequencies. These two antenna elements are shown in Figure 2.2. Both top and bottom substrate layers are based on RO5880 materials.

Table 2.1: Dimensions and parameters of the broadband element design

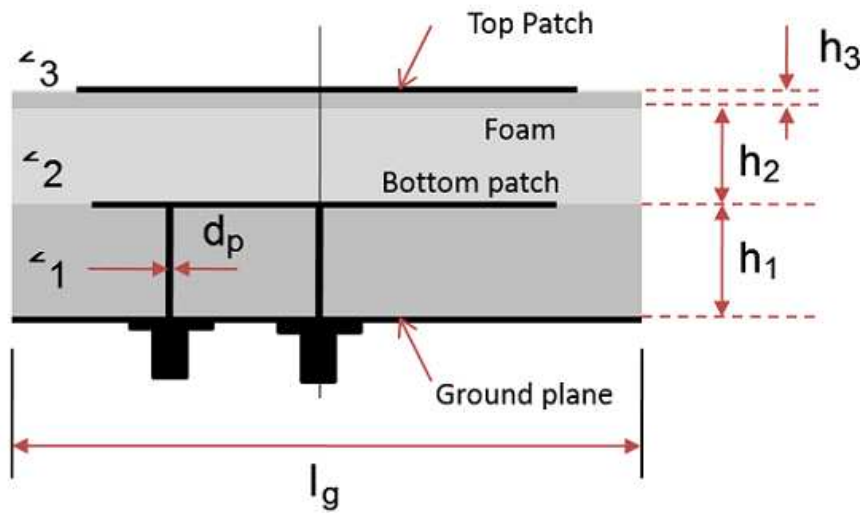
Parameter	Definition	Value
f_c	Center frequency	2.705 GHz
ϵ_1	Relative permittivity of the bottom substrate	2.2
ϵ_2	Relative permittivity of the air/foam layer	1.03
ϵ_3	Relative permittivity of the top substrate	2.2
d_1	Bottom patch diameter	40.71 mm
d_2	Top patch diameter	43.16 mm
p	Feed pin offset	16.83 mm
h_1	Height of the bottom substrate	3.18 mm
h_2	Height of the air/foam layer	6.67 mm
d_p	Feed pin diameter	1.3 mm
l_g	substrate length and width	69.53 mm

The top patch is fabricated on RO5880 with 5 mil thickness, while bottom patch is fabricated on RO5880 with 125 mil thickness. For the broadband element design, a layer of Styrofoam with custom cut was used between the top layer and bottom layer to enhance the broadband performance. The configuration of the broadband element is shown in Figure 2.3 and the parameters and dimensions are given in Table 2.1.

The measured return loss of the two patch antennas are shown in Figure 2.4 and 2.5, respectively. From the return loss results we can easily calculate the



(a)



(b)

Figure 2.3: Configuration of the broadband element design. (a) top view. (b) side view.

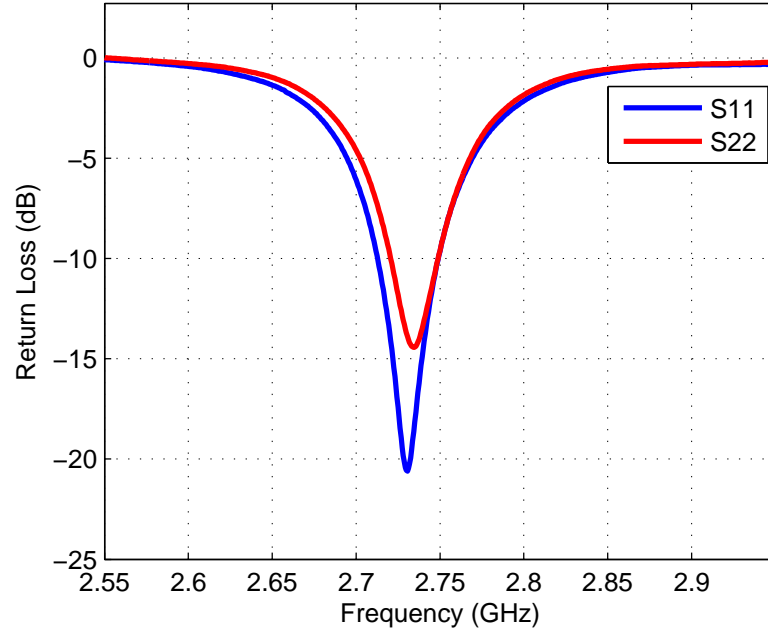
impedance bandwidth of an antenna, which is the power delivered to the antenna greater than or equal to **90%** of the available power. When the power reflection coefficient \mathbf{S}_{11} is -10 dB, it represents **90%** of the available power to the antenna is being sent to antenna, assuming the line impedance matches well with the generator impedance (usually **50Ω**). For the stacked circular patch antenna, larger than 300 MHz usable frequency range is achieved at the 10 cm wavelength band of operational weather radars, which corresponds to a fractional bandwidth **11.11%**, while the single layer patch antenna only gives a very narrow bandwidth about **1.56%**. Therefore, by stacking multiple layers space, a multiresonant behavior is obtained between the layers and the resonant frequency range is increased. This method has also been applied in reflectarray for bandwidth improvement, as demonstrated in [12,18]. The details of this method in reflectarray will be discussed in later sections of this chapter.

2.2.2 Bandwidth Limitation by Differential Spatial Phase Delay

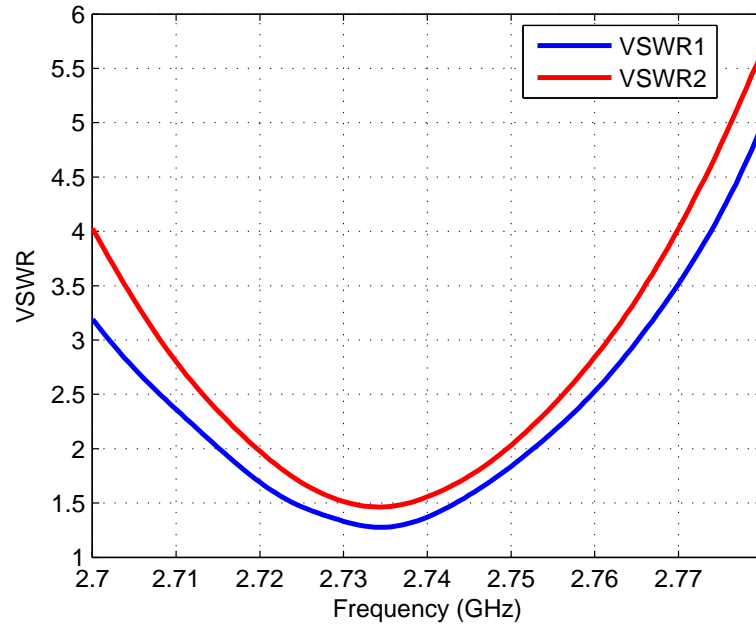
The second bandwidth limiting factor is the phase delay caused by the non-constant path delays at different locations of the reflectarray surface. It is also called differential spatial phase delay [53]. The biggest differential spatial phase delay occurs at the edge of the reflectarray. At the design frequency \mathbf{f}_0 , the differential spatial phase delay $\Delta\mathbf{S}$ is the electrical path difference between focal length \mathbf{f} and the ray trace \mathbf{S} that is incident on the edge at the array plane [53],

$$\Delta\mathbf{S} = (\mathbf{N} + \mathbf{d})\lambda \quad (2.2)$$

where \mathbf{N} is an integer and \mathbf{d} is a fractional number of a free-space wavelength λ .

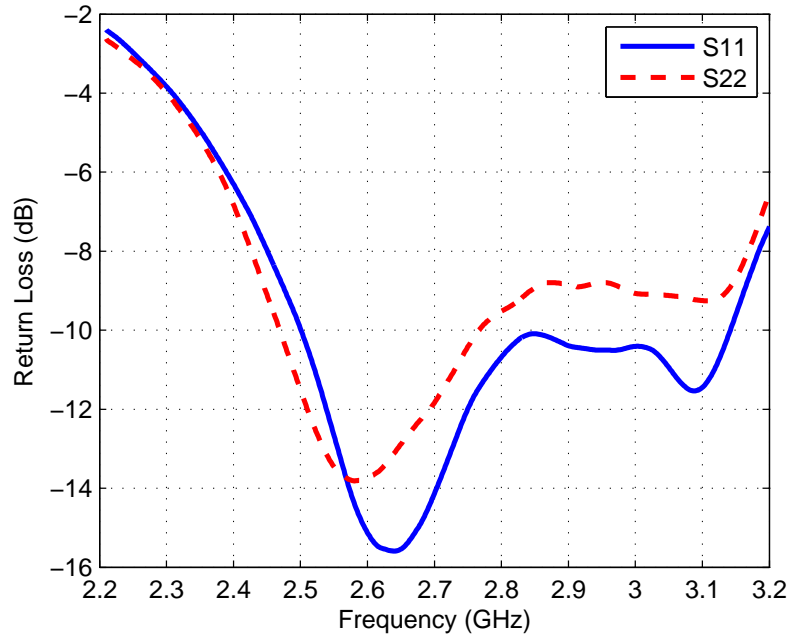


(a)

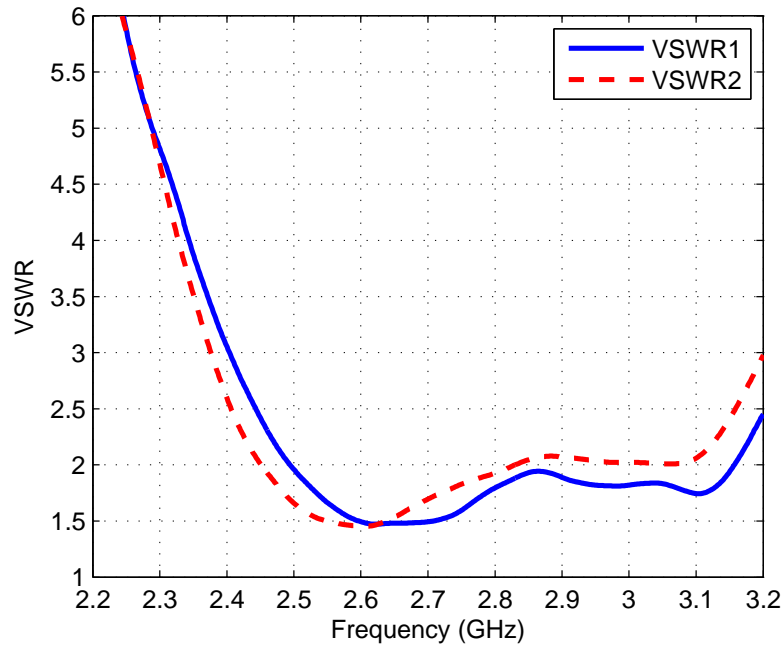


(b)

Figure 2.4: Measurement results of the narrow band dual-polarized patch antenna. (a) return loss, (b) Voltage Standing Wave Ratio (VSWR).



(a)



(b)

Figure 2.5: Measurement results of the broadband stacked patch antenna. (a) return loss. (b) VSWR.

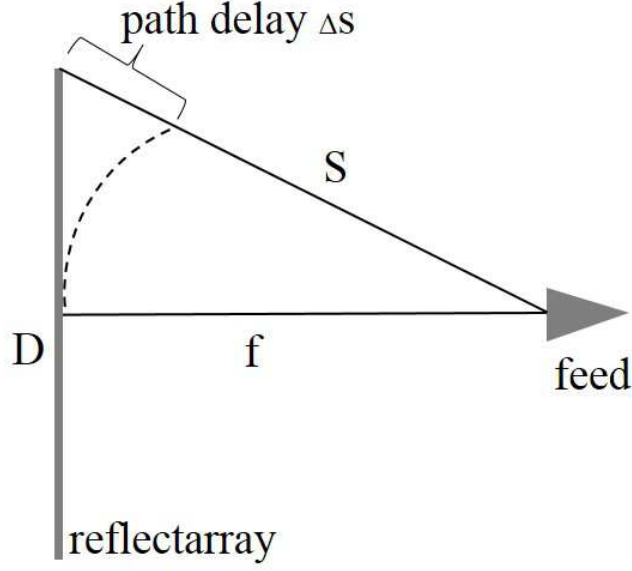


Figure 2.6: Geometry for the reflectarray.

Therefore, $d\lambda$ is the compensated phase in order to obtain a planar wavefront at the focal plane. The compensation phase can be realized by an appropriate length of phase delay line attached to the patch. However, when the frequency changes to f_1 , the differential spatial phase delay ΔS will also change,

$$\Delta S = (N + d)(\lambda + \Delta\lambda) \quad (2.3)$$

Thus, a phase error will occur since the phase delay lines are fixed and the extra phase delay $(N + d)\Delta\lambda$ cannot be compensated in the re-radiated phase front. Furthermore, the phase error is dependent on the reflectarray dimensions, mainly the array diameter D and focal length f . The reflectarray geometry is shown in Figure 2.6.

Let k_0 and k_1 be the wavenumbers $(2\pi/\lambda)$ at the design frequency f_0 and operational frequency f_1 . Then the phase delays at the edge of the reflectarray,

relative to the phase at the center of the reflectarray, are given by $\mathbf{k}_0(\mathbf{S} - \mathbf{f})$ at design frequency \mathbf{f}_0 and $\mathbf{k}_1(\mathbf{S} - \mathbf{f})$ at operational frequency \mathbf{f}_1 , respectively [55]. The phase error ϕ at these two frequencies is given as,

$$\phi = \mathbf{k}_0(\mathbf{S} - \mathbf{f}) - \mathbf{k}_1(\mathbf{S} - \mathbf{f}) = (\mathbf{k}_0 - \mathbf{k}_1)(\mathbf{S} - \mathbf{f}) \quad (2.4)$$

The maximum effect of this phase error ϕ is 180° induced by the frequency shift, because the out-of phase radiation from the edge elements will detract from the overall gain of the reflectarray and the overall efficiency will be reduced. Thus, when the phase error ϕ equals to 180° ,

$$\phi = (\mathbf{k}_0 - \mathbf{k}_1)(\mathbf{S} - \mathbf{f}) = \pi \quad (2.5)$$

By substituting $\mathbf{k} = 2\pi/\lambda$ and $\lambda = C/f$ into Eq. 2.5,

$$\frac{\Delta f}{f_0} = \frac{C}{2f_0} \frac{1}{\mathbf{S} - \mathbf{f}} \quad (2.6)$$

For the array diameter D , the radial distance S from the feed to the edge of the reflectarray is given as,

$$S = \sqrt{\left(\frac{D}{2}\right)^2 + f^2} \quad (2.7)$$

Substituting Eq. 2.7 into Eq. 2.6 results in,

$$\frac{\Delta f}{f_0} = \frac{C}{2f_0 D} \frac{1}{\sqrt{\frac{1}{4} + \left(\frac{f}{D}\right)^2} - \frac{f}{D}} \quad (2.8)$$

The total frequency bandwidth is given by,

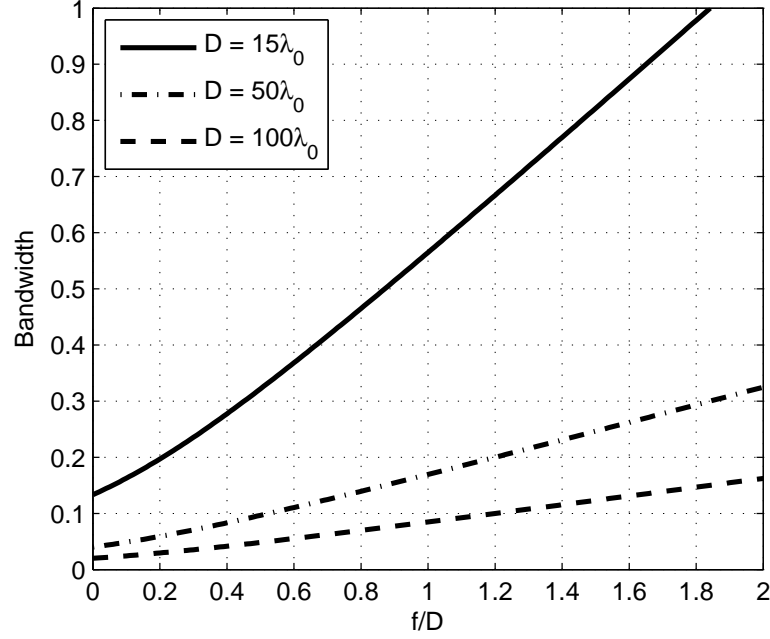


Figure 2.7: Bandwidth limitation of reflectarray for phase error $\phi = 180^\circ$ at edge of array aperture.

$$BW = \frac{f_{upper} - f_{lower}}{f_{center}} = \frac{(f_0 + \Delta f) - (f_0 - \Delta f)}{f_0} = \frac{2\Delta f}{f_0} \quad (2.9)$$

Assuming a phase error $\phi = 180^\circ$ at the edge, the bandwidth against focal ratio f/D for various aperture dimensions is plotted in Figure 2.7. From Figure 2.7, it is observed that the bandwidth limitation is more pronounced when the aperture dimension of reflectarray increases as large as 50λ . The bandwidth is about 15% for a focal ratio f/D in the range of 0.6 to 1.0, which is the typical f/D used in practical reflectarrays [55]. Especially, when the dimension of reflectarray increases to 100λ or even higher, the bandwidth can hardly raise above 20% even for reflectarrays with larger f/D . Moreover, it is also seen that

a larger f/D ratio improves the bandwidth, possibly due to better illumination efficiency and spill efficiency.

2.3 Broadband, Single Layer Element Design

From the discussion in section 2.2, we understand that the microstrip reflectarray has an inherent bandwidth limitation. This results in the maximum range of phase variation of a single layer reflectarray element that can be achieved is on the order of **330°** for thickness smaller than a tenth of wavelength [4]. Moreover, due to the narrow band behavior of microstrip patches, the reflection phase curves can be highly nonlinear, which makes the reflectarray sensitive to manufacture tolerance. To design a reflectarray, the phase of the reflected wave should have a progressive variation over the whole aperture surface, which implies that phases in a whole range from 0 to **360°** should be used for the reflection coefficient. This can be solved by stacking double and triple layers of patches of different sizes, as in [12, 18]. By stacking several layers, a multi resonant behavior is obtained and the phase range can be several times of **360°**, and using thicker dielectric substrate a smoother and more linear phase variation can be obtained [18, 53]. However, one drawback of the multi-layer structure is the increased cost and complicated assembly. For example, for the single layer and dual layer microstrip patch elements designed for the Configurable Phased Array Demonstrator (CPAD) at the University of Oklahoma [48], the cost of element fabrication and assembly was doubled when replace the single layer element with a dual layer one.

In this chapter, a broadband low-cost reflectarray is designed to achieve a better linear behavior of the phase versus size in a range wider than **360°**. The low-cost feature is achieved by adopting a single layer reflectarray configuration.

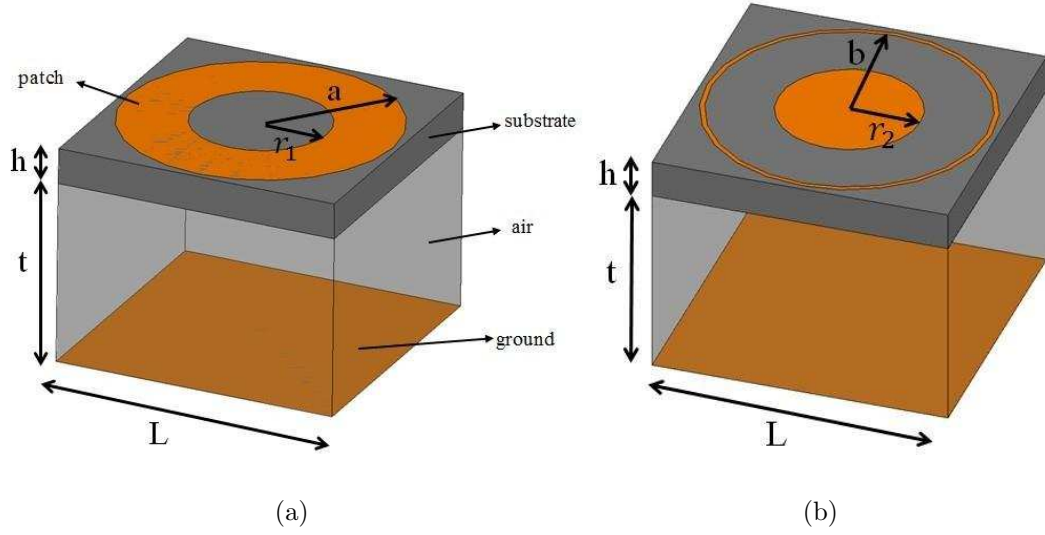


Figure 2.8: Two types of element configurations, (a) ring and (b) circular patch with ring boundary (ring-patch).

Moreover, different from traditional single layer reflectarray, in this design the reflectarray elements are composed of two different types of realizations, which are ring and circular patch with a ring boundary. The element configuration of circular patch with a ring boundary is referred to as ring-patch element, comparing to the element with only a single ring. The inner radius of the ring and the radius of the circular patch are changed respectively to compensate for the spatial phase delay. A Ku-band reflectarray was designed to demonstrate the proposed technology.

Considerations focus on a Ku-band single-layer reflectarray elements with two different configurations aimed for operation at 13.325 GHz. The elements are arranged in a square unit cell with periodicity of $\mathbf{L} = 12.5$ mm, which is equivalent to 0.55 wavelength (λ) at 13.325 GHz. The element configurations are shown in Figure 2.8. Both types of elements are assumed to be printed on a thin dielectric substrate RT/Duroid 5880 with $\epsilon_r = 2.2$, and thickness $h = 1.575$ mm.

An air/foam layer of $\varepsilon_r = 1$ with thickness $t = 8$ mm is inserted between the substrate and the ground plane to enhance the linearity of the phase curve.

It is known that phase of the reflected wave varies with the resonant length of the elements. In the proposed element configurations, the inner radius r_1 of the ring and the radius r_2 of the circular patch are changed respectively to generate the phase curve. In Figure 2.8 (a), the outer radius a of ring is fixed at 6 mm, and the inner radius r_1 varies from 0.1 mm to 5.9 mm. In Figure 2.8 (b), the outer radius b of ring boundary is fixed at 6 mm with a width 0.2 mm, while the radius r_2 of the circular patch varies from 0.1 mm to 5.8 mm. The dimensions and parameters of the elements design are also summerized in Table 2.2.

Table 2.2: Dimensions and parameters of the reflectarray

Parameter	Value
Frequency	13.325 GHz
Unit cell size L	12.5 mm (0.55λ)
Substrate RO5880 height h	1.57 mm
Air/foam layer height t	8 mm
Ring outer radius a	6 mm
Ring inner radius r_1	0.1 mm \rightarrow 5.9 mm
Boundary radius b	6 mm
Circular patch radius r_2	0.1 mm \rightarrow 5.8 mm

The analysis and design of reflectarray is based on the use of reflection phase of the single element with a certain geometrical parameter change. Thus, the

accurate characterization of the individual element's reflection phase is very important. To obtain the reflection phase, the reflective element can be analyzed as an isolated element or in an array environment. The isolated element analysis is valid when the distance between the edges of the adjacent patches is larger than 0.25λ , also assuming the array elements spacing is larger than 0.6λ . In this scenario, it was stated that the mutual coupling between the elements can be neglected [67, 68]. This assumption is very common in elements with attached stubs and elements with different rotation angles [9, 68, 69], where the element dimension is fixed while only the stub lengths or angles of element rotation are varied to generate different reflection phases.

However, the effect of mutual coupling can be stronger for variable sized elements, because that sometimes the separation between the patches is small. In this case, the reflection phase can be calculated by considering an infinite periodic array model, where the mutual coupling between elements can be automatically taken into account [6]. The infinite periodic array model is an array structure with repeated geometry, defined by a unit cell and a uniform periodic spacing. It is extensively used in the applications such as array antennas, frequency selective surfaces (FSS) and meta-materials. Furthermore, by applying Floquet's theorem, the infinite periodic array model can be reduced to only one unit cell with a Floquet incident wave [70, 71], which makes the characterization very efficient, as well as being accurate [72].

The reflection phase of the unit cell of the infinite periodic array model can be obtained by performing waveguide simulation (WGS). The WGS method is elaborated in details in [73]. In the WGS method, the reflection phase is calculated based on the reflection coefficient of the plane wave incident normally on the unit cell, and this reflection coefficient is equal to the reflection coefficient of

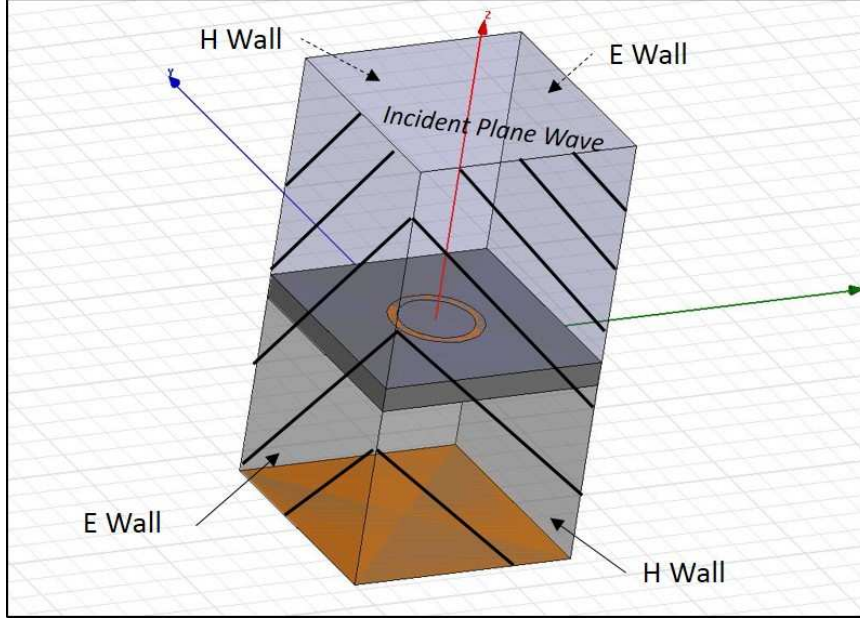


Figure 2.9: Unit cell waveguide simulation (WGS) approach.

the fundamental TEM mode incident on the multilayer structure (including air, foam, substrate and metal patch) in a waveguide environment. When applying WGS approach, one pair of unit cell boundaries are set to E-wall, while another pair of boundaries are set to H-wall. Then a plane wave is incident onto the microstrip patches as the excitation. The reflected phase is then computed from the reflection coefficient at the top patch surface. One example of the unit cell with WGS approach is shown in Figure 2.9.

Ansoft HFSS is used for the reflection phase characterization of the unit cell, and the obtained phase curves are illustrated in Figure 2.10. It can be observed that variable-sized ring covers a phase range from -132° to 188° and the variable-sized ring-patch element can generate a phase range from 188° to 230° . In total, the combination of these two element configurations can provide at least a 360° phase range, which is sufficient for reflectarray application. Furthermore, the

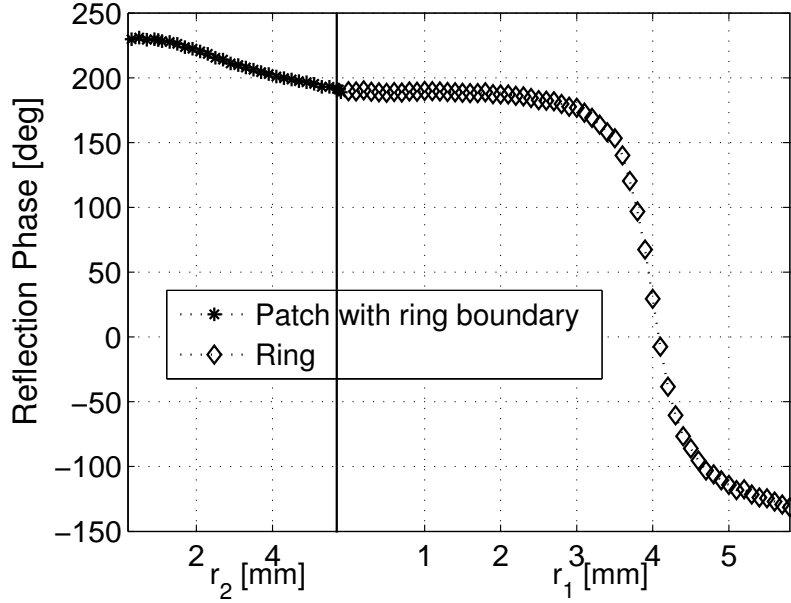


Figure 2.10: Reflection phase of the unit cells at normal incidence.

phases are approximately a linear function of the element sizes for both configurations. Gentle phase variation and wide phase range are important to reduce the manufacturing errors and improve the operating frequency band of the reflectarray.

In the presented design with WGS approach, the elements reflection phase was estimated by considering the normal wave incidence, where an additional assumption was applied that the phase response is independent of the angle of incidence of the impinging wave. This assumption is valid for the central elements of a center-fed reflectarray, where the incident angles are not too far from normal incidence. It has been shown in reference [74] that the phase variation is small for a incident angle less than 40° . If the incident angle is greater than 40° , the phase change may go up to 50° for an incidence angle of 60° , where the approximated reflection phases of normal wave incidence may not be applicable [74]. As the reflectarray in this design uses two types of element configurations,

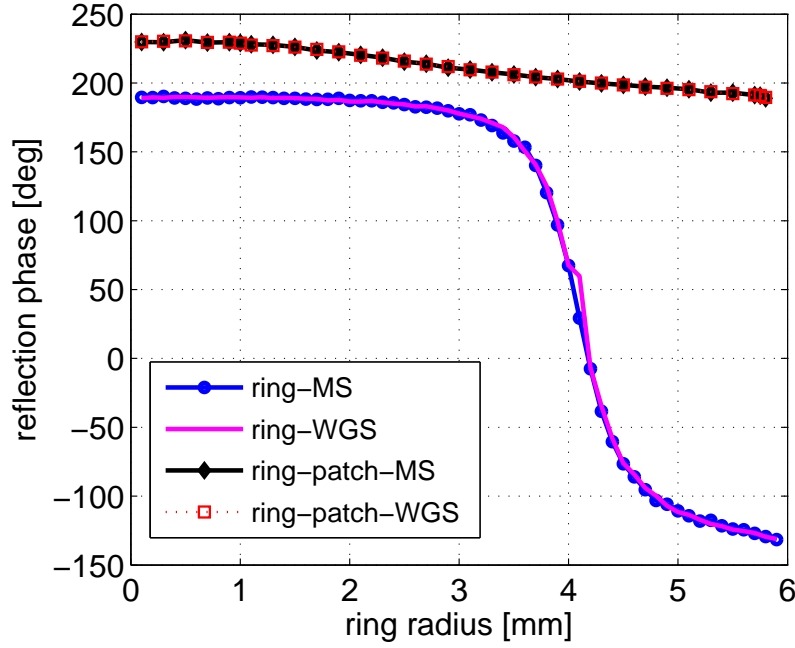


Figure 2.11: Simulated reflection phase curves on the designed unit cell using WGS and MS methods are compared.

it is worthwhile to test this assumption for these new conditions. Thus, the reflection phases with different angle of incident wave on the unit cell should be calculated.

Due to the fact that the WGS method does not offer flexibility of setting an arbitrary angle of incidence, another method which affords master and slave (MS) boundaries and Floquet Ports to simulate the unit cell in an periodic array environment was used. In this method, any oblique incident angle can be used for the Floquet Ports. This method is here referred to as MS method.

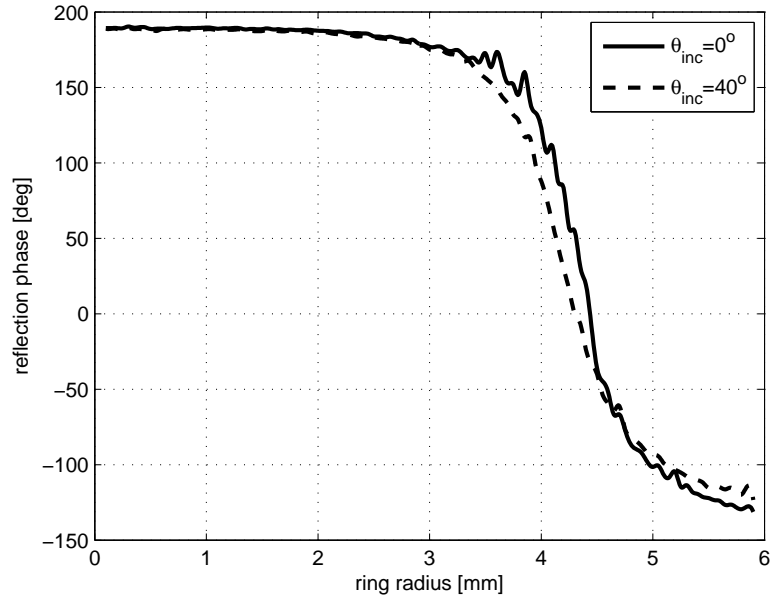
In order to validate this method, the reflection phase curves with normal incident wave on the designed unit cell using both WGS and MS methods are simulated and compared in Figure 2.11. It can be seen that for both ring and

ring-patch elements, the WGS and MS methods have a very good agreement on the reflection phase curves.

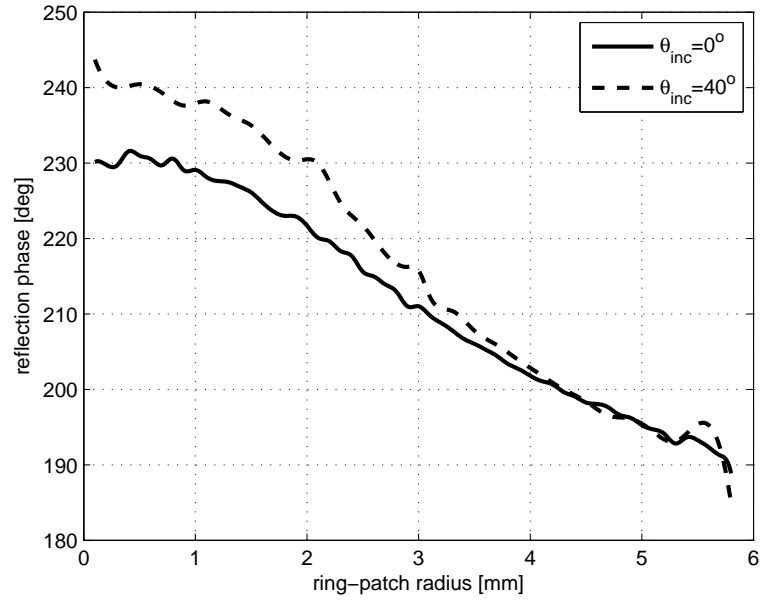
Figure 2.12 shows the reflection coefficient phase curves for the designed ring and ring-patch unit cells for different incidence angles. As seen in Figure 2.12 (a), the reflection coefficient phase deviates from the case of normal incidence mostly around the resonance size of the ring in the range 3.5 mm to 4.5 mm. The maximum phase deviation in this range is about 50° when incidence angle $\theta_{inc} = 40^\circ$. For the phase curves of the ring-patch unit cell in Figure 2.12 (b), the maximum phase deviation is only about 10° when incident wave becomes oblique to $\theta_{inc} = 40^\circ$. For the remaining size variation ranges other than the resonant size, the phase deviation reduces quickly and can be neglected for both element configurations. So the simulation result indicates that the normal incidence, either in WGS or MS simulations, can provide a reasonable approximation for the reflection coefficient phase for the incidence angles θ_{inc} up to 40° for the designed element configurations.

2.4 Antenna Array Design

In the previous section, the reflection phase curves of the reflectarray elements are characterized. In this section, a circular reflectarray of diameter $D = 305$ mm with a center feed horn is demonstrated. The dimensions of the reflectarray elements are determined based on the reflection phase curves generated in the previous section. Three steps in the reflectarray design will be discussed, including the horn pattern characterization, reflectarray efficiency estimation and array aperture phase distribution.



(a)



(b)

Figure 2.12: Simulated reflection phase curves for different incidence angle ($\theta_{inc} = 0^\circ$) and 40° on (a) ring element and (b) ring-patch element, respectively.

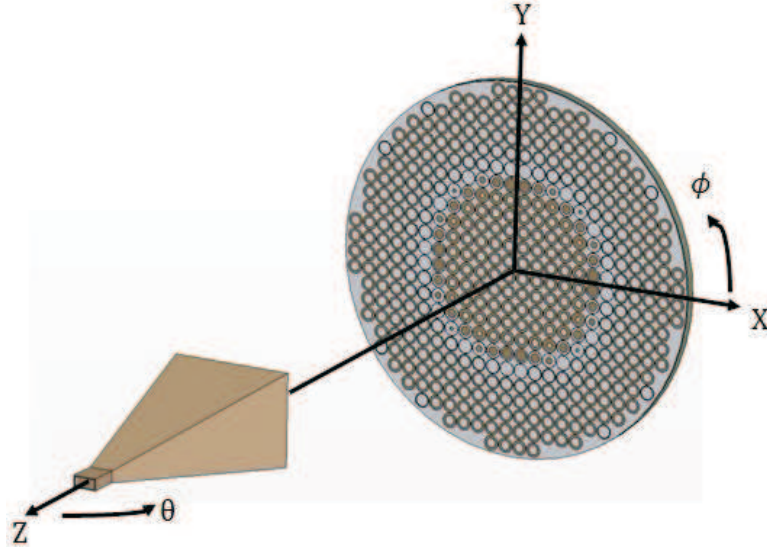
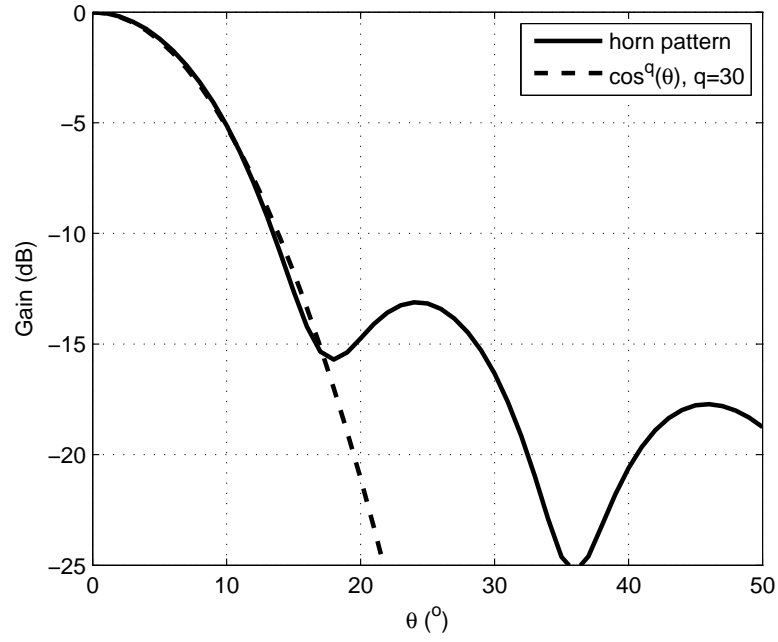


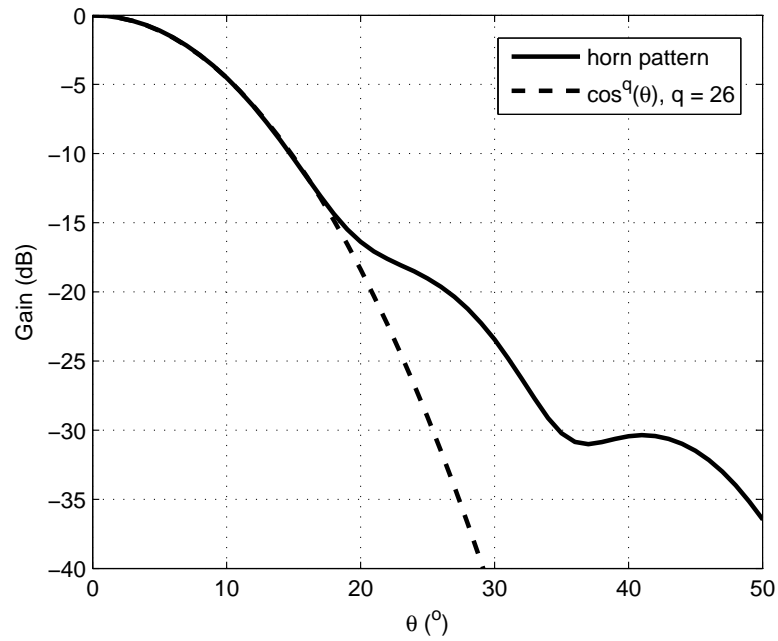
Figure 2.13: The coordinate system used in the reflectarray design. The YOZ plane and XOZ plane are treated as H -plane and E -plane, respectively.

2.4.1 Horn Pattern Characterization

First a standard horn antenna has been selected for feed, and the center-fed scheme is used for the reflection design concept demonstration. A standard horn antenna *ATM 75-442-6* from ATM Inc. is used as the feed and its pattern has been modeled as a $\cos^q(\theta)$ function. Figure 2.13 shows the coordinate system of a center-fed reflectarray adopted in this design. Here the YOZ plane and XOZ plane are treated as H -plane and E -plane, respectively. Since the feed is a pyramidal horn, the patterns in E -plane and H -plane are not the same. So different q values are estimated in each plane and an averaged value is used in the model. The simulated horn patterns are shown in Figure 2.14. The calculated q factor at 13.325 GHz is chosen to be $(30+26)/2=28$.



(a)



(b)

Figure 2.14: Simulated feed horn pattern and the $\cos^q(\theta)$ with different q values, (a) E -plane and (b) H -plane patterns.

2.4.2 Reflectarray Efficiency

Similar to the conventional reflector design, the feed position f is optimized to achieve the maximum aperture efficiency. As Huang stated in [4], a good geometry design, primarily the focal length to array dimension ratio f/D , will yield good reflectarray efficiency. The aperture efficiency η_a is a measure of how effective a reflectarray is for receiving the energy of an incident electromagnetic wave from the feed horn. It is defined as the product of the illumination (η_I) and spillover (η_s) efficiencies: $\eta_a = \eta_I \times \eta_s$. For reflector and reflectarray antenna, usually the aperture fields get weaker towards the edge of the reflector panel, which is the edge illumination effect [75]. The illumination efficiency is the ratio of the electric field at the edge and at the center of the reflectarray. The illumination efficiency for a center-fed reflectarray can be obtained using following equation [76]:

$$\eta_I = \frac{[\left((1 - \cos^{q+1} \theta_e)/(q+1)\right) + ((1 - \cos^q \theta_e)/q)]^2}{2 \tan^2 \theta_e [(1 - \cos^{2q+1} \theta_e)/(2q+1)]} \quad (2.10)$$

The spillover efficiency η_s represents the fraction of the power of the feed horn that actually gets reflected by the reflectarray. It is the ratio of the received power of the reflector and the total power of the feed horn. When the spillover efficiency η_s is not 100%, it means some power from the feed horn “spills over” the edge of the reflectarray and is lost. The spillover efficiency η_s can be obtained [76],

$$\eta_s = 1 - \cos^{2q+1} \theta_e \quad (2.11)$$

where θ_e is half of the subtend angle from the feed to the reflectarray aperture. As shown in Figure 2.15, when f/D increases, the spillover efficiency decreases

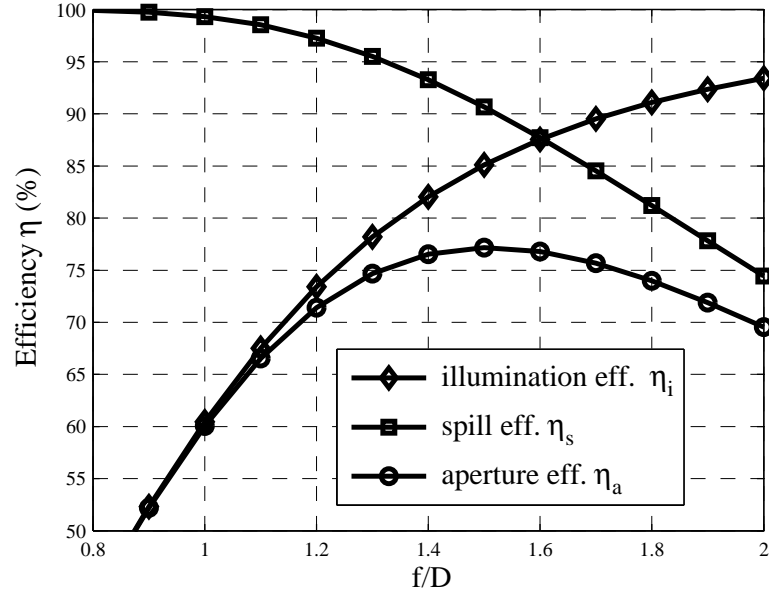


Figure 2.15: Efficiencies versus f/D ratio.

but the illumination efficiency increases. In this design, $f/D = 1.5$ is chosen for the selected horn antenna considering the tradeoff between η_s and η_i and also the antenna setup size. It is worth noting that in practice, additional efficiency terms must be introduced, such as those due to cross polarization or to partial aperture blockage by the feed horn. For example, Figure 2.15 shows the best aperture efficiency is 77% at $f/D = 1.5$, however, taking into account other losses, the aperture efficiency of a practical reflectarray is typically of the order of 50% to 60%.

2.4.3 Reflectarray Phase Distribution

To form a focused beam in a given direction, the phase shift must be introduced at each element on the reflectarray. Considering the coordinate system in Figure

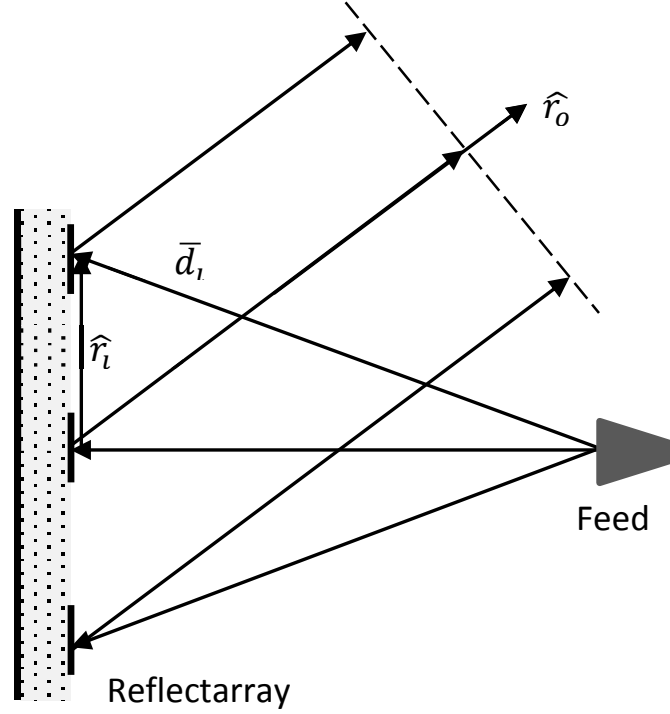


Figure 2.16: Reflectarray geometry.

2.13 and the reflectarray geometry in Figure 2.16, this distributions over the reflectarray plane are computed by applying the following formula [4]:

$$\Phi_{m,n} = k_0(d - (x \cos \phi_b + y \sin \phi_b) \sin \theta_b) \quad (2.12)$$

where (x, y) are the coordinates of the element $_{m,n}$, and d is the distance from the center of element $_{m,n}$ to the central point of the feed aperture. The desired beam direction is defined by ϕ_b and θ_b , which are the spherical coordinates with origin at the center of the array. Figure 2.17 shows the required phase-shift on the designed circular reflectarray with feed horn centered, which produces a pencil beam in normal direction. Then the configurations and sizes of each element can be determined based on the phase curves given in Figure 2.10.

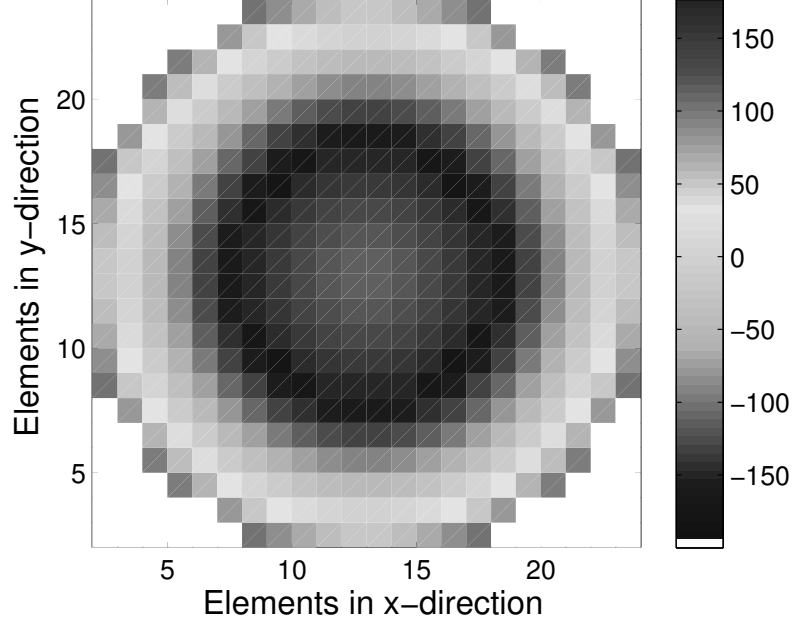


Figure 2.17: Required phase distribution on the broadband single layer reflectarray.

2.5 Antenna Array Simulation

Full-wave electromagnetic simulations on this 424-element reflectarray are carried out using the Integral Equation Solver in CST Studio[®] [77]. The Integral Equation Solver of CST is usually used for far-field and radar cross section (RCS) computation for electrically large structures (dimension $> 10\lambda$). The Integral Equation Solver is based on the multilevel fast multi-pole method (MLFMM) [78], which enables an optimal complexity in memory and simulation time.

In the MLFMM, the mesh is subdivided into groups with a fixed dimension, typically no smaller than 0.3λ , and the interaction between groups is calculated in

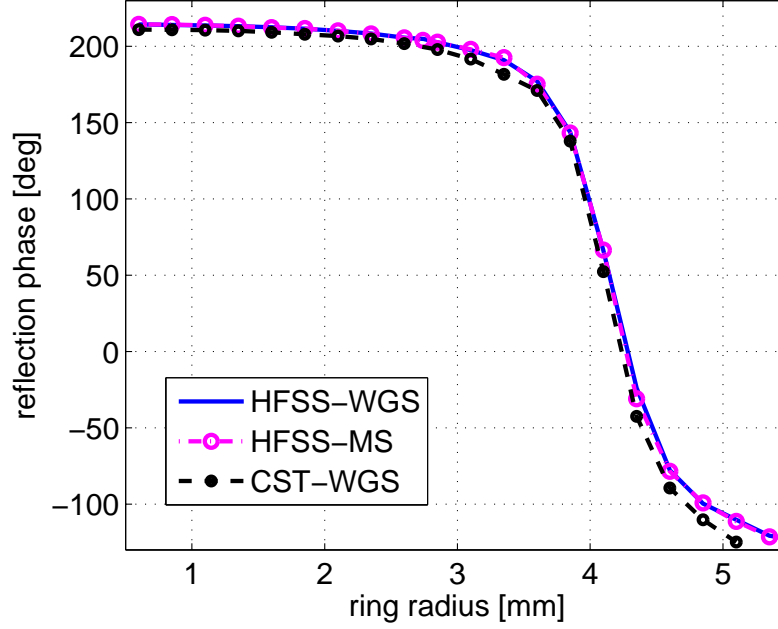


Figure 2.18: The comparison of obtained reflection phase curves between HFSS and CST.

a recursive scheme. The complexity of the MLFMM is $O(N \log N)$, where N is the number of unknowns, while the conventional method of moments (MoM) solver has a complexity of $O(N^2)$, which requires a large computational cost [79–81].

In section 2.3, a combination of ring and ring-patch elements has been used to achieve a wider reflection phase range $> 360^\circ$. The reflection phases of both element configurations were obtained using the WGS and MS approaches in HFSS. When introducing the phase shift on the elements according to the phase curves obtained in HFSS and simulating the far-field performance of the array in CST, it is worthwhile to test the consistency of the two simulation tools regarding to the phase curves. The ring element in Figure 2.8 (a) was also simulated using the WGS approach in CST with a normal incident wave to generate the reflection

phase curve, and it is compared with the results obtained from HFSS in Figure 2.18.

It can be seen that, for the case of normal incident wave, there is a good agreement on the obtained phase curves between the two simulation tools. Due to that HFSS has a better efficiency on calculating the reflection phase at a single frequency, while CST usually calculates the reflection coefficients in a frequency range instead of a single frequency point, in this design the HFSS was adopted to calculate the **reflection phase** of the proposed elements at the center frequency 13.325 GHz.

In order to simulate the far field pattern of the reflectarray, the radiation pattern of the feed horn is calculated first, from which the incident field on the reflectarray is found by using far field source in Integral Equation Solver of CST. This approach is referred to as the *data-link* approach. By using this *data-link* approach in Integral Solver rather than simulating both the feed horn and reflectarray simultaneously in Time Domain Solver, the computing efficiency is significantly increased.

This simulation is accomplished on a computer of 8 cores CPU (2 GHz) and 32 GB RAM. It takes about 5 hours for the simulation using a regular surface mesh density. The calculated far field patterns in H -plane and E -plane are shown in Figure 2.19. It is noted the *data-link* approach, which separates the horn and reflectarray during calculation, can not account for the blockage of the feed horn, especially for a center-fed reflectarray with the mainbeam directing at broadside. It only gives acceptable results on and near the broadside for the mainbeam.

To investigate the blockage effects, the radiation pattern of the reflectarray in the *data-link* simulation is here set as the incident field on the passive horn reversely, and then the far field is calculated again. This approach, which gives a

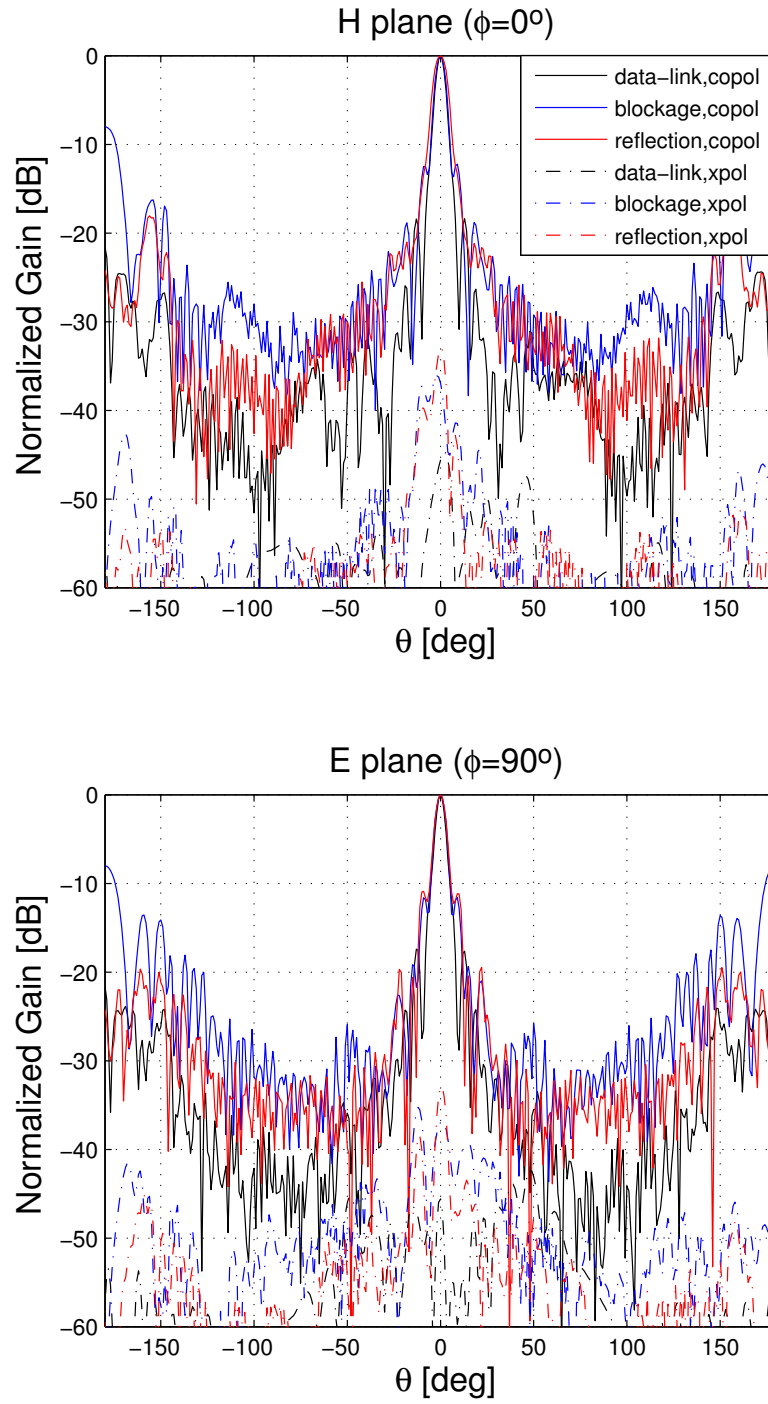


Figure 2.19: Simulated normalized radiation pattern at 13.325 GHz.

rough approximation of the contribution of center blockage on the calculated far field, is here referred to as *blockage* approach in Figure 2.19. It can be seen that a sidelobe appears at $\theta = 10^\circ$ for both *H*-plane and *E*-plane patterns, due to the blockage of the center-fed horn.

Furthermore, the blocking obstacle (feed horn), will also scatter fields back toward the reflectarray panel and thus cause multiple reflections. It is laborious and will cost huge computation resources to predict such effects accurately. Only a simple scenario is considered here to account for the single reflection, which uses the radiation pattern result in the *blockage* as the far field source on the reflectarray. This approach is referred to as *reflection* method. In the simulation results, the sidelobe level is increased significantly and the main beam is also broadened slightly due to the center blockage and multiple reflections.

It is believed that one cause of the higher sidelobe level is that some radiation energy supposed to form the main beam is blocked by the center-fed horn, and thus scatters from the main beam direction and contributes the higher sidelobe. The sidelobe behavior of the reflectarray is also caused by the sidelobes of the radiation pattern of the feed horn, such as the horn patterns shown in Figure 2.14, where its specular reflection on the reflectarray surface contributes the sidelobe of the reflectarray.

Another reason of the “noisy” sidelobe is perhaps the result of element phase errors (variation) shown in Figure 2.12. In the array simulation, element phase curve is determined using normal incidence, with the assumption that the reflection phase deviates not much when the incident angle becomes oblique up to $\theta_{inc} = 40^\circ$. Nevertheless, the phase errors induced by oblique incidences on the element will probably result in radiation energy scattering from main beam direction and increasing the sidelobes of the radiation pattern.

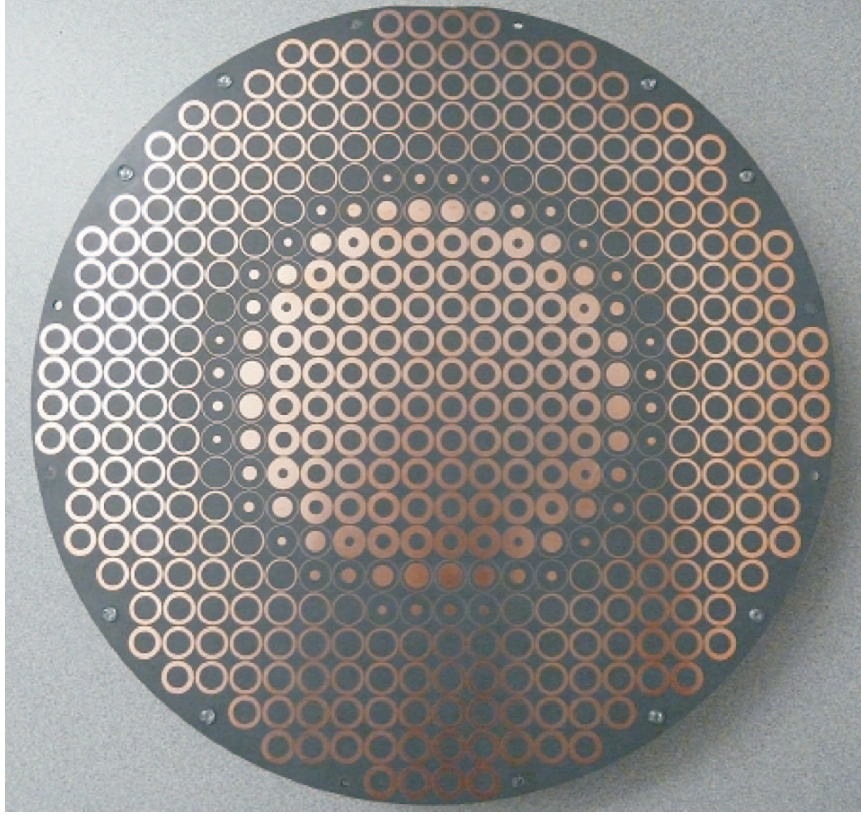


Figure 2.20: Fabricated broadband single layer reflectarray.

2.6 Antenna Array Measurements

The prototype reflectarray is shown in Figure 2.20, which has 424 elements in total. Measurements of the reflectarray are conducted in the anechoic chamber at University of Oklahoma with the range of 6 meters. Only the measurement for E-plane cut was carried out. The photo of the antenna setting for E-plane measurement is shown in Figure 2.21.

In the measurement the feed horn of the reflectarray was set as the transmit antenna, while the reflected beam from the reflectarray was received by a standard horn at the other end of the anechoic chamber. The normalized radiation patterns at 13.325 GHz are given in Figure 2.22. By comparing the results in Figure 2.22,



Figure 2.21: Reflectarray measurement setup for E-plane cut.

we see that the measured half power beamwidth (HPBW) of the main beam is 4° , which is in good agreement with the simulation. The cross-polarization level is -27.2 dB near the main beam region and below -30 dB outside. However there are some discrepancies in the co-polarization sidelobes. As explained in the previous simulation section, the center feed blockage and multi-reflection effect mainly contribute to this increased side lobe levels. To accurately predict the performance of the reflectarray with a center-fed horn, the blockage from the feed horn and the support structure should be taken into account carefully. In the next chapter, the blockage effect will be investigated and a reflectarray with tilted beam will also be presented to mitigate the blockage from the center-fed horn.

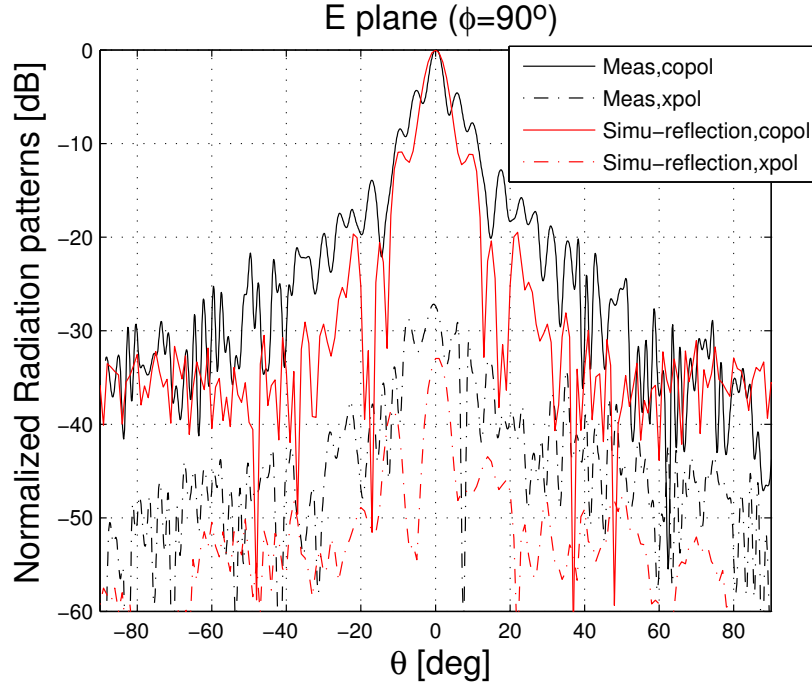


Figure 2.22: Measured normalized radiation patterns at 13.325 GHz.

2.7 Conclusion

Reflectarray shows many advantages over both traditional reflector antenna and phased array antenna. A single layer Ku-band microstrip reflectarray constituted by two different types of elements for larger phase range has been developed with main beam pointing at broadside. The feed and reflector of this antenna has been designed with full wave EM solving tools. The measured results of the reflectarray show good agreements with the simulation on main beam width and cross-polarization levels. A slightly side lobe level increase occurs in measurements due to the center feed blockage and multiple reflections on this relatively small-sized reflectarray. In the next chapter, study will be provided to improve the accuracy of the feed blockage prediction in a center-fed reflectarray.

Chapter 3

Analysis of Blockage Effects in a Center-fed Reflectarray

3.1 Introduction

In Chapter 2, a broadband low-cost reflectarray antenna design was presented. A combination of two types of element configuration is adopted in the reflectarray design to give a reflection phase range $> 360^\circ$. For proof of concept, a reflectarray with a diameter of 305 mm and 424 elements was fabricated and measured. For simplicity, a symmetrical reflectarray structure and a center-fed scheme was adopted in the reflectarray design. However, certain obstacles, such as the feed horn, subreflector, and their supports, still exist. When these obstacles present in front of the reflectarray, a portion of reflected wave is blocked, and the feed's absorption weakens the reflected power. For example, in Chapter 2, the simulation approaches, including the *blockage* and *reflection* approaches, only predicted the beam width accurately, but lacked accuracy on the estimation of sidelobe level and cross-polarization level. Thus, an accurate prediction of blockage effect in reflectarray design should be further developed.

Blockage effect has been well-documented for conventional parabolic reflector antennas [82–84]. For reflectarrays, blockage effect is similar while has unique characteristics. First, many blockage effect analyses for dish antennas are based on asymptotic methods such as ray-tracing and physical optics, which may not

be sufficient for reflectarrays. Second, the construction of array elements can be complicated and *beam-tilting* needs precise modeling at the level of each individual patched element. Therefore, better modeling and accuracies are needed, and simulation technique is more demanding for reflectarrays. In this chapter, several methods are introduced, and comparisons among these methods are presented in terms of modeling the blockage effects, accuracies, and efficiencies [85]. For a realistic example, the reflectarray design in Chapter 2 with a standard horn feed was used for the study, and this antenna was simulated using the MLFMM approach in the CST Studio, including both the array and the feed, to provide an accurate reference radiation pattern prediction. The blockage of the reflectarray is further suppressed by using a support structure of wood material (dielectric constant $\varepsilon_r \approx 1.4$) instead of acrylic plastic (dielectric constant $\varepsilon_r \approx 3.9$). Furthermore, another reflectarray with mainbeam direction steered 18° off broadside is also presented. These arrays have been fabricated and measured to verify the calculated results.

3.2 Analysis Of Blockage Effects

In this section, five modeling schemes to account for the blockage effects in a reflectarray are described. The five schemes are illustrated in Figure 3.1 and described in more detail in following Sections.

3.2.1 Zero Blockage

When analyzing center-fed reflectarray antennas, treating the feed and the reflectarray separately is convenient. First, the radiation pattern of the feed antenna is calculated by simply using a time domain solver by CST. Then, the radiation

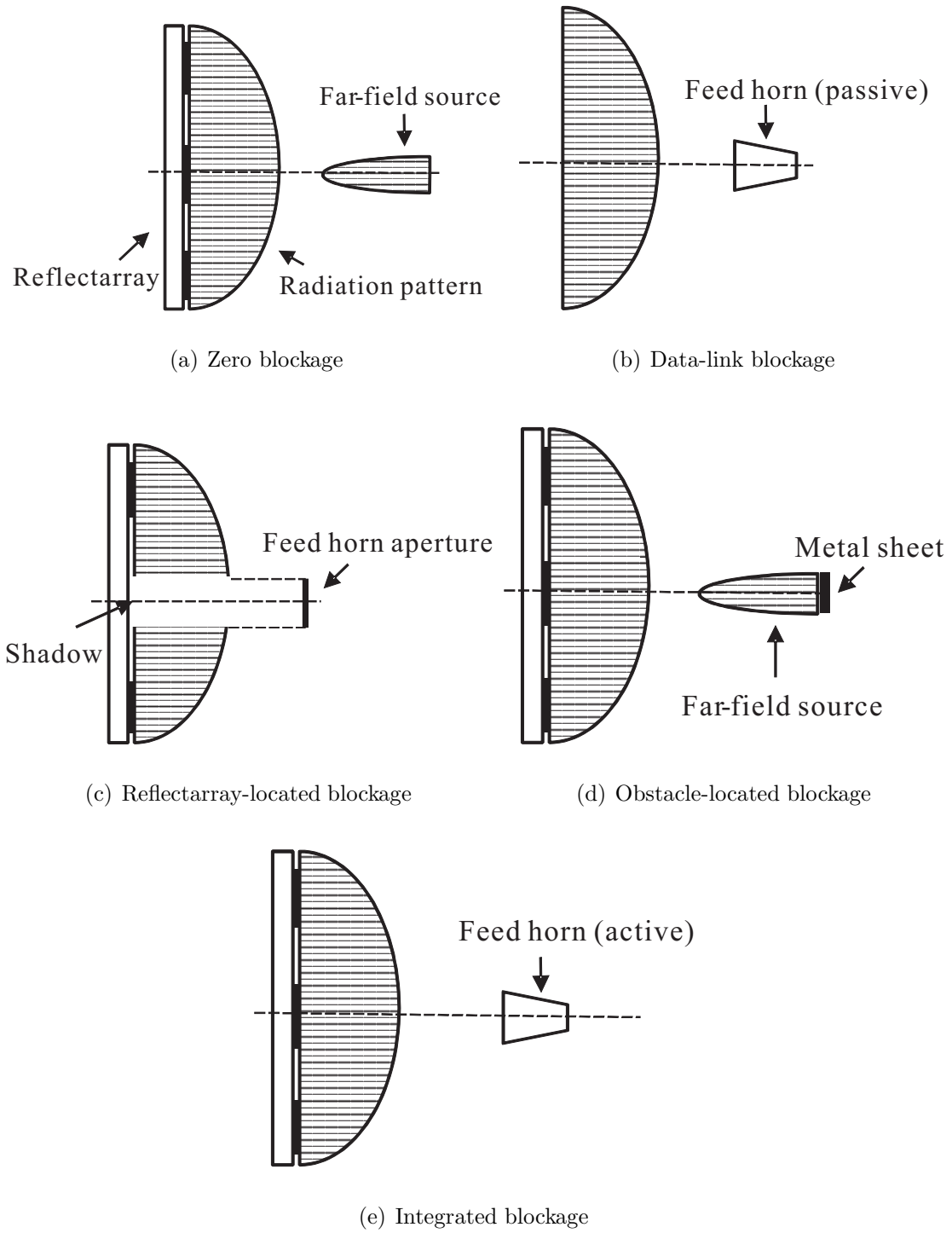


Figure 3.1: Different schemes for modeling blockage effects in a reflectarray.

pattern of the feed is set as the incident field on the reflectarray, and the radiation pattern of the reflectarray is found via the MLFMM method and far-field source function. As shown in Figure 3.1 (a), this method uses the radiation pattern rather than the physical horn as the feed, therefore, the blockage effect is not included in the calculation. This approach is referred to as *zero blockage* (ZB).

3.2.2 Data-link Blockage

In this scheme, the obtained radiation pattern of the reflectarray using the *zero blockage* method is first set as the incident field on the passive feed horn, and then the far-field radiation pattern is calculated. This method, which gives a rough approximation of blockage on and near the main beam direction, is shown in Figure 3.1 (b) and is referred to as *data-link blockage* (DLB).

3.2.3 Reflectarray-located Blockage

One common way to analyze the blockage in reflector antenna is to use the *null-field hypothesis* where an aperture field with the same amplitude as the unblocked field obtained in the *zero blockage* method is within the blocked area, but it is 180° out-of-phase as the blocking effect so that the two fields extinguish each other [82]. For a reflectarray, an alternative approach to improve the *null-field hypothesis* using the observation-point-dependent shadows [83]. As shown in Figure 3.1 (c), the first step of this approach is to calculate the shadow of the horn aperture on the reflectarray surface and then remove those elements located in the shadow area on the reflectarray. The reflectarray is then simulated with the remaining elements to include the blockage. This approach is called the *reflectarray-located blockage* (RLB) herein. Notably, this approach is not very accurate off the main

axis because the blocking feed is actually located at a certain distance in front of the reflectarray, not on the surface of it [84].

3.2.4 Obstacle-located Blockage

Another approach to improve the accuracy of simulation is to regard the feed as a smooth plane of conducting metal with the radiation pattern of the feed added in front of this metal sheet as the far-field source. Then, together with the metal sheet, the reflectarray is simulated as a whole structure. This approach is referred to as *obstacle-located blockage* (OLB). It is illustrated in Figure 3.1 (d).

3.2.5 Integrated Blockage

Finally, in order to determine which of the three schemes in Figure 3.1 (b) through (d) is the most accurate, the radiation pattern of the complete antenna structure with both the feed and the reflectarray is calculated using a full-wave solver in CST. The effect of center blockage and even multiple reflections (i.e., mutual coupling) between the feed and the array are implicitly included in this method. This approach is shown in Figure 3.1 (e) and is referred to as *integrated blockage* (IB).

3.3 Simulation and Measurement Results

This section describes the analysis of the different simulation approaches using the Ku-band reflectarray with a standard-gain horn designed in chapter 2. The reflectarray uses a combination of two types of element configuration to achieve a wider than 360° reflection phase range. The antenna array has a diameter of 13.6λ and focal length of 20.3λ . The fabricated planar array and the measurement

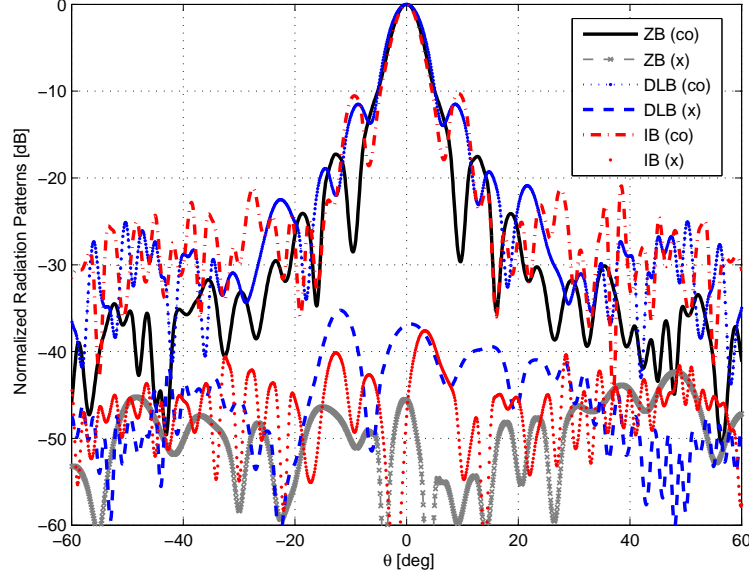


Figure 3.2: Simulation results of antenna radiation patterns at 13.325 GHz in E-plane. Calculated *zero blockage*, *data-link blockage* and *integrated blockage* radiation patterns.

setup are shown in Figure 2.2. Herein, the plane of the support strut is defined as the E-plane both in the simulations and measurements.

First, the calculated *zero blockage* and *data-link blockage* radiation patterns in the E-plane cut are shown in Figure 3.2. The *integrated blockage* radiation pattern, which incorporates the blockage effects more accurately, is also plotted in Figure 3.2 for comparison. As observed in Figure 3.2, the reflectarray in the *zero blockage* simulation scheme generates a good radiation pattern with a narrow beamwidth, low sidelobe levels (SLLs), and a very low cross-polar level. This is due to the fact that no blockage is assumed in the *zero blockage* simulation.

Next, the pre-obtained radiation pattern of the reflectarray is added onto a passive horn, and then the *re-radiation pattern* is calculated. In Figure 3.2, we can see from the *data-link blockage* simulation results that the front-placed horn

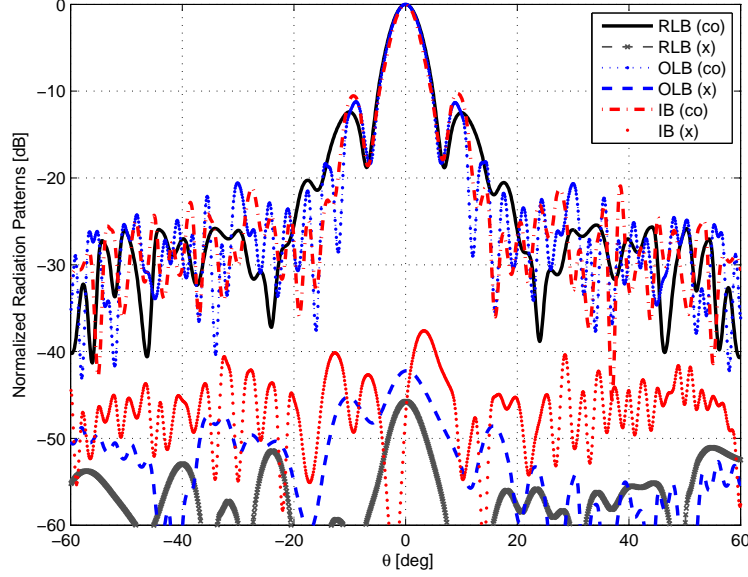


Figure 3.3: Simulation results of antenna radiation patterns at 13.325 GHz in E-plane. Calculated *reflectarray-located blockage*, *obstacle-located blockage* and *integrated blockage* radiation patterns.

causes large increases on the sidelobe levels and the cross-polar levels, and the beamwidth is also broadened by about 1° . This is because the reflected energy from the reflectarray is partially scattered by the feed horn. It convinces us that we must consider the blockage impact when designing a reflectarray with a relatively small size.

The calculated radiation patterns using the *reflectarray-located blockage* and *obstacle-located blockage* schemes are shown in Figure 3.3. By removing the elements located in the shadow area of the horn aperture on the reflectarray surface, the *reflectarray-located blockage* method can provide a quick prediction of the blockage effect. From these results, we can see that the *reflectarray-located blockage* radiation pattern has a slightly wider beamwidth than the *integrated blockage* result. Also in Figure 3.3, the small discrepancy on the SLLs between



Figure 3.4: Test setup of the reflectarray with a wood and acrylic structure.

the *reflectarray-located blockage* and *integrated blockage* results is probably due to the fact that in the RLB method, the removed elements break the phase integrity of the reflectarray. In other words, this RLB method provides a simple approach through the analysis of the array instead of the whole structure. On the other hand, the interactions between the horn and the array, such as the multi-reflections and the energy absorption by the horn, are ignored.

Next, both the array and the horn are considered in the simulation of the *obstacle-located blockage* scheme. In contrast to the *integrated blockage* method, the active horn is replaced by a simple metal sheet with same area as the horn aperture and a far-field source, which is the pre-obtained radiation pattern of the feed horn. In the OLB simulation result in Figure 3.3, the radiation pattern has a similar beamwidth as the IB result, and we can also see improved agreement on the SLLs with the IB result despite the slight difference (less than 1 dB) that can still be observed.

Both the feed horn and the array are included in the IB simulation. For the actual measurement setup, however, a support structure must be used to locate the feed horn at the designed (i.e., center-fed or offset-fed) position in front of the array. This support structure may also cause additional blockage and multiple reflections depending on the material used and the shape of the strut. In order to include the blockage from the support structure, the IB simulation must be carried out with the entire structure, including the support strut, which is shown in Figure 3.4. An acrylic material was used for the support strut in the experiment, and the dielectric constant of acrylic was assumed to be $\epsilon_r = 3.9$ at Ku band. In order to reduce the blockage from the support structure of acrylic material, two wood bars were used in front of the array to hold the feed horn, since the dielectric constant of wood ($\epsilon_r = 1.4$) is lower than the acrylic.

The calculated radiation pattern including the support strut is herein referred to as *IB+strut* and is plotted in Figure 3.5. By comparing the IB and IB+strut results, we can see that the added support strut causes a slightly broadened beamwidth and additional sidelobes emerging around $\pm 20^\circ$ and $\pm 40^\circ$ in the radiation pattern.

To verify the accuracy of the simulations, the reflectarray was then fabricated and measured in a far-field anechoic chamber at the University of Oklahoma. In the measurements, a standard horn in Ku band was used as the source antenna and then the receiving patterns of the test reflectarray antenna were measured. The measured antenna pattern in the E-plane cut is shown in Figure 3.5. Through comparisons between the IB, the IB+strut, and the measurement results, we can see that both the calculated IB and IB+strut simulations are in good agreement with the measured results near the broadside direction in terms of the beamwidth and the major SLLs. Moreover, observations indicate that the IB+strut result

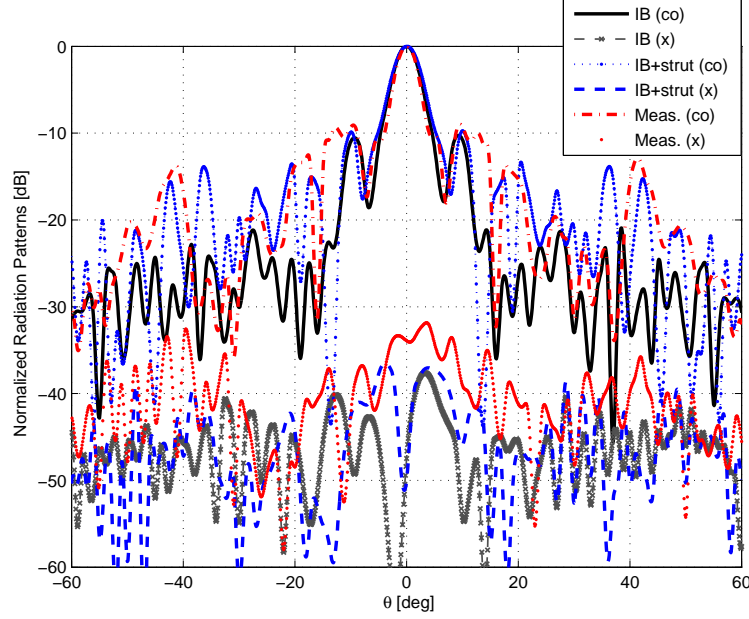


Figure 3.5: Simulations and measurements of antenna radiation patterns at 13.325 GHz in E-plane. Calculated *integrated blockage*, *integrated blockage* with strut and the measured radiation patterns.

more closely matches the measurement results at those areas off the broadside direction.

The simulations were accomplished on a computer with an 8-core CPU (2 GHz) and 32 GB RAM. Key parameters of the simulation, the measurement results, and the time and peak memory consumption comparisons are summarized in Table 3.1. Note that the DLB computation was based on the assumption that the ZB radiation pattern of the reflectarray was already obtained as a far-field source. In Table II, we see that as the blockage analysis schemes become more complex, the simulation time increases accordingly, and the calculated radiation patterns are also closer to the measurement results. For the proposed DLB, RLB, and OLB schemes, the DLB method consumes the least computational resources (i.e., time and memory) and provides a rough prediction of the radiation

Table 3.1: Summary of the simulation and measurement results

	BW ($^{\circ}$)	SLLs (dB)		X-pol. (dB)	Simu. time (h)
ZB	5	-17.26	-17.52	-45.59	7
DLB	5.95	-11.52	-11.5	-36.94	7+0.1
RLB	5.4	-12.38	-12.48	-45.75	12.3
OLB	5.2	-11.22	-11.32	-42.22	11.4
IB	4.7	-10.55	-10.27	-47.47	22
IB+strut	5	-9.89	-9.75	-49.46	76.8
Meas.	4.2	-9.35	-9.16	-33.91	-

properties. The OLB method generates the most accurate prediction while using relatively more computational resources. As the support strut of the reflectarray also has blockage impact on the radiation patterns, especially in the area off the mainbeam direction, the proposed schemes of DLB, RLB, and OLB can be further improved if the support structure is included at the cost of increased computing time.

In summary, a tradeoff occurs between the accuracy and efficiency of simulating the far-field radiation patterns of a reflectarray. Using DLB, RLB, and OLB schemes, the performance of the reflectarray can be estimated quite accurately near the main beam direction with much lower requirements on computational resources as compared to full-wave simulation of the entire structure.

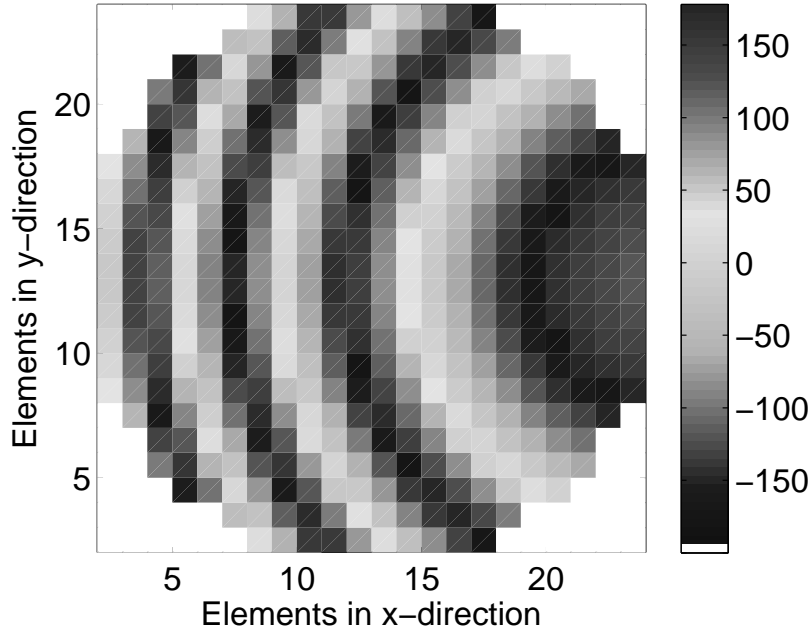
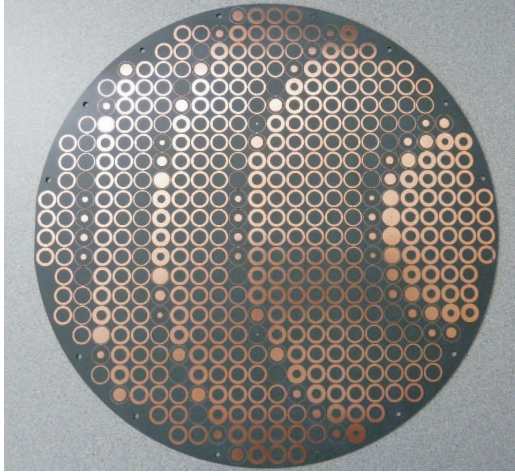


Figure 3.6: Required phase distribution on the designed reflectarray with a tilted beam at 18° .

3.4 Reflectarray with Tilted Main Beam

Although the main focus of this communication is to characterize the blockage effect for a reflectarray, how to reduce the feed blockage effects is also a natural follow-on question. As one of the solutions, the blockage can be mitigated by tilting the main beam certain degrees off broadside, depending on the aperture size of the feed horn and the focal length. To illustrate, another reflectarray antenna is designed with tilted beam at 18° to minimize the blockage from the center-fed horn. This reflectarray adopts the same array size and focal length as the broadside reflectarray.



(a) Zero blockage



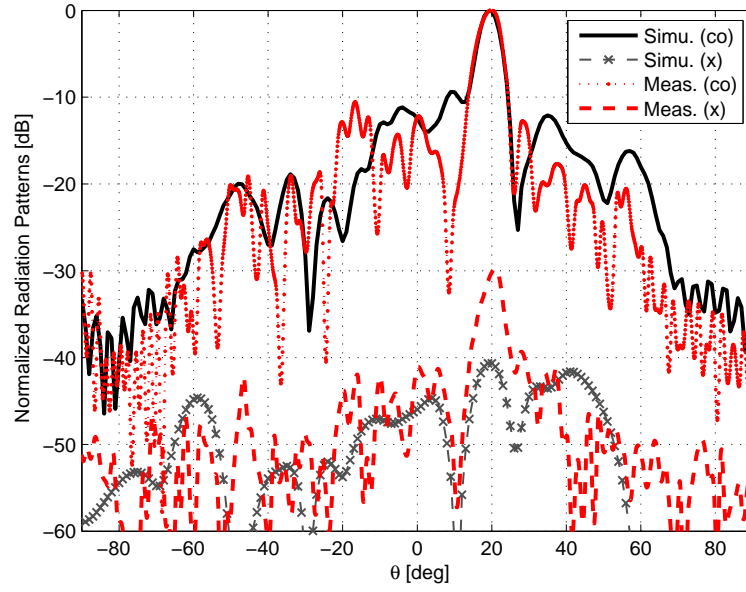
(b) Data-link blockage

Figure 3.7: Prototype of the designed reflectarray with a tilted beam at 18° , (a) front view and (b) side view.

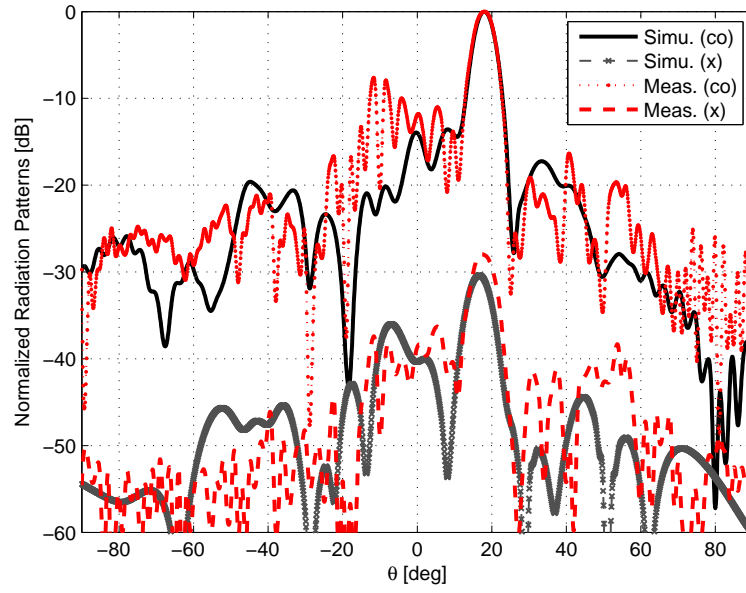
For a reflectarray with tilted main beam, the desired beam direction is set to $\theta_b = 18^\circ$ and the phase distribution can be obtained using Equation 2.12. The calculated phase distribution for the reflectarray with a tilted beam is shown in Figure 3.6.

A prototype of the beam tilting reflectarray is shown in Figure 3.7. An air layer is introduced by using the nylon spacers between the substrate layer and the metal ground plane, and the array panel is then affixed onto the ground plane with plastic screws fastened through the spacers at the edge.

Also from Figure 3.7 (a) we can see that the majority of the elements are ring element, which can generate a phase range from -132° to 188° via varying the ring radius. The ring-patch elements are used in the area where the required phase is in the range from 188° to 230° . The ring-patch elements are used as a complementary design besides the ring element in order to achieve a broader phase range.



(a)



(b)

Figure 3.8: Simulated and measured radiation patterns of the reflectarray with a tilted beam at 18° at (a) 12.5 GHz, (b) 13.325 GHz.

The simulation and measurement results of this reflectarray, including the radiation patterns at different frequencies for the E -plane, are shown in Figure 3.8 and Figure 3.9. The *data-link* approach is used in the simulations for efficient computation. In Figure 3.8 and Figure 3.9, it can be observed that the measurement results are in good agreement with the simulations at different frequencies. The blockage effect from the center-fed horn is avoided, and the performance of the reflectarray can be predicted accurately and efficiently using the DLB approach.

The measured wideband gain of the reflectarray is also shown in Figure 3.10. The designed reflectarray has a good wideband gain performance from 12.5 GHz to 14 GHz.

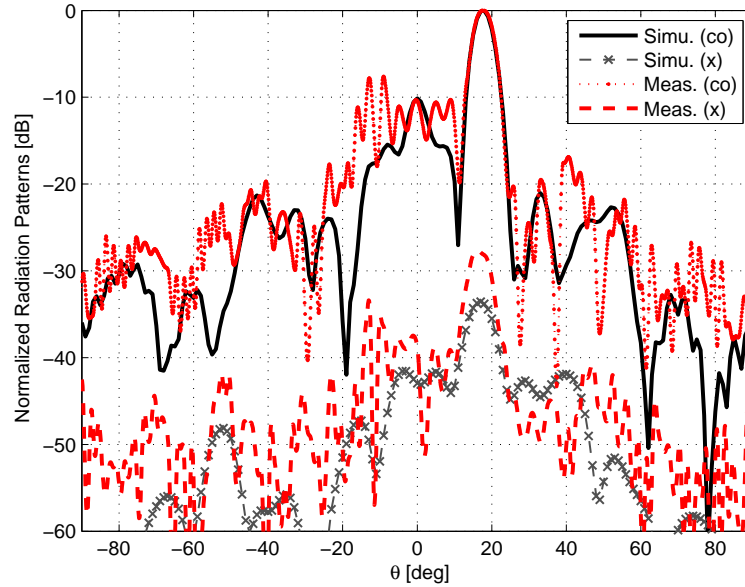


Figure 3.9: Simulated and measured radiation patterns of the reflectarray with a tilted beam at 18° at 13.5 GHz.

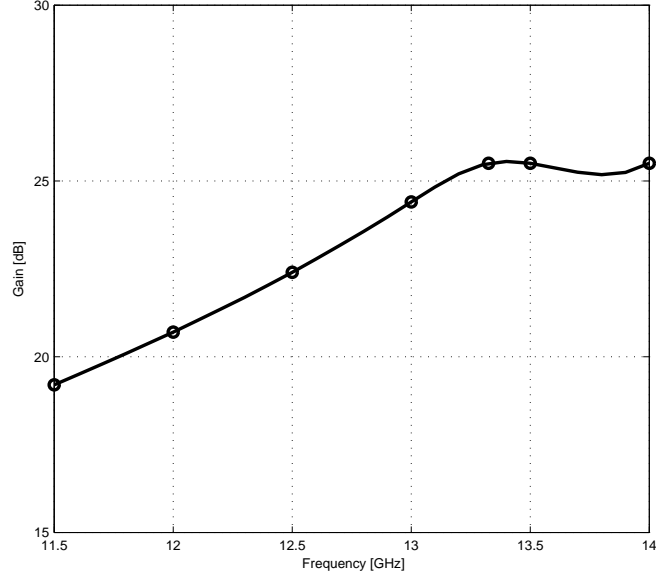


Figure 3.10: Measured wideband gain of the reflectarray with a tilted beam at 18° .

3.5 Conclusion

Radiation beam blockage is a challenge to reflectarray designs and it is more difficult to analyze than parabolic dish antennas. The radiation patterns of a center-fed reflectarray using different modeling schemes are compared. The radiation patterns, including the blockage from the feed horn, can be predicted efficiently and accurately via DLB, RLD, and OLB methods despite the differences in simulation time and required computer memories. Other factors, such as subreflectors and support struts, can also be included to further improve the accuracies of predictions. In addition, the reflectarray with a tilted main beam is suggested as a solution to mitigate the blockage effect. For this example, the measurement results are in good agreements with the simulated results using the DLB approach.

Chapter 4

A Reflectarray Design with Reduced Cross-Polarization for Polarimetric Radar

4.1 Introduction

The reflectarray combines some of the best features of parabolic reflectors and the conventional antenna arrays, such as low physical profile and low fabrication cost. It also eliminates the losses associated with beam-forming networks and expensive TR modules of phased array antennas. Those make reflectarray a possible candidate for weather radar applications.

As discussed in Section 1.3.1, reflectarrays have various forms of elements to achieve a planar phase front. Some element examples are shown in Figure 4.1. In Figure 4.1 (a), the variable-length phase delay lines attached on the microstrip patches can provide different compensation for the phase delays over the paths from the illuminating feed [86]. Another way is to use variable-sized patches, dipoles, or rings such that elements can have different scattering impedances and thus different phases to compensate for the different feed-path delays [13, 52, 87]. Moreover, elements with different angular rotations can also be used to compensate for the feed path-length differences for circularly polarized reflectarray [21].

In the three types of reflectarrays, the reflectarrays with variable-sized elements exhibit superior cross-polarization performance, due to the reduction of leakage radiation from the phase delay lines shown in Figure 4.1 (a) [4]. This has

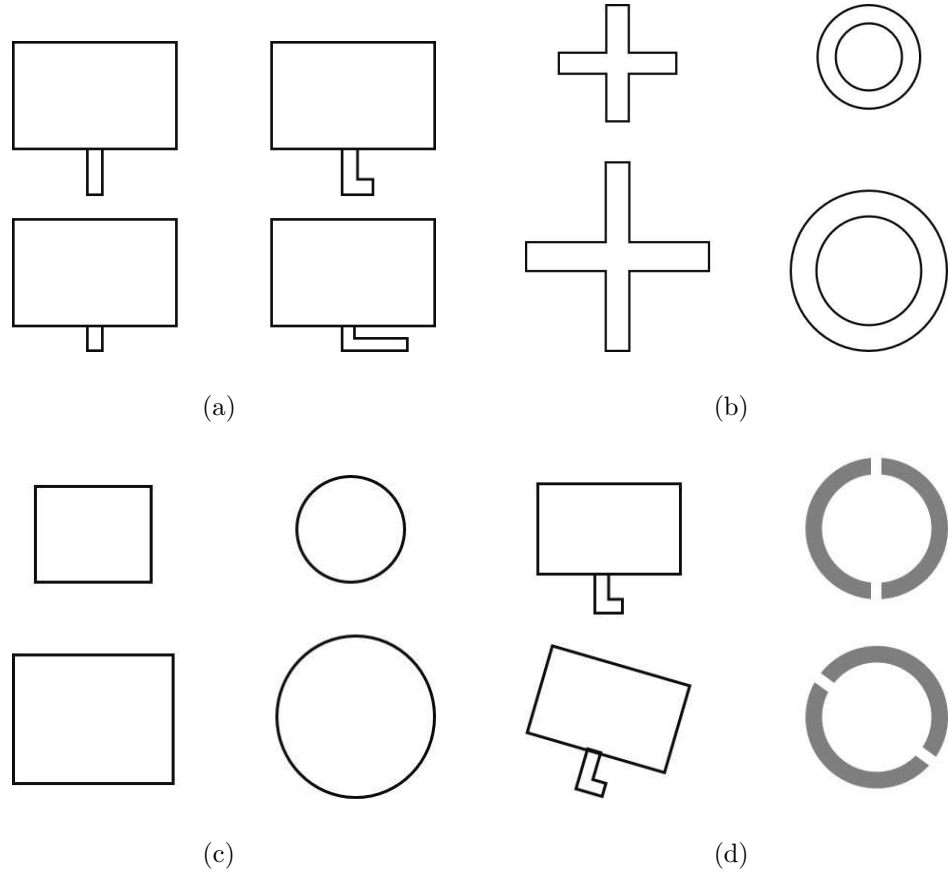


Figure 4.1: Various reflectarray elements, (a) identical patches with variable-length phase delay lines, (b) variable-sized dipoles or rings, (c) variable-sized square patches or circular patches, (d) variable angular rotations. [4]

made this type of reflectarray antenna a promising choice for the application of precipitation detection in weather radar.

The most important polarimetric variables of weather measurements include the differential reflectivity Z_{DR} , co-polar correlation coefficient magnitude ρ_{hv} , and specific differential phase K_{DP} , etc. [88]. These polarimetric variables represent differences in the amplitude and phase of the horizontally (H) and vertically (V) polarized backscatter from hydrometeors.

Due to the scatterer's axis ratio, the H-pol and V-pol backscatter differences are usually very small. For instance, the axis ratio of typical oblate rain drops is not too different from unity. Therefore, good accuracy in measurement is required to provide meaningful information for hydrometeor classification (i.e., rain, snow, hail, etc.) and quantitative estimation of precipitation fall rates [89].

To meet the accuracy requirement, a dual-polarized mode of operation is being adopted extensively for weather detection. Moreover, the precipitation observation dual-polarized measurements relies on complete isolation of orthogonal components of the fields, and negligible levels of cross-polarized radiation along the beam axis need to be maintained (i.e., more than 40 dB below the co-polarization peak) [89]. Zrnic indicated in [90] that if the cross-pol level of an antenna is 40 dB below the co-pol peak, and if the SHV data collection mode (Simultaneously energizing the H and V antenna ports on transmit, and simultaneously receiving H and V backscatter radiation) is used (i.e., the mode used by the WSR-88D), it is shown that the differential reflectivity Z_{DR} bias can be about ± 0.35 dB for rain rates $R \leq 10$ mm/h.

In this chapter, an effective method for cross-polarization suppression in reflectarray using the gapped double-ring elements is proposed. With the gapped double-ring design, the surface currents on the inner ring and outer ring will be

enhanced at the co-polarization radiation direction and also cancel each other at cross-polarization radiation, so the cross-polarization level is suppressed [91, 92]. Measurement results of the new design show 10 dB reduction in cross-polarization level at the broadside direction at 13.325 GHz by cutting gaps on the double-ring elements. The measured cross-polarization level of this new design is about -44 dB at broadside and less than -33 dB in all other directions.

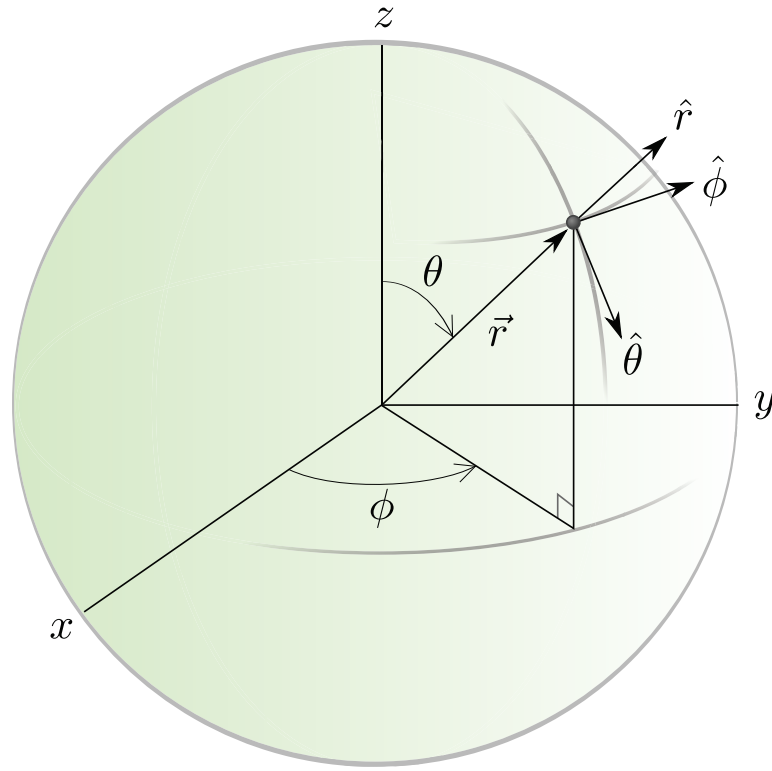


Figure 4.2: Coordinate systems for cross polarization definitions. Radiation source is in the $x - y$ plane.

4.2 Definitions of Cross-Polarization

The term of cross-polarization arises because an antenna is never 100% polarized in a single mode (linear, circular, etc) [93]. In addition to the polarization mode it is designed to operate, every antenna has a radiation leakage in the perpendicular (or orthogonal) polarization direction. Hence, two radiation patterns of an antenna are present simultaneously, including the co-polarization (or desired polarization component) radiation pattern and the cross-polarization radiation pattern (the perpendicular polarization to the desired polarization).

In other words, co-polarization represents the polarization the antenna is intended to radiate or receive while cross-polarization represents the polarization orthogonal to the co-polarization [2]. Three different definitions of cross polarizations given so far by Ludwig in [94] are briefly presented below. This will be done by deriving unit vectors \hat{u}_{ref} and \hat{u}_{cross} , where \hat{u}_{ref} represents the reference polarization (which is usually the co-polarization) of electric field \mathbf{E} and \hat{u}_{cross} represents the cross polarization of \mathbf{E} .

The first definition is referred to as *Ludwig-1*: in a rectangular coordinate system, the two polarizations are the projections of the electric field vector onto the two Cartesian unit vectors \hat{x} and \hat{y} lying in the aperture plane. One unit vector is taken as the direction of the reference polarization, for example, y axis in Figure 4.2, and another as the direction of cross polarization, which is the x axis in Figure 4.2.

$$\left\{ \begin{array}{l} \hat{u}_{ref}^{(1)} = \hat{y} \\ \hat{u}_{cross}^{(1)} = \hat{x} \end{array} \right. \quad (4.1)$$

The second definition is referred to as *Ludwig-2*: in a spherical coordinate system as shown in Figure 4.2, the two polarizations are the projections of the electric field vector onto the two spherical unit vectors given by [94]:

$$\begin{cases} \hat{u}_{ref}^{(2)} = \frac{\sin \phi \cos \theta \hat{\theta} + \cos \phi \hat{\phi}}{\sqrt{1 - \sin^2 \theta \sin^2 \phi}} \\ \hat{u}_{cross}^{(2)} = \frac{\cos \phi \hat{\theta} - \sin \phi \cos \theta \hat{\phi}}{\sqrt{1 - \sin^2 \theta \sin^2 \phi}} \end{cases} \quad (4.2)$$

The third definition is referred to as *Ludwig-3*: the reference and cross polarization are defined as the fields in measurement when antenna patterns are taken in the common manner.

$$\begin{cases} \hat{u}_{ref}^{(3)} = \sin \phi \hat{\theta} + \cos \phi \hat{\phi} \\ \hat{u}_{cross}^{(3)} = \cos \phi \hat{\theta} - \sin \phi \hat{\phi} \end{cases} \quad (4.3)$$

The use of *Ludwig-1* definition is limited for most of the antenna applications, since the far-field radiation pattern of an antenna is tangential to a spherical surface. Definitions *Ludwig-2* and *Ludwig-3* involve unit vectors tangent to a sphere so they are appropriate for the case of primary or secondary fields [94]. The presented cross polarization definitions are primarily defined for either electric, magnetic dipole or horn antennas, and different polarization definitions have their corresponding optimal sources. The *Ludwig-3* definition corresponds to the standard antenna measurement practice and is ideal for testing feed horn antennas or small aperture antennas [94, 95], but the *Ludwig-3* is not optimal for electric and magnetic dipoles [96]. At the same time, the *Ludwig-2* definition is optimal

for H -field aperture source and not appropriate for pyramidal or corrugated horn antennas [94].

For the design presented in this Chapter, we used *Ludwig-2* definition for the calculation of cross-polarization in the simulation and measurement. For a X-polarized antenna oriented in the X-Y plane, as shown in Figure 2.13, the co-polarization component is E_ϕ and the cross-polarization component is E_θ . For a Y-polarization antenna oriented in the X-Y plane, the co-polarization component is E_θ and the cross-polarization component is E_ϕ [97].

Recently, several designs have been proposed to reduce the cross-polarization in reflectarrays [98–101]. In [98], a reflectarray with microstrip patches and delay lines was designed, and by arranging the delay lines in a mirror-symmetric configuration, the cross-polarization is reduced at the direction of the main beam. In [99], the farfield cross-polarization is further suppressed by employing the mirror symmetry configuration in all adjacent elements; that is, each element is the immediate mirror of its neighboring elements in both x and y directions. In this way, the radiated fields of the elements would eliminate the farfield cross-polar component, since the directions of currents responsible for cross-polarization are all opposite and thus may cancel each other out. However, one drawback of patch elements with tuning stubs is the possibly degraded cross-polarization performance due to the radiation leakage from the microstrip stubs, which contributes to the cross-polarization field. Also, the elements with stubs have more power loss than the variable size elements. In [100, 101], it is demonstrated that through synthesis of unit cell dimensions to produce a cancellation of cross-polar reflective field in which maximum cross-polarization is achieved. This approach requires a more sophisticated synthesis of reflective cells and much finer control of all field components in both phase and magnitude.

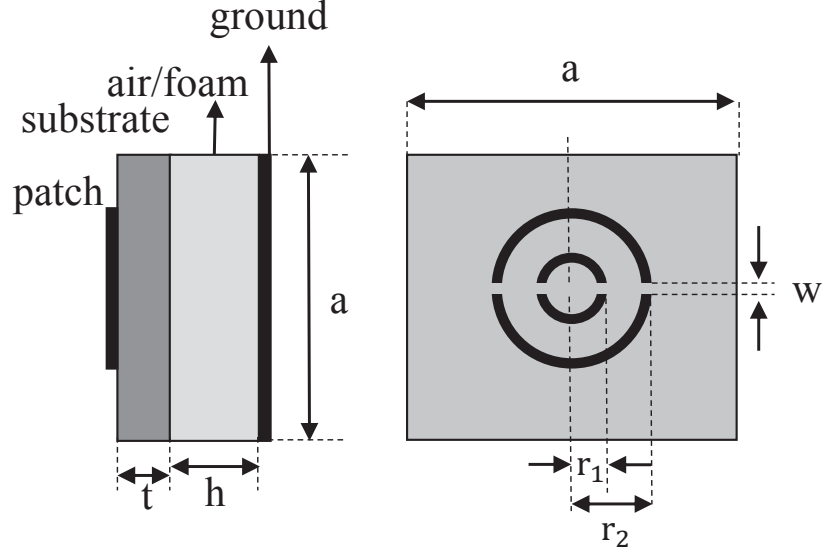


Figure 4.3: Double-ring element configuration for lower cross-polarization.

In this work, a more effective method for cross-polarization suppression in reflectarray using the gapped double-ring elements is proposed. With the gapped double-ring design, the surface currents on the inner ring and outer ring will be enhanced at the co-polarization radiation direction and also cancel each other at cross-polarization radiation, so the cross-polarization level is suppressed.

4.3 Element Design

A variable-sized ring configuration is adopted for the element design, and different reflection phases are achieved by varying the ring dimensions. The configuration of the double-ring element is shown in Figure 4.3. The ring element design eliminates the need for tuning stubs for phase variation, and thus the leakage radiation associated with the microstrip stubs is mitigated. A double-ring element configuration is used to extend the reflection phase range. Since a double resonant

Table 4.1: Dimensions and parameters of the low cross-polarization double-ring reflectarray.

Parameter	Value
Center Frequency	13.325 GHz
Unit cell size a	12.6 mm
Substrate RO5880 height t	1.575 mm
Air/foam layer height h	1 mm
Radius of inner ring r_1	1.7 mm \rightarrow 2.7 mm
Inner to outer ring radius ratio I/O	0.7
Radius of outer ring r_2	$r_1/(I/O)$

response can be obtained from the concentric rings, a much larger phase range will be generated than that of a single-ring element, and thus a broadband frequency operation can be achieved [16, 102].

The reflectarray unit cell was designed at center frequency of 13.325 GHz. The unit cell has a size $a = 12.6$ mm. The radius of the inner ring r_1 is changed to generate the variable phases. Rogers RO5880 laminate with $\varepsilon_r = 2.2$ and thickness $t = 1.575$ mm is used as the substrate. An air/foam layer with thickness $h = 1$ mm is inserted between the substrate layer and the ground plane to enhance the linearity of the phase curve [24]. The dimensions and parameters of the element design are given in Table 4.1.

Figure 4.4 shows the simulated reflection phase responses for normal incidence of plane wave obtained by CST Studio[®]. The reflection phases of the element are determined by performing the WGS method on the unit cell. The resonant

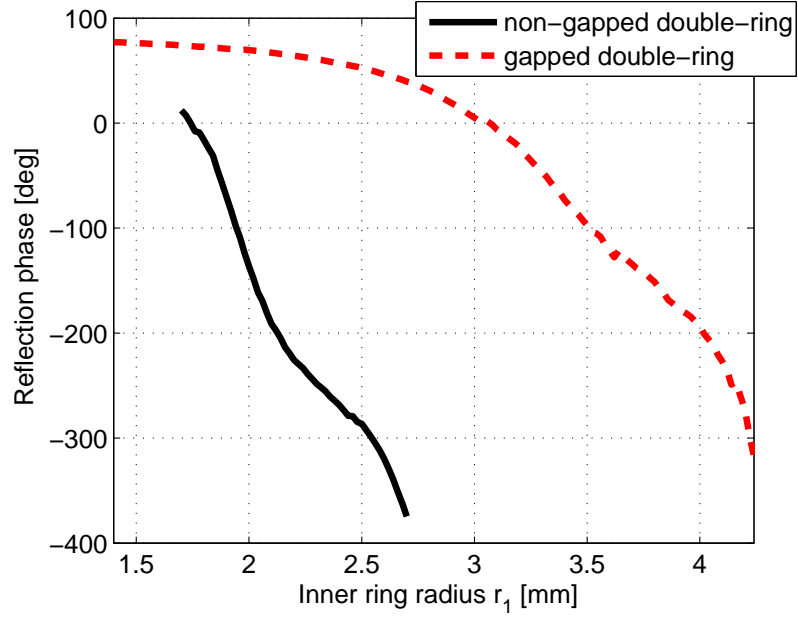


Figure 4.4: Simulated reflection phases of the double-ring element.

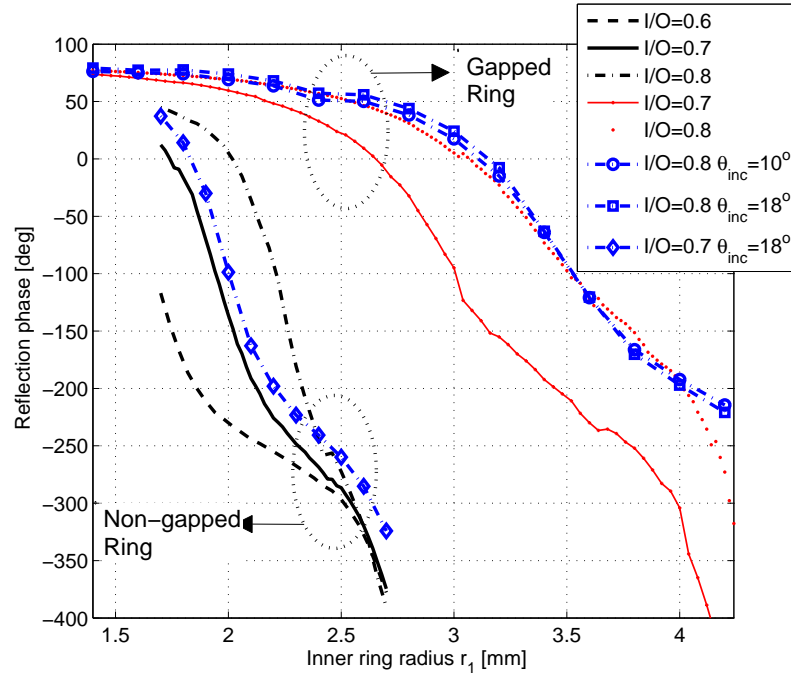


Figure 4.5: Simulated reflection phases of the double-ring element with different radiuses ratio I/O .

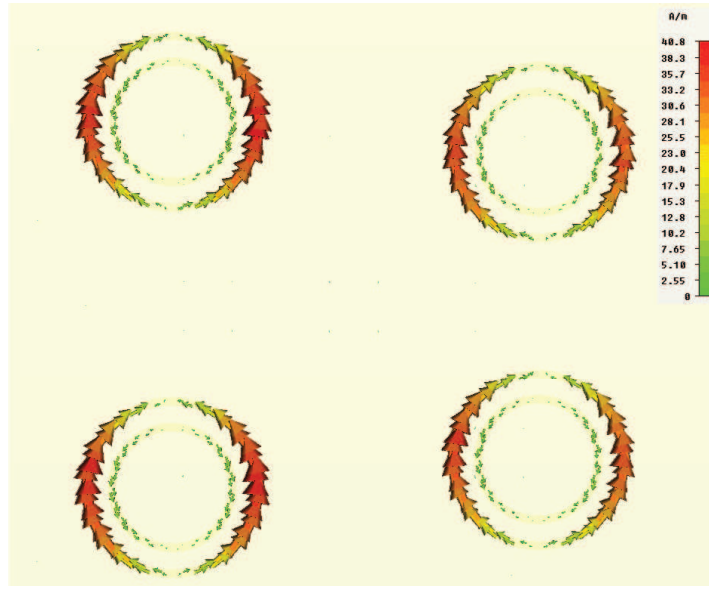
responses between the concentric rings provide a wide phase range which exceeds 390° , which is sufficient for reflectarray design.

In the early design stage, the ratio of the inner and outer ring radii (I/O), r_1 and r_2 in Figure 4.3, was selected to be 0.6, 0.7 and 0.8 for the non-gapped double-ring element in the simulations. The phase curves for each ratio I/O were calculated, respectively, as shown in Figure 4.5. The unit cell with a ring radius ratio I/O of 0.7 shows a better linearity of phase variation and also a broad phase range over the other two I/O ratios, when the inner ring radius r_1 is varied between 1.7 mm and 2.7 mm. Thus, $I/O = 0.7$ was adopted in the design for the non-gapped double-ring elements.

4.4 Surface Current Simulation

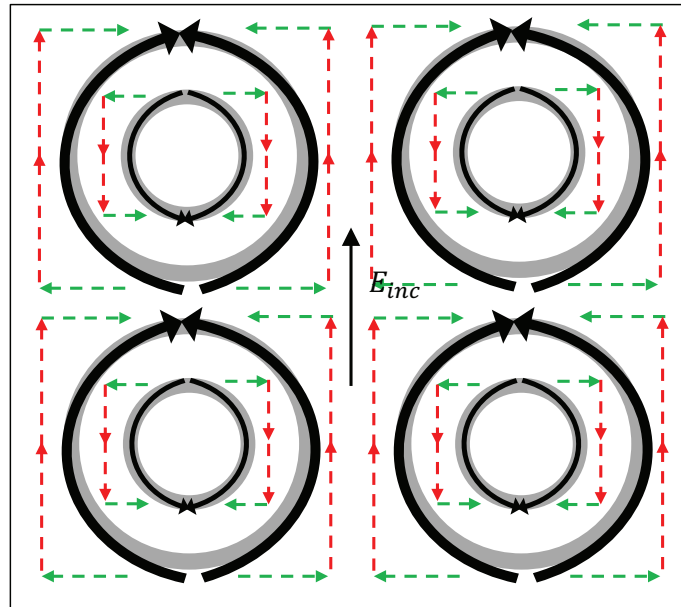
In either reflectarray or phased array antennas, one of the contributors to the cross-polarization is the leakage radiation of the surface current components. Methods for cancelling the cross-polar components of electric fields were developed for reflectarray with the incorporation of mirror arrangements of the array elements [98]. In this design, the surface currents of the elements in an array configuration were also simulated to investigate their contributions to cross-polarization radiation.

Extensive simulations of smaller reflectarrays of non-gapped double-ring elements were carried out in CST. Figure 4.6 (a) shows the simulated surface currents for a typical configuration, and the co-polar and cross-polar components are illustrated in Fig 4.6 (b), where Co-polar components are shown in red-color arrows, and cross-polar components are shown in green-color arrows. We can see that the directions of the surface currents on the inner ring and outer ring



(a)

PBC



(b)

Figure 4.6: Simulated surface currents of the non-gapped double-ring elements with periodic boundary conditions (PBC), (a) Surface currents on the 2×2 double-ring elements. (b) Illustration of the Co-polar and Cross-polar components of (a).

for each individual element are inverse. For a single element, on the outer ring the two cross-polar components on the left side have inverse directions compared with the two cross-polar components on the right half; thus, such cross-polar components will cancel each other. In the following discussion, the cancellation inside one element will be referred as *self-cancellation*, and the cancellation between adjacent elements will be referred as *mutual-cancellation*. Moreover, if the components combine constructively inside or between the elements, it can be referred as *self-construction* or *mutual-construction*.

From Figure 4.6 (b) we can see that for cross-polar components the self-cancellation exists on both inner ring and outer ring of a single element. Moreover, the mutual-cancellations of the cross-polar components between the neighboring elements can be clearly observed. This mutual-cancellation is also helpful for the cross-polarization suppression. Thus, the simulation results indicate that the cross-polar components would cancel each other inside and between the elements.

In regard to the co-polar components, which have the same direction as the incident electric field E_{inc} , a mutual-construction can be observed between the elements. However, the co-polar components inside a single element are reverse between the inner ring and outer ring. This results in some self-cancellation of the co-polar components, which will degrade cross-polarization performance. To suppress the cross-polarization radiation, further improvement on the element design is necessary, to achieve not only a self/mutual-construction on the co-polar components but also a simultaneous self/mutual-cancellation on the cross-polar components.

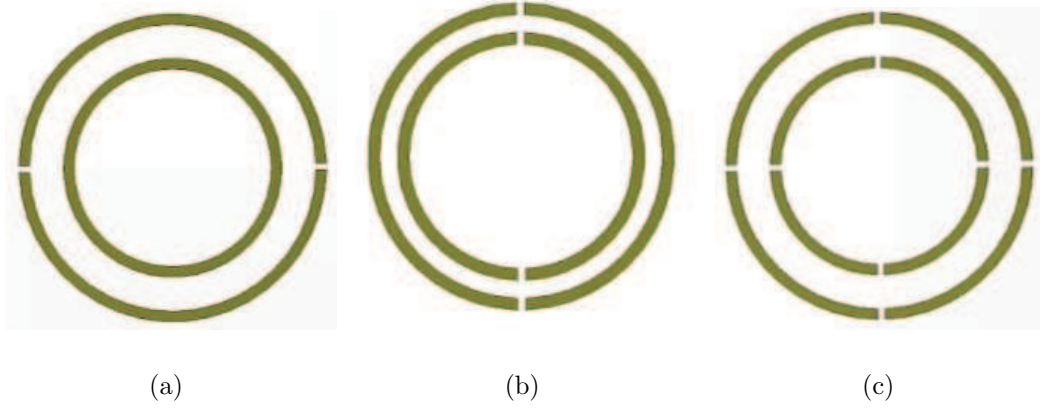


Figure 4.7: Gaps are cut on the rings to change the directions of surface currents, (a) gaps are cut on the outer ring only, (b) gaps are cut on both the inner and outer rings and (c) two pairs of gaps are cut on both the inner and outer rings.

4.5 Cross-Polarization Suppression Using Gapped Ring Elements

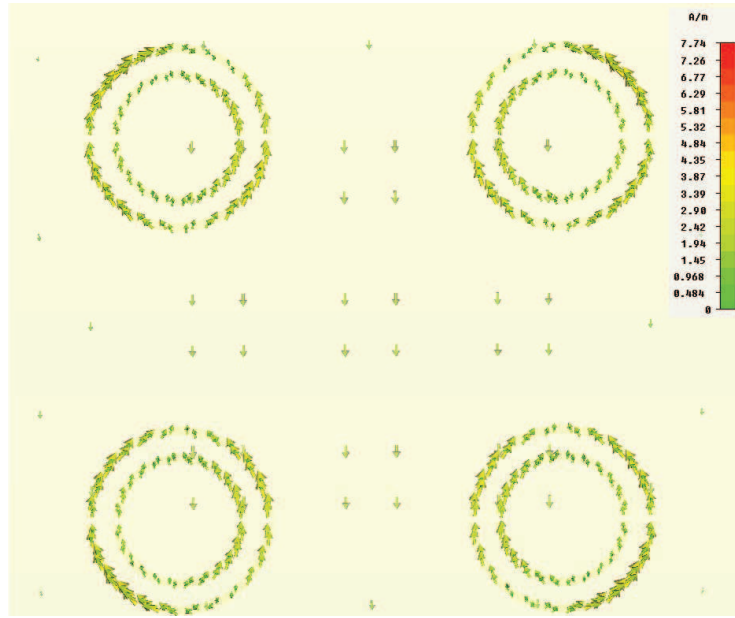
By cutting gaps on the double-ring element, the surface currents' directions can be reversed on the rings. Different element configurations, as shown in Figure 4.7, were tried in simulations, including elements with a single gap, a pair of gaps and multiple gaps cut on either the inner ring or outer ring or both. Modeling results indicate that the configuration with a pair of gaps cut on both the inner ring and outer ring, as shown in Figure 4.7 (b), is the most optimal configuration for the cross-polar components' cancellation of the surface currents.

To verify this, the reflection phase responses of the unit cell with gapped double-ring configuration were first simulated. A gap size $W = 0.2$ mm was adopted in the design. The reflection phases from a normal incident plane wave are plotted in Figure 4.4. When the inner ring radius is varied between 1.4 mm and 4.2 mm, the phase range covers about 350° . Although the phase range is

smaller than that of the non-gapped double-ring element, it is still acceptable for the reflectarray design. Moreover, the ratio of the inner and outer ring radiuses (I/O) is varied in the simulation and the I/O effect on the phase curve is shown in Figure 4.5. A ring radius ratio $I/O = 0.8$ was adopted in the gapped double-ring element due to the better phase linearity than the unit cell with $I/O = 0.7$.

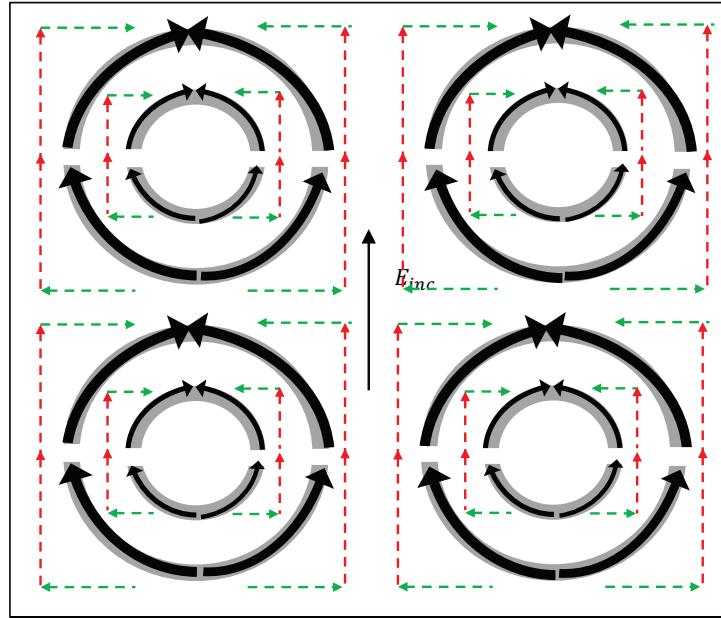
The surface currents of a 2-by-2 reflectarray using the gapped double-ring elements were also simulated, which are shown in Figure 4.8 (a), and the co-polar and cross-polar components of the surface currents are given in Figure 4.8 (b). We can observe that with a pair of gaps cut on the double-ring element, the surface currents on the inner ring are reversed compared to that in Figure 4.6 (a), and thus have the same direction as on the outer ring. In Figure 4.8 (b), we can see that the cross-polar components would still cancel each other both inside and between the elements. Furthermore, the co-polar components for a single element are converted to have the same direction. Thus a self/mutual-construction on the co-polar components and also a simultaneous self/mutual-cancellation on the cross-polar components are achieved on the new design.

The radiation patterns of this 2-by-2 reflectarray using the original non-gapped double-ring and new gapped double-ring elements were also simulated and compared to study the cross-polarization suppression performance. Since the simulation of a big reflectarray with hundreds of elements costs computing time as well as computer resources, it is necessary to take a preliminary study on a small scale array. The radiation patterns of the 2-by-2 reflectarray are compared in Figure 4.9. It is clearly shown in Figure 4.9 that, with the gaps cut on the double-ring elements, cross-polarization nulls show up at and around broadside ($\theta = 0^\circ$). The cross-polarization level is successfully suppressed by using the new



(a)

PBC



(b)

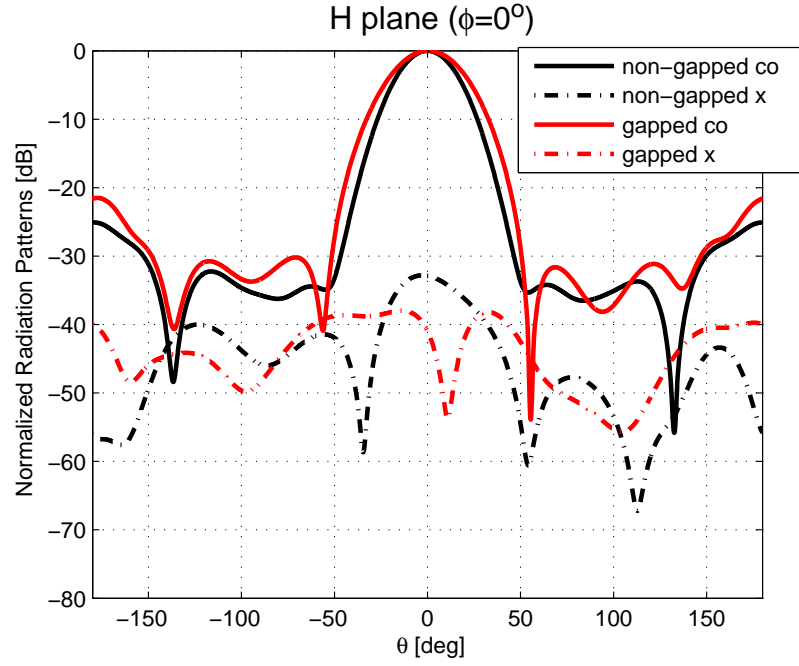
Figure 4.8: Simulated surface currents of the new gapped double-ring elements with PBC, (a) Surface currents on the 2×2 gapped double-ring elements. (b) Illustration of the Co-polar and Cross-polar components of (b).

gapped double-ring elements design. It is worth noting that the new elements design has a little bit degradation on the beamwidth and SLLs, possibly induced by the discontinuous surface currents due to the gaps cut on the elements.

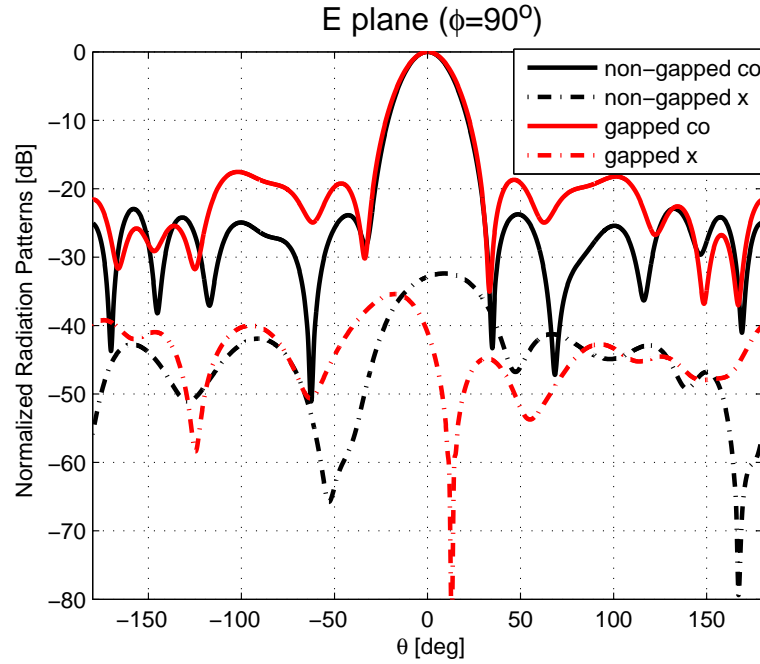
4.6 Reflectarray Design Example

To demonstrate the performance of cross-polar suppression using the gapped double-ring elements, two full-size circular reflectarrays with a diameter $D = 305$ mm were designed with non-gapped and gapped double-ring elements, and both simulation and measurement results were compared. An optimized focal point $f/D = 1.5$ is chosen for the feed horn, considering both maximum aperture efficiency and antenna setup size. Both of the reflectarrays use center-fed horns and are designed for broadside radiation. The reason for the choice of center-fed method was to keep a symmetric antenna structure, which could simplify the designs and be helpful for cross-polarization reduction. The cross-polarization suppression using gapped elements would also apply to offset-fed reflectarrays.

In the presented design, the dimensions of all elements are calculated based on the phase curve with a normal incidence, with the assumption that the phase curves of a single layer unit cell are similar to those of the normal incidence when the scan angles are in the range not exceeding 30° to 40° [74]. Nevertheless, this assumption was also verified on the reflection phases for squint incident angles. Figure 4.5 also shows the phases curves for incident angles of $\theta_{inc} = 10^\circ$ and 18° off broadside direction for both gapped and non-gapped element configurations. Note that $\theta_{inc} = 18^\circ$ is the largest incident angle for the elements on the edge in the presented design. As seen in Figure 4.5, for the whole range of the inner ring radius r_1 , the maximum phase deviation is about 15° , which indicates that the



(a)



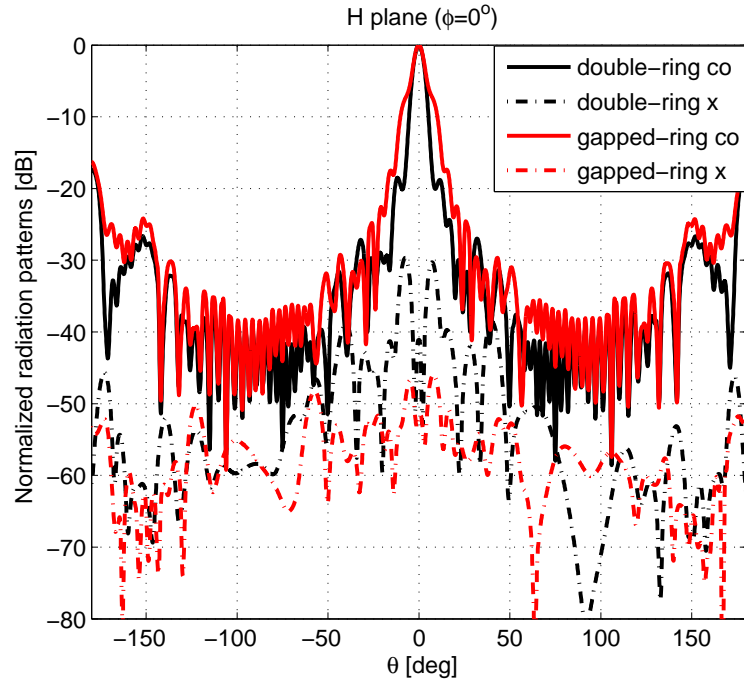
(b)

Figure 4.9: Comparison of the simulated radiation patterns of the 2 by 2 reflectarrays with non-gapped and gapped double-ring elements, (a) H-plane patterns and (b) E-plane patterns.

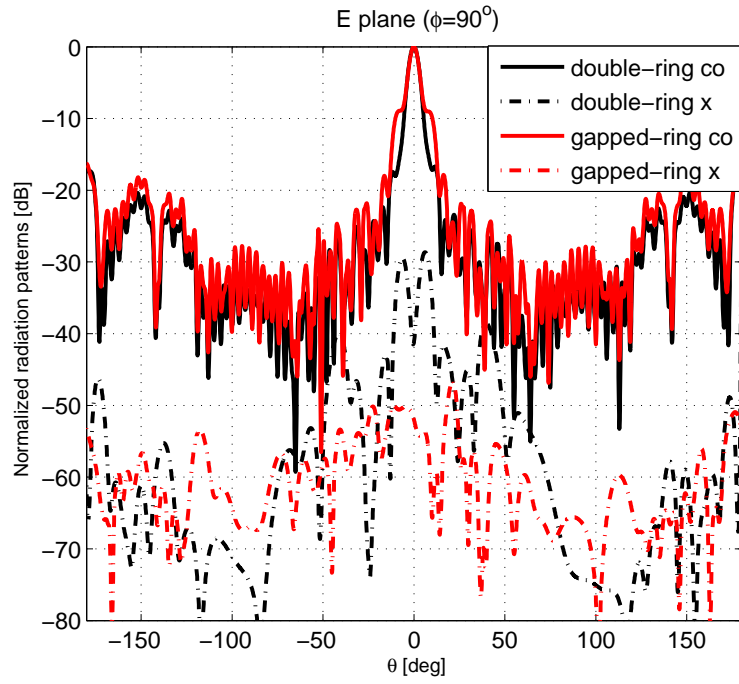
phase responses of the normal incidence can provide a reasonable estimation for the presented design.

Full-wave electromagnetic simulations on the 24-by-24 reflectarrays were carried out using the Integral Equation Solver of CST. The simulated farfield radiation patterns of the reflectarrays are shown in Figure 4.10. It can be observed that, with the non-gapped double-ring elements, the cross-polarization level of the farfield radiation pattern is -41.2 dB at broadside for both H plane and E plane cuts, in comparison the reflectarray design with gapped double-ring elements shows much lower cross-polarization level -52 dB for both H plane and E plane cuts, attributed to the cancellation of the cross-polar components in radiation. Generally, the simulation shows 11 dB reduction in the cross-polarization level of the radiation pattern at and around broadside. The simulated results for other antenna parameters are summarized in Table 4.2, from which we can also see there are some tradeoffs with the new design, such as the gain loss, the broadened beamwidth and slightly higher SLL. Those tradeoffs are probably due to the discontinuities of the surface currents and the radiation leakage from the gaps cut on the elements. With further gap optimization, such as by controlling gap dimensions or by connecting a line between two edges of the gap, we possibly can make adjustments to these tradeoffs.

The two reflectarrays were also fabricated so that the simulation results can be verified. Figure 4.11 shows the reflectarray panel with gapped double-ring elements. The $h = 1$ mm air gap between substrate and the ground is realized using nylon screws and pads. The reflectarrays were assembled with a support structure, which ensures the position of the feed horn and the reflectarray panel.



(a)



(b)

Figure 4.10: Simulated farfield patterns of the 24 by 24 reflectarrays with non-gapped and gapped double ring elements, (a) H-plane and (b) E-plane.

Table 4.2: Simulated cross-polarization level of the two reflectarrays with non-gapped and gapped double ring elements.

H plane	Conventional design (dB)	New design (dB)	Improvement(dB)
Broadside	-41	-52	-11
Highest	-30	-46	-16
E plane	Conventional design (dB)	New design (dB)	Improvement (dB)
Broadside	-41.2	-52	-10.8
Highest	-28.6	-46.6	-18

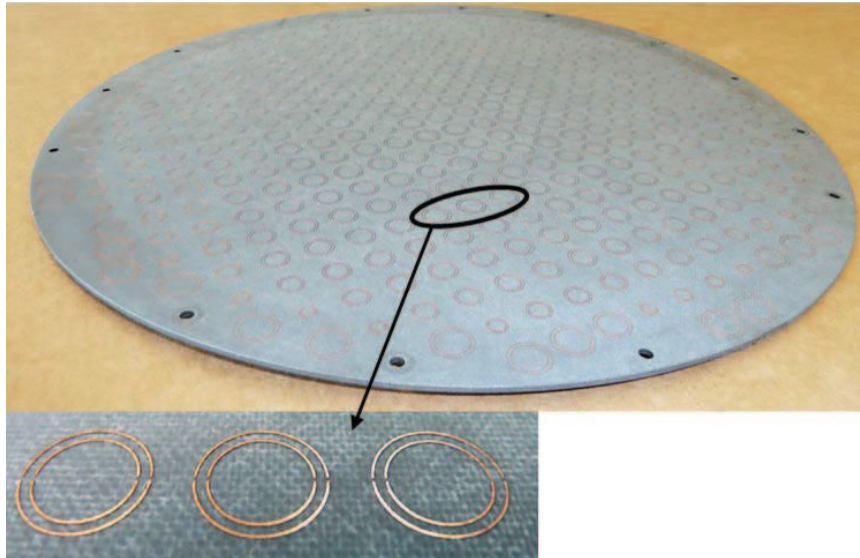
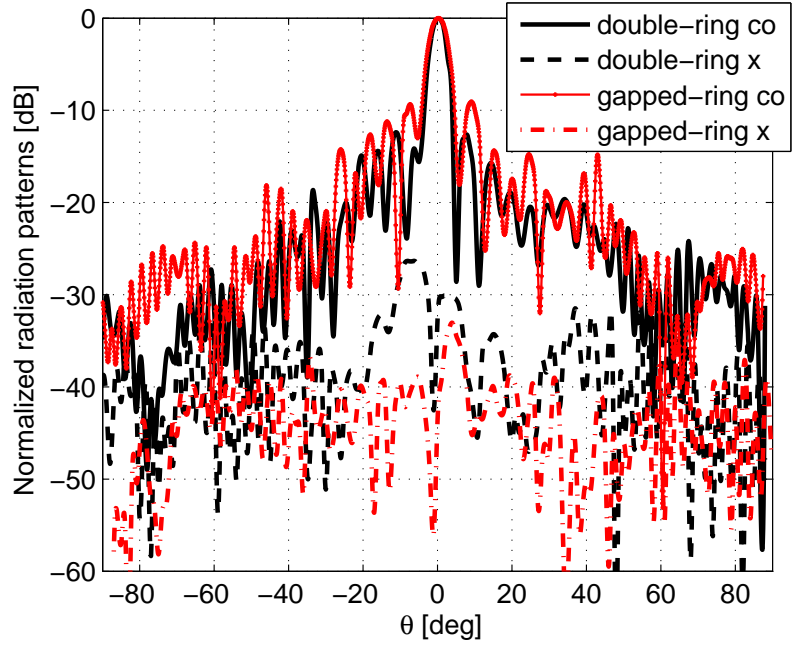


Figure 4.11: Fabricated reflectarray with gapped double-ring elements.

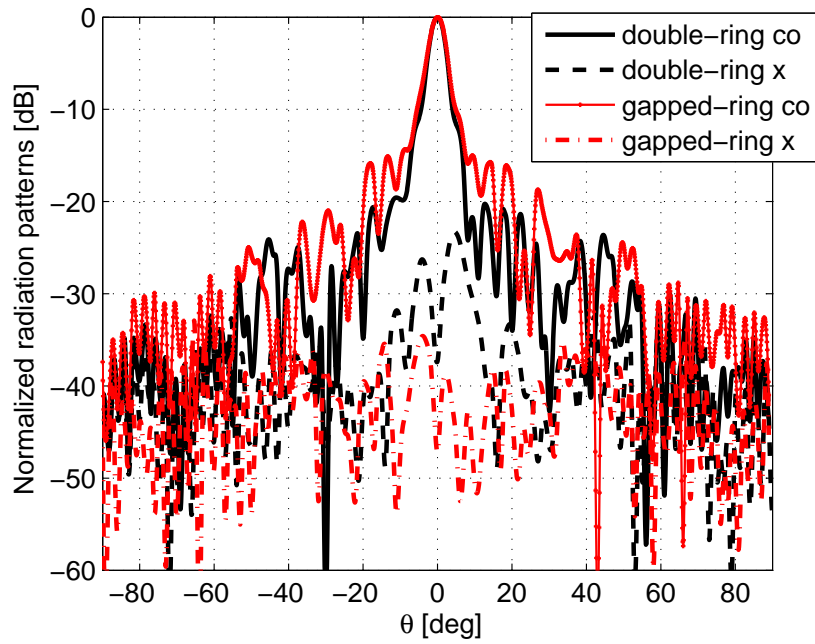
The antenna radiation pattern measurement was carried out in the anechoic chamber at the University of Oklahoma. The measured farfield radiation patterns at 13.325 GHz are given in Figure 4.12.

The measured cross-polarization levels of the new design are slightly higher than the simulated ones but much less than the prior-art designs. It can be seen that the prior-art design with the non-gapped double-ring elements has a cross-polarization level of -37.3 dB below the co-polar peak at broadside for H plane cut and -32.8 dB for E plane cut, while with the new design using gapped double-ring elements, the cross-polarization level at broadside is reduced to -47.1 dB for H plane cut and -43.7 dB for E plane cut. Furthermore, the antenna cross-polarization level is below -33 dB for the entire azimuth angle ranges ($-90^\circ < \theta < 90^\circ$) for both H and E plane cuts. Note that the measured results also show a performance tradeoff of the higher SLL and slightly broadened beamwidth, which is similar to the observation in simulated results. The aperture efficiency of the non-gapped double-ring array is 46.07% at 13.325 GHz, while with the gapped double-ring the efficiency dropped to 38.32%. Lower aperture efficiency on the gapped-double ring array is probably due to the larger size variation of the elements, especially for those elements on the edge. It may be also attributed to the surface currents discontinuity and the consequent radiation leakage from the gaps cut on the elements. By further optimizing the gap sizes, the gain and efficiency can be improved.

The cross-polarization level of the two antennas were also measured at different frequencies from 12.2 GHz to 14.4 GHz and the measured E -plane results are compared in Figure 4.13. The improvements of cross-polarization level are evident for the new design. The reduction of the cross-polarization level varies



(a)



(b)

Figure 4.12: Measured farfield radiation patterns of the 24 by 24 reflectarrays with non-gapped and gapped double ring elements, (a) H-plane patterns and (b) E-plane patterns.

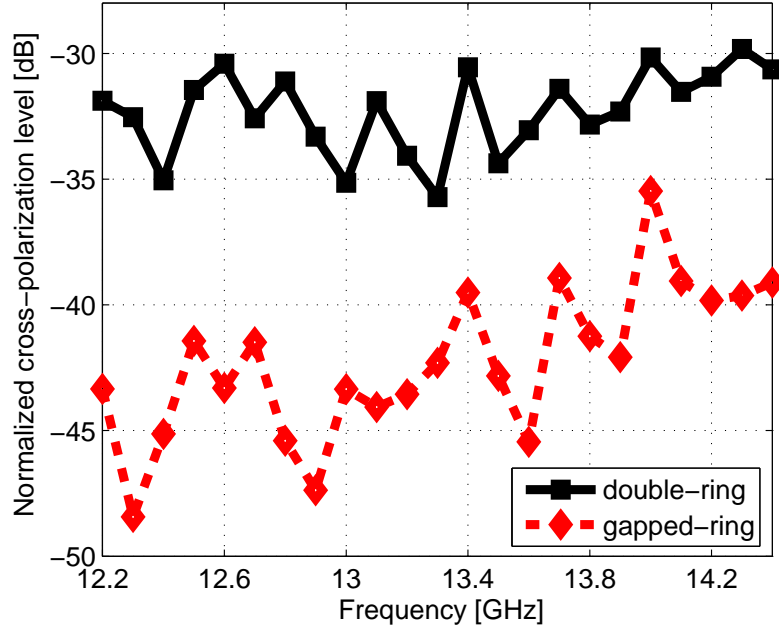


Figure 4.13: Measured normalized cross-polarization level at broadside direction (E-plane).

between of 5.3 dB at 14 GHz and 15.9 dB at 12.3 GHz. Besides the cross-polarization reduction, the measured broadband results also show performance tradeoffs of the higher SLL and slightly broadened beamwidth, which are similar to the observation in simulated results.

Two factors may cause the slight discrepancy of the cross-polarization levels between the simulated and measurement results. First, in the simulation, the feed horn is simulated separately with the array of the reflectarray, and then the obtained radiation pattern of the feed horn is added as an incident field on the reflectarray. By using the incident field instead of the physical horn as the feed source, the calculation efficiency is largely increased. However, the blockage effects from the feed horn and antenna support strut, which will affect the cross-polar level in measurements, are not included in the simulations. Second, the

cross-polarization level is also affected by the alignment condition between the antenna under test (AUT) and the source antenna in the measurements.

4.7 Conclusion

This chapter presents the investigation results of a novel reflectarray design using gapped double-ring elements for cross-polarization suppression. To suppress cross-polarization radiation, gaps are cut on the double-ring elements to change the directions of the surface currents, so the co-polar components enhance each other and the cross-polar components cancel each other, and thus a low cross-polarization level can be achieved. Even though there are some tradeoffs for the gain and SLLs, measurement results for the two reflectarray antennas show a 10 dB reduction in cross-polarization level at the broadside direction at 13.325 GHz and > 5.3 dB reduction through the frequency band from 12.2 GHz to 14.4 GHz.

Chapter 5

An X/Ku Dual-band Reflectarray Design with Cosecant Squared Shaped Beam

5.1 Introduction

A reflectarray antenna is a well-known antenna type whose history can be traced back to the 1970s; it has been used in NASAs space-borne systems [8, 76]. The multi-beam, electronic scanning of a reflectarray can be achieved with good beam pattern properties and polarimetric isolations [34, 103]. However, compared to the reflector antenna, one of the most severe drawbacks of a reflectarray is the narrower bandwidth performance. As discussed in Section 2.2, the bandwidth of reflectarray is limited by both the narrow bandwidth behavior of microstrip elements and the different spatial phase delays in a large aperture.

To overcome this problem, several broadband or multi-bands reflectarrays have been developed, one example is an X/Ka bands reflectarray developed by JPL in [104], in which the Ka-band variable rectangular patches layer were put on bottom and X-band variable crossed-dipoles above them. However, when extending single-band and single-layer reflectarray to dual-band and dual-layer reflectarray, one difficulty is the interactions between the layers cannot be predicted accurately and the effect of the interactions on array performance can only be determined empirically [104]. It also shows that the Ka-band patches

had negligible impact on X-band performance, while the X-band caused a 1.8 dB reduction in Ka-band gain [104].

Another example is a dual-layer, C/Ka dual frequency reflectarray developed in [19], in which a dual frequency, dual-layer circularly polarized reflectarray using microstrip ring elements of variable rotation angles was designed. The single-layer Ka-band and dual-layer Ka-band (with the existence of a C-band layer) were both measured and presented. An aperture efficiency loss and a higher sidelobe level were observed for the Ka-band in a dual-layer environment, comparing to the single-layer Ka-band performance which has no interference/scattering from the top layer C-band elements. Other recent designs of the dual-band reflectarray include an array-fed Ku/Ka dual-band reflectarray [20] and a single layer dual-band reflectarray using multi open loop elements [105].

The goal of this chapter is to design a shaped beam reflectarray to realize a dual-band operation at 10 GHz (X-band) and 15 GHz (Ku-band) for potential GBSAA radar applications [106]. Since the two operation frequency bands are fairly close to each other, the radiation interference between the two bands must be taken into consideration and design should be optimized to suppress the interference as much as possible. In the unit cell design, microstrip cross-dipoles and double-rings are chosen as the X-band and Ku-band elements, respectively. A dual-layer structure with cross-dipoles on the top layer and double-rings on the lower layer is adopted to suppress the interband couplings. Moreover, the dual-band elements are arranged in an interleaved manner in order to minimize element blockage: one cross-dipole element is put at the center of the unit cell on the top layer, while on the lower layer four double-ring elements are placed at the four quadrants, separated by the cross-dipole, respectively. Furthermore, the coupling effects on the reflection phase response are also investigated, and the

unit cell designs are carefully tuned in the simulations to suppress the coupling effects.

In addition, a phase-only synthesis technique is also developed to generate two cosecant squared shaped beams for each operation frequency band. One typical application of cosecant squared beam pattern is the air and coastal surveillance radars, where a fan beam with a shape proportional to the square of the cosecant of the elevation angle is achieved for the surveillance coverage. Traditionally, a cosecant squared beam pattern can be achieved by a deformation of a parabolic reflector, usually through fine tuning of the reflection surface, such as with a lower bending of the top part of the reflector. However, the design and manufacture of the reflector are fairly complicated and costly. In this chapter, a reflectarray design has been demonstrated to fulfill the required shaped beam. With a beam synthesis process, the phase distributions for the cosecant squared beams are obtained and realized through size variations of the reflectarray elements. The reflectarray can be easily manufactured with the modern PCB technology, making the antenna low-profile and low-cost.

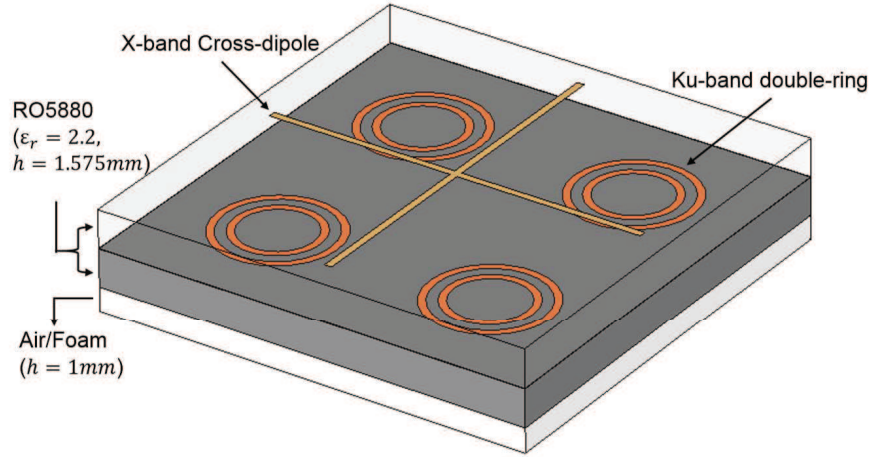
This chapter starts with cross-dipole and double-ring element designs, which are arranged in an interleaved manner to minimize the blockage of the incident waves. Then the coupling effects of the elements between the two close operational bands are investigated. The phase-only synthesis method to generate the desired shaped beams and the implementation into an array design are also discussed. Finally, the measured reflectarray performances are discussed and compared with simulated results.

5.2 Unit Cell Design

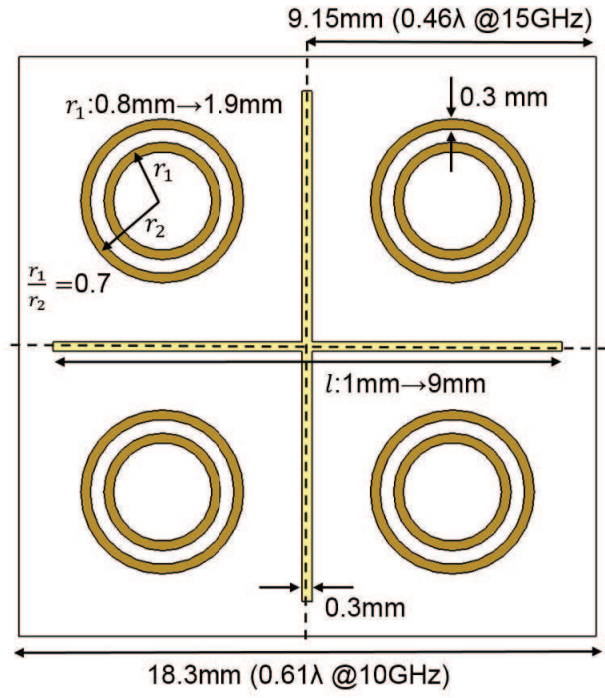
The reflectarray unit cell is shown in Figure 5.1 (a) with its dimensions shown in Figure 5.1 (b). The reflectarray unit cell has a dual-layer configuration with the X-band layer on top of the Ku-band layer to support dual-frequency operation. The reflectarray unit cell consists of two different types of elements. Double-ring elements are used for the Ku-band to achieve a wider range of reflection phase variation. Since a double resonant response can be obtained from the concentric rings, a much larger phase range will be generated than that of a single-ring element. The cross-dipole elements are used on the top layer of the unit cell for the X-band, because they use less metallization than patch elements and can be seen as transparent to the bottom layer elements at the Ku-band. Thus, this allows more incident energy to pass between the layers.

Moreover, to further reduce the elements blockage from the top layer, as shown in Figure 5.1, the X-band cross-dipole is placed at the center of the unit cell on the top layer, while on the second layer four Ku-band double-ring elements are put on the four quadrants separated by the cross-dipole, respectively. This so-called interleaved element arrangement between the layers can help minimize the blockage of the incident wave and reduce the element interaction between the two frequency bands as well.

The X-band element is designed at a center frequency of 10 GHz, while the operation frequency of the Ku-band element is 15 GHz. As shown in Figure 5.1 (b), the X-band cross-dipole has a size of 18.3 mm, which is about 0.61λ at 10 GHz. The Ku-band double-ring has a size of 9.15 mm, corresponding to a 0.46λ at 15 GHz. The length l of the cross-dipole elements and the inner ring radius r_1 of the double-ring elements are adjusted to obtain the reflection phases,



(a)



(b)

Figure 5.1: Schematic and geometry of the dual-band reflectarray unit cell.

Table 5.1: Dimensions and parameters of the X-band and Ka-band unit cell design

Parameter	Definition	Value
f_X	X-band operation frequency	10 GHz
l_X	X-band unit cell dimension	18.3 mm
l	X-band cross-dipole length	1 mm \rightarrow 9 mm
w_X	X-band cross-dipole width	0.3 mm
ε_r	Relative permittivity of the substrate	2.2
ε_2	Relative permittivity of the air/foam layer	1.03
h_1	Height of the RO5880 substrate	1.575 mm
h_2	Height of the air/foam layer	1 mm
f_{Ku}	Ku-band operation frequency	15 GHz
l_{Ku}	Ku-band unit cell dimension	9.15 mm
r_1	Double-ring inner ring radius	0.8 mm \rightarrow 1.9 mm
r_1/r_2	Inner and outer ring radius ratio	0.7
w_{Ku}	Ku-band double-ring width	0.3 mm

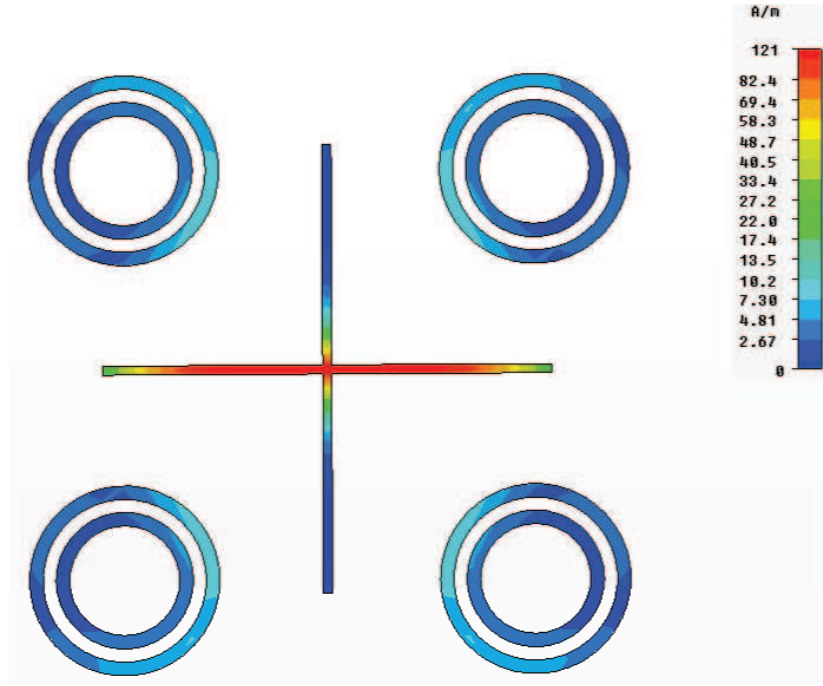
respectively. Ring width and cross-dipole width are both 0.3 mm. A ring radius ratio $r_1/r_2 = 0.7$ is adopted for the double-ring elements because our simulations showed it has a better linearity of phase variation and also a broader phase range over other ratios. The substrate used for both layers was RO5880 with $\varepsilon_r = 2.2$ and 1.575 mm in thickness. The dual-layer is placed 1 mm above the ground with the aid of foam in order to enhance the linearity of the phase variation curves. The dimensions of the dual-band unit cell are summarized in Table 5.1.

5.3 Coupling Effects

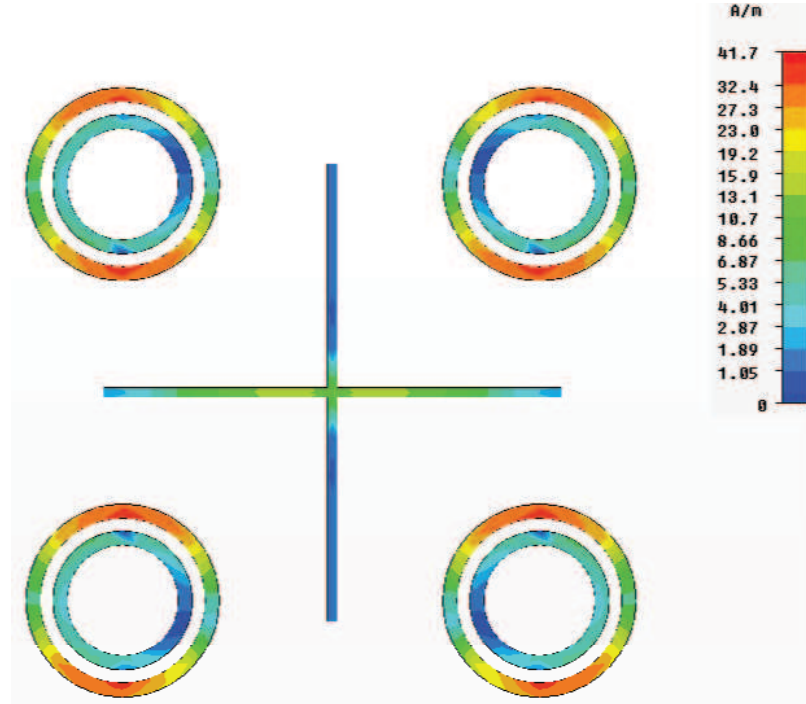
The element configurations for dual-frequency operation has been introduced in the previous section. In order design a fully functional reflectarray with dual-band operation, especially for two close frequencies as in the presented design, it is necessary to examine the coupling effects between the two bands. Since the two types of elements are assembled together, their coupling effects will change the performance of the antenna. Besides the aforementioned interleaved element arrangement between the two layers, the EM coupling effects are also investigated in the simulations, including the surface currents and reflection phase variations.

First, the surface currents of the dual-band unit cell in Figure 5.1 (a) were simulated at 10 GHz and 15 GHz, respectively. The simulations were carried out in CST Microwave Studio® [77]. The simulated surface current densities of the dual-band dual-layer unit cell at different frequencies are depicted in Figure 5.2. From Figure 5.2 (a) it can be clearly observed that, the currents are concentrated on the cross-dipole on the top layer at the X-band (10 GHz), while at the Ku-band (15 GHz) the currents flow dominantly on the double-ring elements, as shown in Figure 5.2 (b). In fact, the reflection field are radiated from the surface currents on the patches array and most of the radiation power should be coupled to the currents on them. Therefore, both cross-dipole elements and double-ring elements can generate a dominant surface current at their respective operation frequencies, indicating a possibly low coupling effects.

In order to further study the interference between the dual frequency bands, the reflection phase responses of the dual-band elements were also examined. Two cases were considered for each frequency band: (1) single band elements alone, and (2) two band elements together. First, for the case of X-band cross-dipole



(a)



(b)

Figure 5.2: The surface current density on the dual-band reflectarray unit cell, (a) at 10 GHz and (b) at 15 GHz.

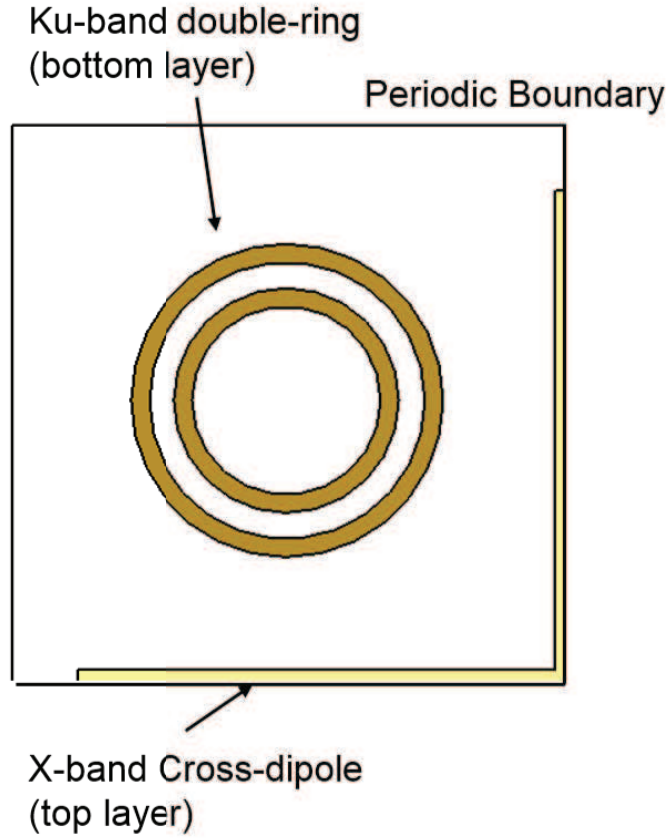


Figure 5.3: The unit cell of the Ku-band double ring are simulated at 15 GHz with presence of X-band cross-dipole.

with presence of the Ku-band double rings, the unit cell in Figure 5.1 (a) were used in the simulation, in which the periodic boundaries were applied to emulate the unit cell in an array environment. Second, for the Ku-band double ring with presence of the X-band cross-dipole, the unit cell shown in Figure 5.3 was used in the simulation, due to the fact that only half part of the X-band cross-dipole are presented for a single double ring unit cell.

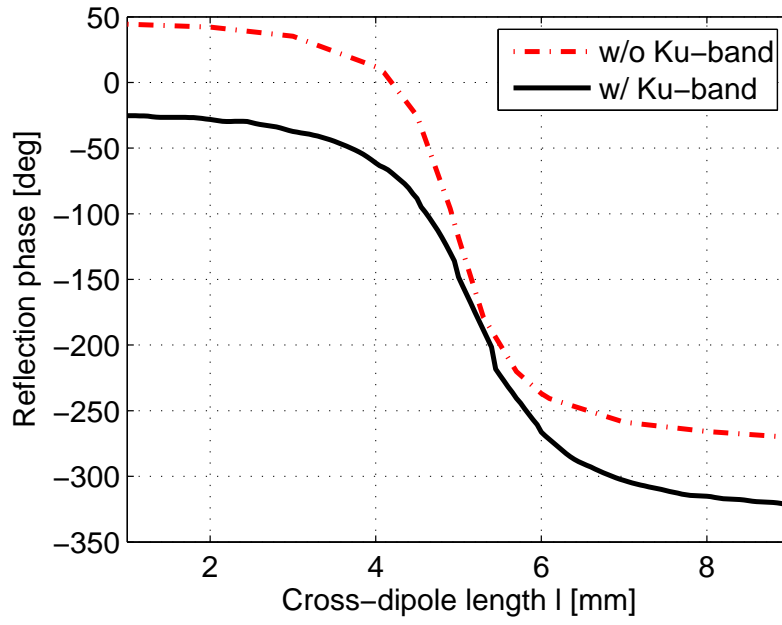
Figure 5.4 shows the simulated phase responses for those scenarios. We can clearly see the change of the phase variations, due to the induced parasitic effects from the preset elements of different bands.

First, for the Ku-band double ring, with the X-band cross-dipole on the top layer, the reflection phases become larger than that without the cross-dipole, where the maximum phase difference is about 20° .

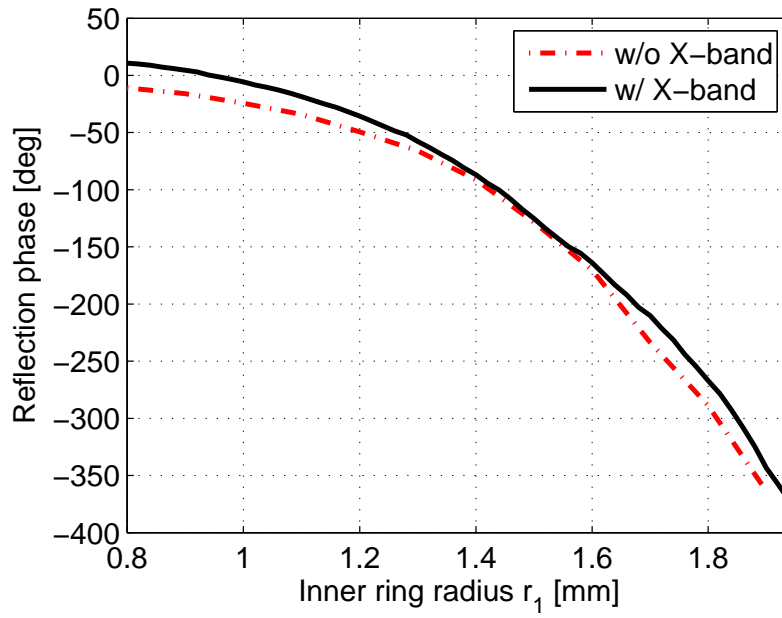
Second, for the X-band cross-dipole, the reflection phase difference between with Ku-band layer and without Ku-band layer can be as large as around 80° . Since the phase responses of elements in a single band are prone to shifts when combining with elements from another frequency band, it becomes necessary to include the elements of another band into the unit cell simulation when characterizing the phase variations.

To calculate the reflection phase of the elements of one frequency band (referred to as main frequency) with the presence of another frequency band element (referred to as coupling frequency), the dimension of the elements of the main frequency will be varied and the dimension of the elements of coupling frequency needs to be fixed. To find an optimal pre-configured size for the coupling elements in the unit cell, different dimensions are tested in the simulations.

Figure 5.5 shows the reflection phase curves with several dimension changes on the coupling elements. In Figure 5.5, different cross-dipole lengths from 4 mm to 7 mm are tested in the Ku-band unit cell simulations. We can see that the varied dimensions of the coupling elements have little impact on the reflection phases of the elements of main frequency. Thus for simulation efficiency, it may be safe to fix the dimension of the coupling elements while only varying the dimensions of the element of the operational band. In our simulations, to obtain the reflection phase curves, the inner radius of the double-ring is set to 1.7 mm for the X-band simulations, while the length of the cross-dipole is set to 5.5 mm for the Ku-band simulations.



(a)



(b)

Figure 5.4: Simulated reflection phases of the (a) X-band cross-dipole element at 10 GHz and (b) Ku-band double-ring element at 15 GHz.

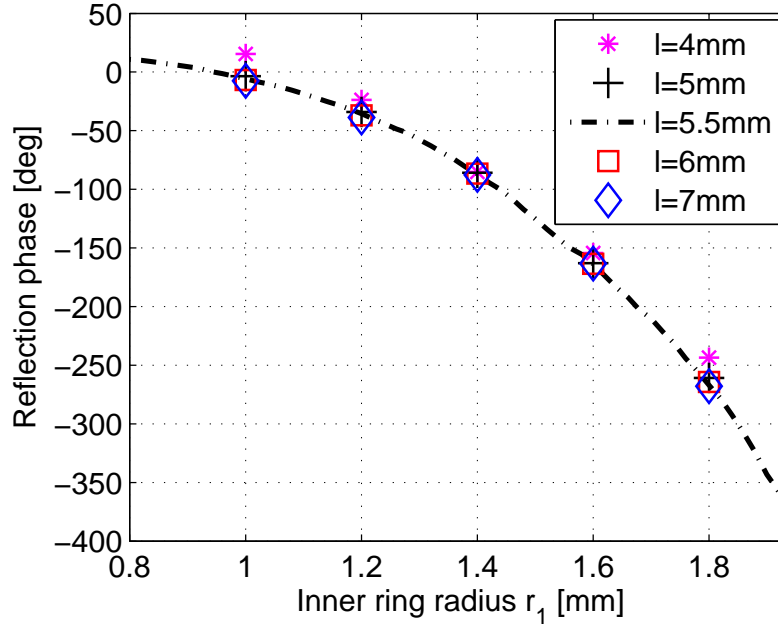


Figure 5.5: With presence of X-band cross-dipole of different dipole lengths, the reflection phases of the Ku-band double ring are simulated at 15 GHz.

5.4 Beam Synthesis

5.4.1 Phase-Only Synthesis of Reflectarray

As discussed in Chapter 1, a reflectarray is an array of non-interconnected radiating elements, and the desired radiated field of the reflectarray comes from the reflection of the field emitted by a feed on the array elements which has proper phases to form the desired wave front. Hence, the synthesis of radiation patterns from reflectarrays can be reduced to a phase-only control problem: an excitation correction mechanism is required to compensate the different path delays between every element and the feed in order to achieve the desired radiation pattern, while the amplitude of each element is fixed in accordance with the feeding element and the geometry of the antenna.

In the case of linear arrays, different simple methods have been developed to find the phase excitation when the amplitude is fixed [107, 108], although its extension to a planar array with increased number of elements becomes more difficult. Concerning the synthesis of reflectarray with pencil beams, several contributions have been carried out [109, 110]. In [109], the method of approximation programming (MAP) is used to determine the optimum excitation phases which minimize the sidelobe level for a 32-element, uniformly excited double-ring circular array. On the other hand, in [110], a numerical search procedure to minimize the expression for the pattern sidelobe level with respect to the element phases is applied to both linear and circular arrays with rectangular grid and uniform excitations. Also in [110], a more powerful analytical synthesis algorithm is presented for use on very large arrays since the numerical search technique for the minimization of the sidelobe level is computationally impractical. This algorithm was applied to very large circular arrays with more than 10,000 elements.

With regard to contoured-beam patterns in reflectarray, some simple analytical techniques have been developed. In [111], a phase-only method for the synthesis of aperture phase distribution for apertures with arbitrary shape and amplitude distribution is reported. The phase distribution is determined by modeling the aperture as a combination of parallel strips with specific linear-phase distributions. Also in [112], a biquadratic programming method is formulated with variable-phase and constant amplitude distributions. This method is restrictive since it requires the optimization function to be expressed as a ratio of Hermitian quadratic forms, although it shows more rapid convergence characteristics than prior-art methods.

Several numerical techniques of phase-only synthesis have been successfully applied to large reflectarrays with shaped-beams. Some are based on the iterative

optimization of a functional defined as a cost function by perturbations of zeros of a pre-fixed pattern [113], or by adjusting two phases per iteration through a bi-coordinated method [114]. Also, by slightly changing the excitation phases in a linear approximation, which can be determined by the least-squares method, the excitation phases can be obtained after iterations [115]. An alternative for reducing the number of optimization variables was proposed in [116], where only a small representative set of beam directions of the coverage patterns is taken into account as the minimax goal. This method is particularly appropriate for the synthesis of coverage patterns for satellite communications, where the beam directions are desired at a set of service locations [116]. Furthermore, the synthesis problem is formulated as an intersections finding problem, where the actual radiating properties of the antenna and the performance required by the antenna are seen as a system [117]. Different applications of the intersections finding approach have been provided in [118–120].

A shaped beam reflectarray for DBS applications has already been manufactured [121]. The phase synthesis is obtained from the previously designed shaped-reflector that produces the desired beam shape, which is generated through a commercial reflector design software. Then, ray tracing can be used to determine the necessary reflection phases of the reflectarray elements to duplicate the same radiating aperture phase distribution as was synthesized for the shaped-reflector antenna. In this way, a progressive phase shift is generated in addition to the phase required to shape the main beam and no additional phase shift is needed to scan the beam in the desired direction. Nevertheless, a reliable and efficient synthesis method with no dependence on reflectors is desirable.

5.4.2 An Analytical Technique for Cosecant Squared Beam Shaping

In this section the reflection phases of reflectarray elements are synthesized in order to fulfill the desired squared cosecant beam pattern in elevation. An analytical phase-only synthesis technique described in [122,123] is applied to obtain the linear phase distributions for the elevation shaped beam. For an array with a length of $2L$ and a wavelength of λ , the derivative of phase distribution is given by [122]

$$\phi'(x) = \frac{2\pi L}{\lambda} \frac{1}{\frac{1}{u_0} + \left[\frac{1}{u_1} - \frac{1}{u_0}\right] \frac{\int_{-1}^x A^2(x)dx}{\int_{-1}^1 A^2(x)dx}} \quad (5.1)$$

where $A(x)$ is the amplitude distribution, and u_0, u_1 are used to define the cosecant squared shape. The phase function $\phi(x)$ required for any amplitude distribution $A(x)$ can be obtained from a numerical solution of the differential equation 5.1. With $u = \sin\theta$, the pattern function can be found by

$$E(u) = \int_{-1}^1 A(x) e^{j\left(\frac{2\pi L}{\lambda} ux - \phi(x)\right)} dx \quad (5.2)$$

To realize a shaped beam, a circular reflector surface with a diameter $D = 305$ mm is defined. The double-layer array has 15×15 cross-dipole elements operating at 10 GHz on the top layer and 32×32 double-ring elements operating at 15 GHz on the lower layer. First, the linear phase distribution for the desired shaped beam was calculated. With a pre-defined $u_0=0.05$ for X-band squared cosecant beam and $u_0=0.15$ for Ku-band cosecant squared beam, the linear phase distributions $\phi(x)/(2\pi L/\lambda)$ and synthesized pattern $E(u)$ were calculated using equations 5.1

and 5.2 for the linear arrays, including a 15×1 array at 10 GHz and a 32×1 array at 15 GHz, are shown in Figure 5.6 and Figure 5.7, respectively.

After obtaining the linear phase distribution of a shaped beam, the array phase distribution over the reflectarray surface to produce a collimated beam at broadside direction are computed by applying the following formula:

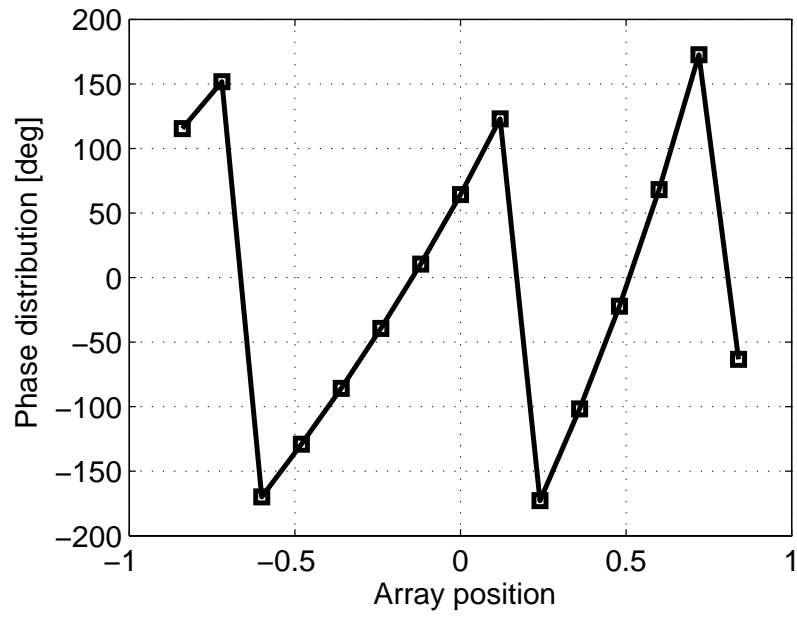
$$\Phi_{m,n} = k_0(d - (x \cos \phi_b + y \sin \phi_b) \sin \theta_b) \quad (5.3)$$

where (x, y) are the coordinates of the element $_{m,n}$, and d is the distance from the center of element $_{m,n}$ to the central point of the feed aperture. The desired beam direction is defined by ϕ_b and θ_b , which are the spherical coordinates with origins at the center of the array. Here we are interested in the surface phase distribution for broadside radiation, so $\phi_b = \theta_b = 0^\circ$.

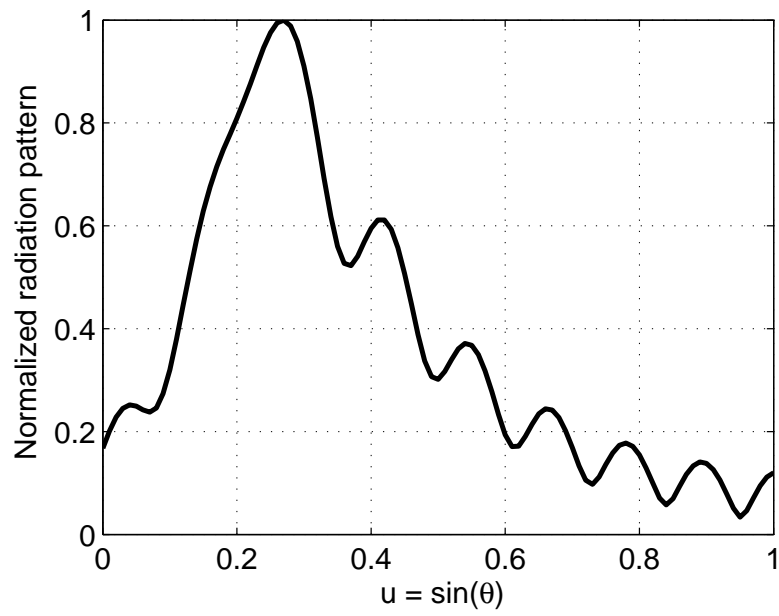
5.5 Array Design and Simulation

Once the linear phase distribution for the shaped beam and the surface phase distribution of the circular array for a broadside beam have been determined, the actual reflectarray phase distribution to shape a squared cosecant beam can be obtained by adding the linear phase distribution onto each row of the array phase distribution. Figure 5.8 shows the required phase distributions on the circular reflectarray with a center-fed horn to generate two squared cosecant beams at 10 GHz and 15 GHz, respectively. The feed position (focal length f) is optimized as $f/D=1.5$ for the selected horn antenna considering both aperture efficiency and antenna setup size.

After the reflection phase required at each reflectarray element has been determined, the dimensions of each element on both layers have to be adjusted

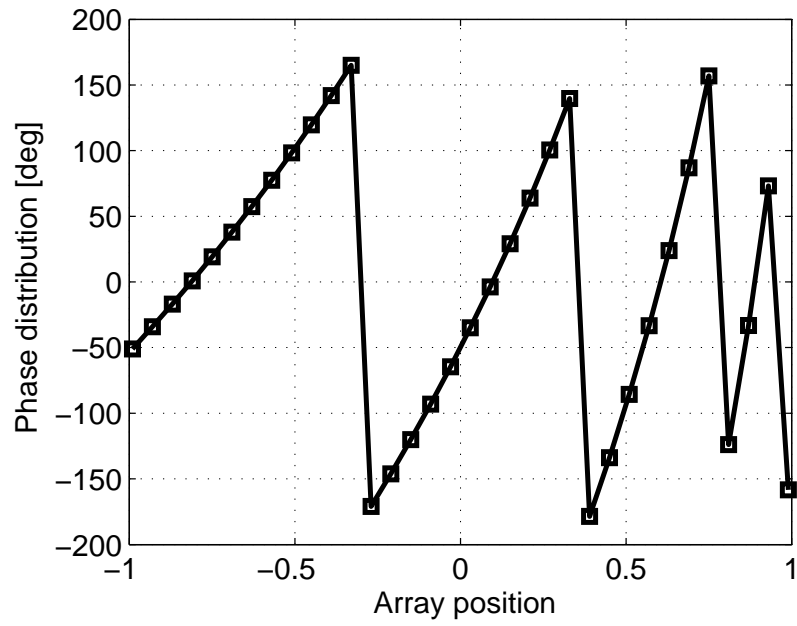


(a)

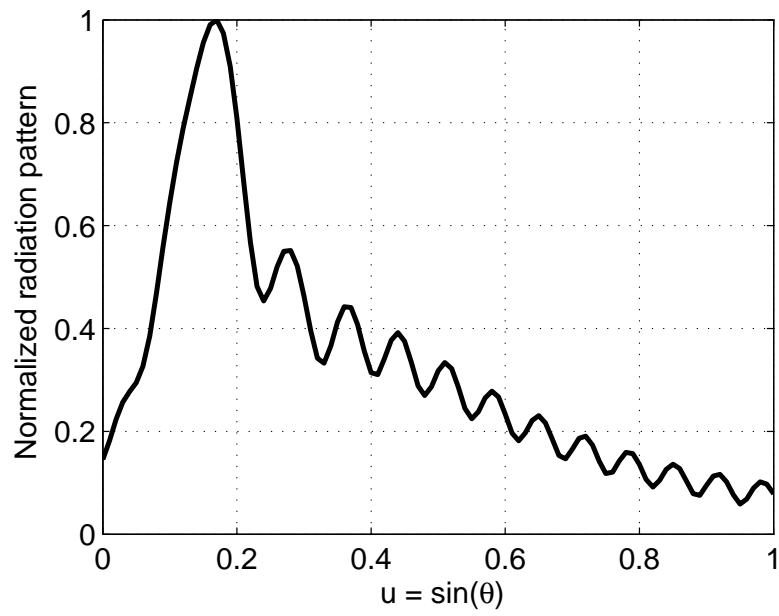


(b)

Figure 5.6: Synthesized phase distribution and pattern for the X-band 15x1 linear array.

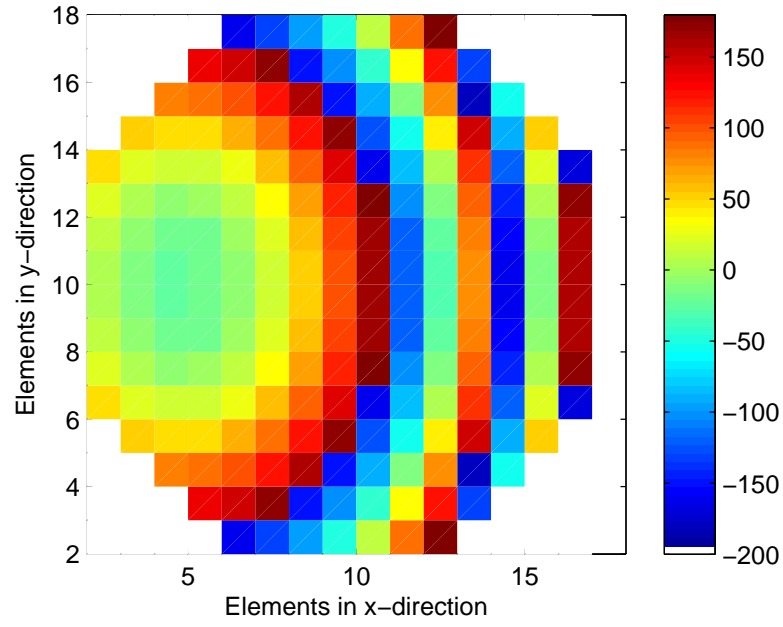


(a)

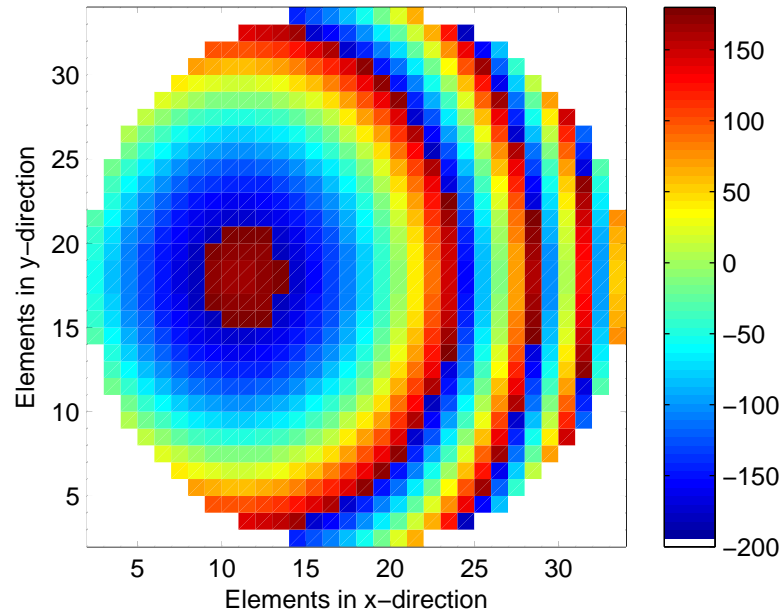


(b)

Figure 5.7: Synthesized phase distribution and pattern for the Ku-band 32×1 linear array.



(a)



(b)

Figure 5.8: Required phase distributions on the dual-layer reflectarray to generate the desired cosecant squared shaped beam for (a) X-band cross-dipole array (b) Ku-band double-ring array.

accordingly based on the phase-size relation. The top view of the dual-layer reflectarray modeled in CST is shown in Figure 5.9, in which the top substrate layer is set to transparent in order to show the array topology on both layers.

Full-wave electromagnetic simulations on this dual-layer reflectarray at both 10 GHz and 15 GHz are carried out by using the Integral Equation Solver in CST. The radiation pattern of the feed horn is first calculated, from which the incident field on the reflectarray is found by using the far field source in the solver. Note that both the top layer array and the lower layer array are included in the simulation at 10 GHz and 15 GHz, since in section 5.3 the unit cell design has been optimized based on the dual-layer configuration considering the coupling effects suppression.

The simulated results of the dual-layer reflectarray are shown in Figure 5.10. We can see that the reflectarray can generate a better cosecant squared shaped beam at Ku-band because for the same aperture size the Ku-band array has 812 elements whereas the X-band array only has 185 elements. Figure 5.11 shows the simulated 3D pattern of the shaped beam, in which we can clearly see the synthesized cosecant squared beam shape in X - Z plane.

5.6 Array Measurements

5.6.1 X-Band Measurement Results for the Dual-Layer Reflectarray

The measurement results of the fabricated dual-layer reflectarray antenna are discussed in this section. A 0.31-m diameter X-band reflectarray is fabricated on the top layer using 185 cross-dipole elements. Then 812 double-ring elements

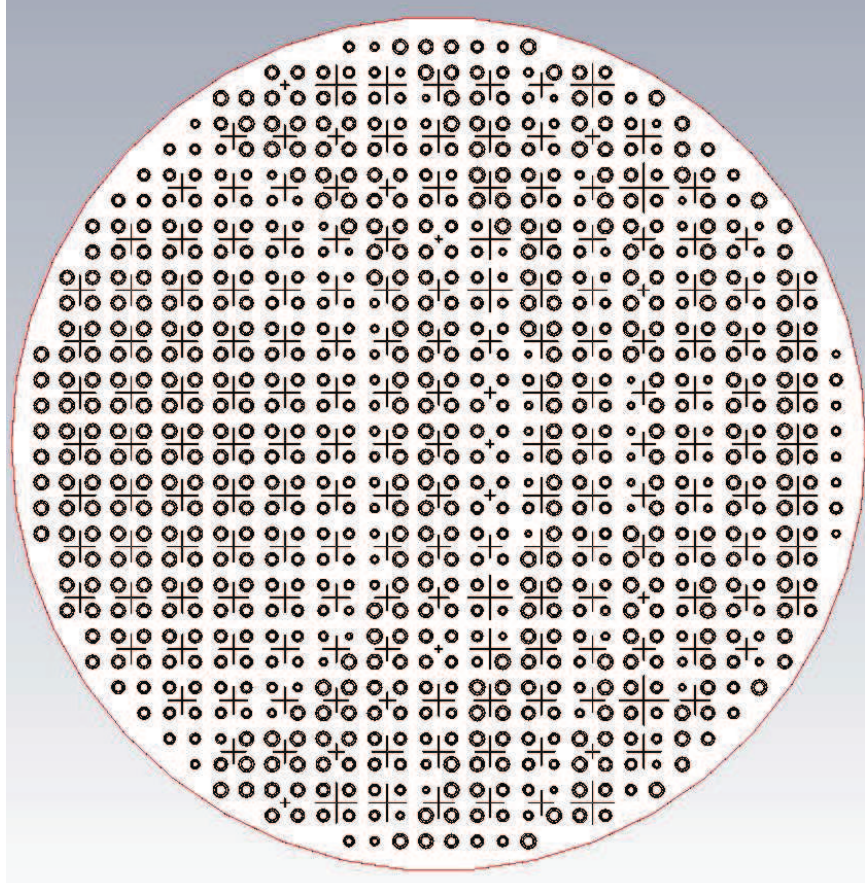
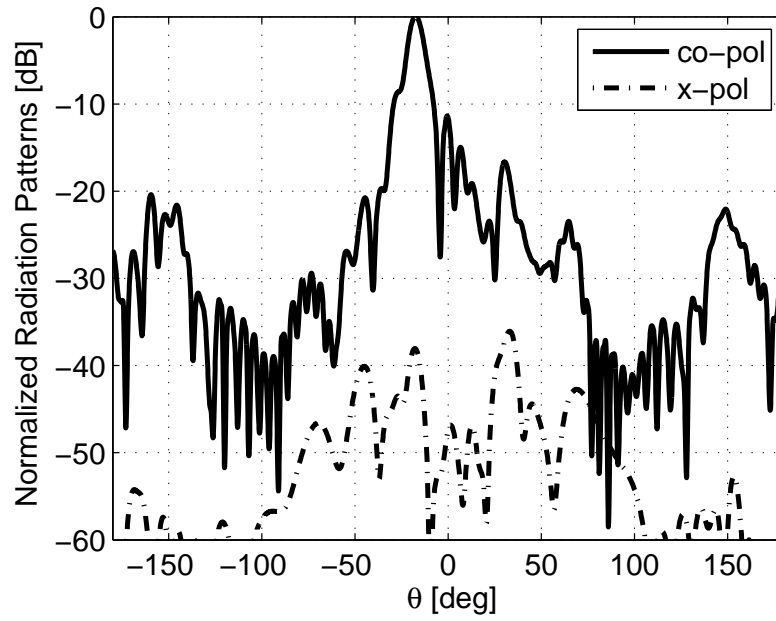


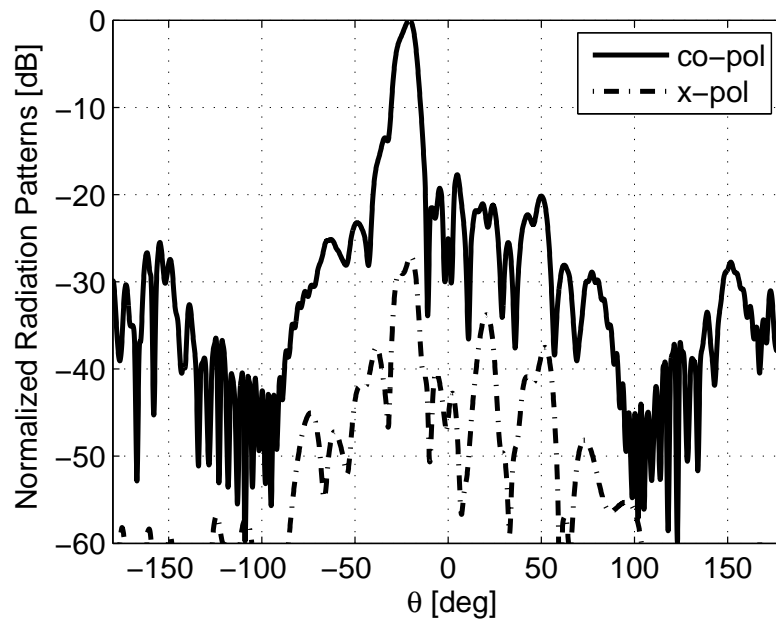
Figure 5.9: Dual-layer reflectarray topology.

operating at Ku-band are fabricated on the lower layer substrate over a 1 mm-thick air gap backed by a ground conductor. The breakdowns of each layer of the prototype reflectarray are presented in Figure 5.12. A linearly polarized standard horn is used as the feed antenna. The feed horn is mounted at 458 mm ($f/D = 1.5$) above the reflectarray through a support arm structure.

The measurements were performed in the anechoic chamber at the University of Oklahoma. During the tests the reflectarray was mounted on a positioning system consisting of an azimuth rotary stage. A linearly polarized standard horn was used as the transmit antenna. Figure 5.13 (a) shows the measured E-plane



(a)



(b)

Figure 5.10: Simulated radiation patterns of the dual-layer reflectarray at (a) X-band and (b) Ku-band.

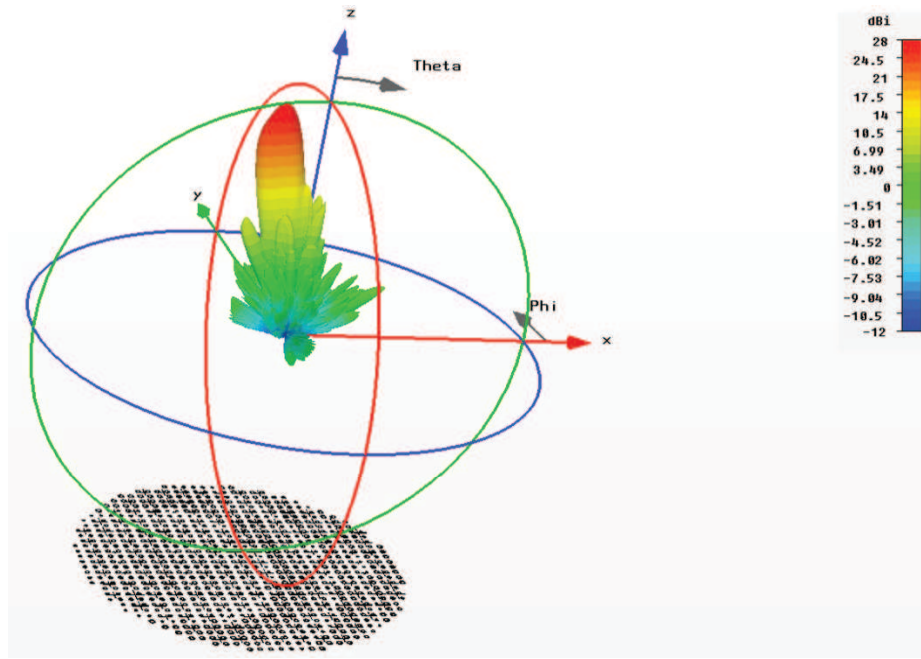


Figure 5.11: Simulated 3D cosecant squared shaped beam of the dual-layer reflectarray at Ku-band.

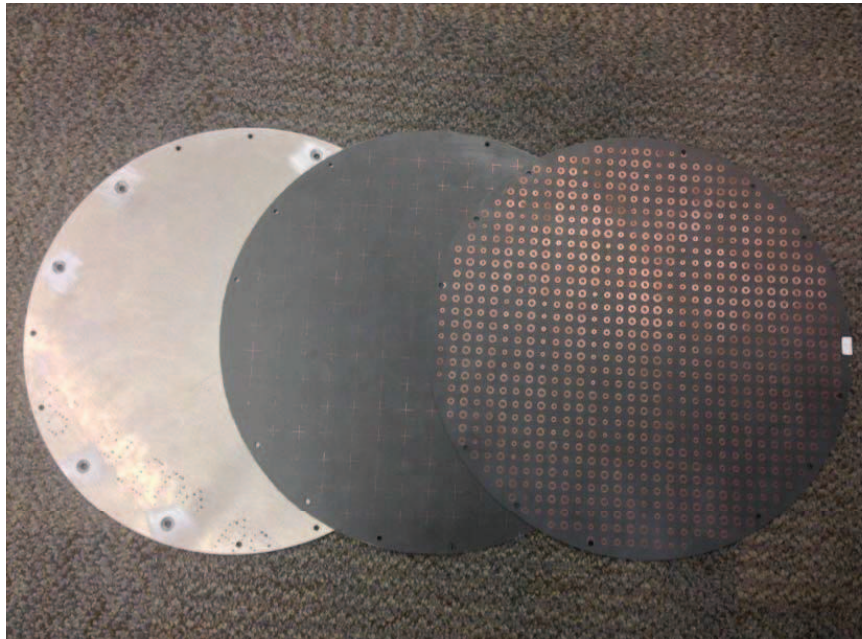


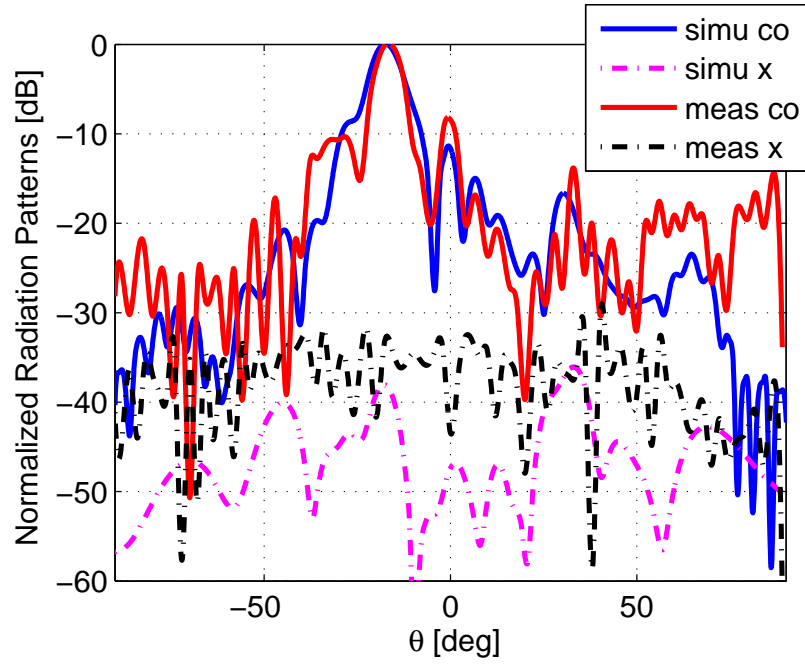
Figure 5.12: Photograph of the dual-layer prototype reflectarray.

far-field radiation patterns at 10 GHz, which is also compared with the simulated results. A good agreement between the measurement and simulation results can be observed, except for a higher side lobe level, which may be caused by the blockage of the mounting strut of the feed horn. In the simulation we directly used the calculated radiation pattern of the feed horn as the source, instead of including the feed horn and the associated support strut in the simulation. This simulation method can largely improve the simulation efficiency and enable the simulation of the complete reflectarray structure with standard PC resources, while with a tradeoff on the prediction of the side lobe levels and the cross-pol levels [85].

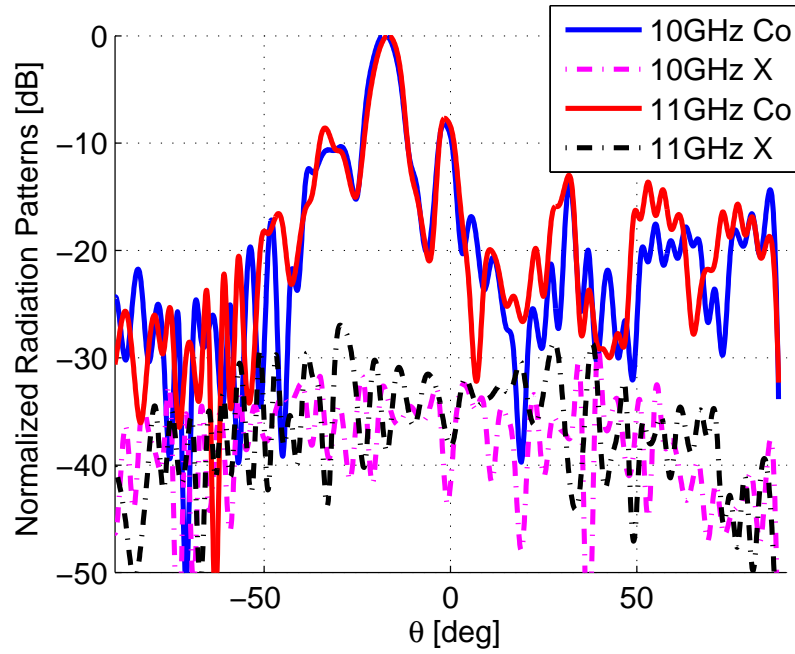
The far-field radiation pattern of the reflectarray is also measured across a frequency band from 10 GHz to 11 GHz. Figure 5.13 (b) shows the measured radiation patterns at different frequencies. At 10 GHz and 11 GHz similar radiation patterns are observed, except for a slight increase in side lobe levels as frequency increases.

5.6.2 Ku-Band Measurement Results for the Dual-Layer Reflectarray

The measured results at Ku-band are shown in Figure 5.14. Figure 5.14 (a) plots the measurement results at 15 GHz, compared to the simulated patterns. At 15 GHz the main beam is at $\theta = 20^\circ$ away from broadside and has a width of 9.7° . The side lobe level is about -14 dB and the cross-polarization level is -45 dB, down from a peak at $\theta = 20^\circ$. This indicates a low interband element coupling due to the carefully optimized element design between the dual-layers. As can be seen in the figure, the measured and simulated results at 15 GHz are

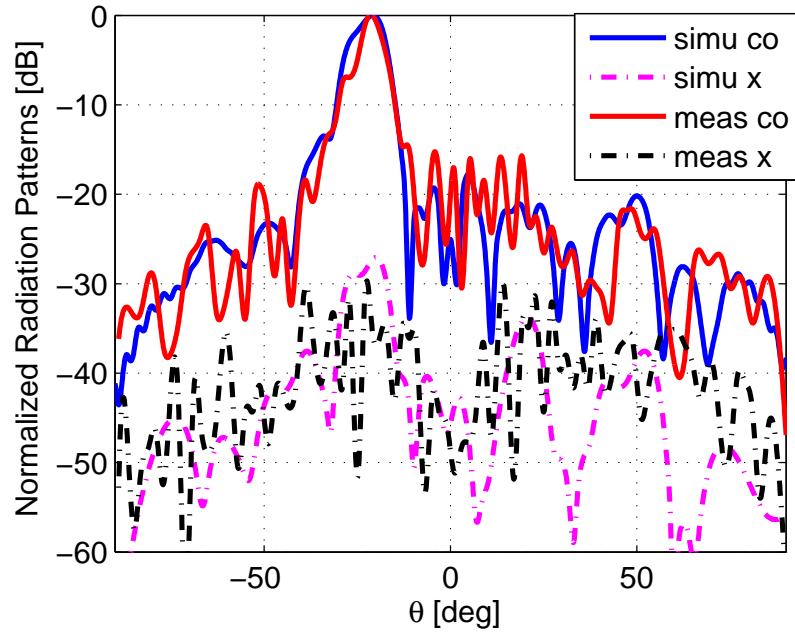


(a)

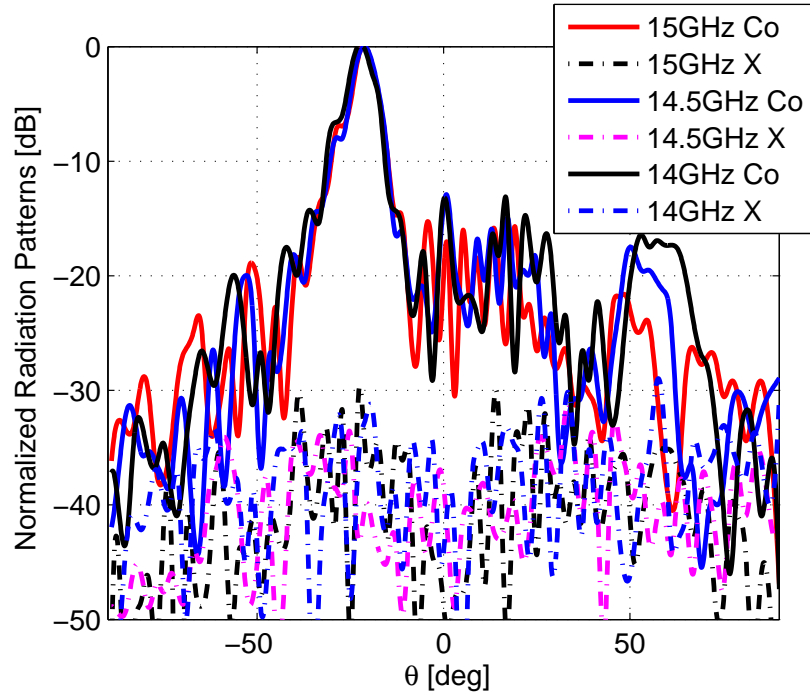


(b)

Figure 5.13: Measured radiation patterns at X-band for the dual-layer reflectarray, (a) at 10 GHz and (b) wide band performance.



(a)



(b)

Figure 5.14: Measured radiation patterns at Ku-band for the dual-layer reflectarray, (a) at 15 GHz and (b) wide band performance.

in fairly good agreement, especially concerning the positions and widths of the main lobes, while the slightly higher side lobe can be attributed to the effects of the supporting structures of the antenna in the anechoic chamber. Figure 5.14 (b) shows the broadband radiation patterns measured at 14 GHz and 14.5 GHz, compared to the beam pattern at center frequency of 15 GHz. The reflectarray maintains similar radiation patterns over the frequency ranges from 14 to 15 GHz.

5.7 Conclusion

In this chapter, a dual-layer dual-frequency reflectarray antenna with cosecant squared shaped beams is presented. The two operation frequencies, 10 GHz and 15 GHz are in a close frequency range. To suppress the interband coupling of the dual-band elements, cross-dipole and double-ring elements are designed and optimized for both operating frequencies. The phase-only beam synthesis technique for the cosecant squared beams is also discussed. The reflectarray antenna has been manufactured and tested, and the measured radiation patterns are in good agreement with theoretical expectations and simulation results. These results demonstrate the capability of reflectarrays to generate simultaneous shaped beams at two close frequency bands.

Chapter 6

Conclusions

6.1 Summary

This dissertation covers the design concepts of a single-layer broadband reflectarray and a dual-band reflectarray with cosecant squared shaped beams, techniques to predict and mitigate the blockage effect in reflectarray, as well as the methods to suppress cross-polarization level in reflectarray designs.

In Chapter 2, a single-layer, low cost broadband reflectarray has been developed. The reflectarray uses two types of elements, microstrip ring and microstrip patch with ring boundary, to increase the reflection phase variation range. In the proposed element configurations, the inner radius of the ring and the radius of the circular patch are changed respectively to generate the phase curve. It shows that the variable-sized ring generates a phase range from -132° to 188° and the variable-sized ring-patch element covers a phase range from 188° to 230° . The combination of these two element configurations can provide at least 360° phase range, which supports a broadband operation of the reflectarray. Furthermore, the phases are approximately a linear function of size of the elements for both configurations, which is important to reduce the manufacturing errors.

In reflectarray, the center feed blockage and multi-reflection effect mainly contribute to the increased side lobe levels. To accurately predict the performance of the reflectarray with a center-fed horn, the blockage from the feed horn and the support structure need to be taken into account carefully. In Chapter 3, the

blockage effect is investigated and a reflectarray with a tilted beam is proposed to mitigate the blockage from the center-fed horn. Several modeling methods are introduced, such as (i) re-radiating the reflectarray pattern on the passive feed horn, (ii) removing the elements at the shadow area on the reflectarray surface, and (iii) regarding the feed as a smooth plane of conducting metal with the radiation pattern of the feed added in front of this metal sheet as the far-field source. Comparisons among these methods are presented in terms of modeling the blockage effects, accuracies, and efficiencies. The method (i) consumes the least computational resources (i.e., time and memory) and provides a rough prediction of the radiation properties. The method (iii) generates the most accurate prediction while using relatively more computational resources.

To mitigate the blockage effects from the center-fed horn, another reflectarray antenna is designed with a tilted beam of 18° . This reflectarray adopts the same array size and focal length as the broadside reflectarray. It is observed that the measurement results are in good agreement with the simulations. The blockage effect from the center-fed horn is avoided, and the performance of the reflectarray can be predicted accurately and efficiently using the method (i). The reflectarray also shows a good wideband performance from 12.5 GHz to 14 GHz.

Low cross-polarization, which is a desired characteristic of dual-polarization weather observation, is discussed in Chapter 4. An effective method for cross-polarization suppression in reflectarray using the gapped double-ring elements is proposed. With the gapped double-ring design, the surface currents on the inner ring and outer ring will be enhanced at the co-polarization radiation direction and also cancel each other at cross-polarization radiation, so the cross-polarization level is suppressed. Measurement results of the new design show 10 dB reduction in cross-polarization level at the broadside direction at 13.325 GHz

by cutting gaps on the double-ring elements. The measured cross-polarization level of this new design is about -44 dB at broadside and less than -33 dB in all other directions.

Finally, a dual-layer dual-frequency reflectarray antenna with cosecant squared shaped beams is developed in Chapter 5. The two operation frequencies are in a close frequency range, 10 GHz and 15GHz, respectively. To suppress the inter-band coupling of the dual-band elements, cross-dipole and double-ring elements were designed and optimized coherently for both operating frequencies. An X-band cross-dipole is placed at the center of the unit cell on the top layer, while on the second layer four Ku-band double-ring elements are put on the four quadrants separated by the cross-dipole, respectively. This so-called interleaved element arrangement between the layers can help minimize the blockage of the incident wave and reduce the element interaction between the two frequency bands as well. The phase-only beam synthesis technique for the squared cosecant beams was also discussed. The measurement results demonstrate the capability of reflectarrays to generate simultaneous shaped beams at two very close frequency bands.

6.2 Recommendations for Future Research

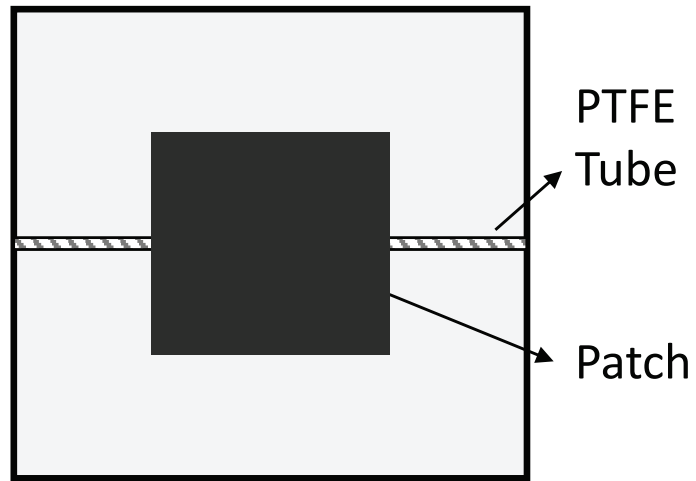
Reconfigurability of reflectarray is becoming more and more important for many applications, and research in beam scanning reflectarray is very active. Traditionally, scannable reflectarrays have been designed by incorporating electronically tunable elements into the unit cells of the periodic structures. Examples of this include embedding varactor diodes and RF MEMS switches in traditional reflectarrays. By changing the state of these varactors and switches, the phase

response of a reflectarray element can be electronically tuned. While electronic tuning has many benefits, they suffer from several disadvantages, especially the limited range of the phase responses, complicated design and high cost, especially for applications where large antennas are required. Further research are needed to develop simple, low cost and precise beam steering reconfigurable cells.

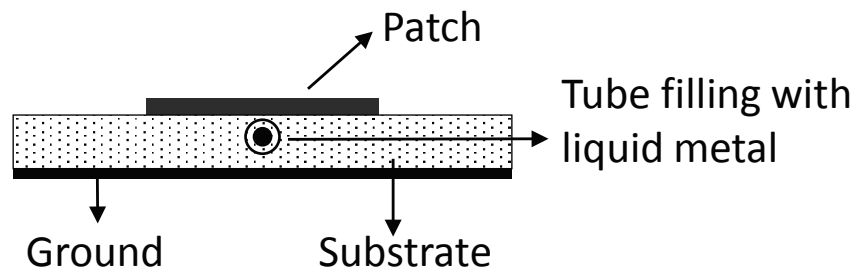
A liquid-tunable unit cell, suitable for reconfigurable reflectarrays, is recommended to achieve wider bandwidth and phase range. This technique is based on introducing capillary tubes filled with liquid metal slugs into the topology of the reflectarray. By moving the liquid metal slugs within the capillary tubes, the phase response can be tuned. The unit cell can be designed and the simulation of the liquid-tunable unit cell may be performed in HFSS.

The proposed reconfigurable reflectarray unit cell design is shown in Figure 6.1. A tube is inserted into the substrate of the unit cell, which consists of volumes of liquid metal and a carrier fluid. First, the liquid metal needs to be chosen appropriately. Generally, safety and easy operation should be the selection criteria. In [37], in a FSS design the eutectic gallium-indium-tin alloy as the liquid metal. However, it is indicated by Lei [38] that the gallium-based liquid metals rapidly oxidize when exposed to air, creating a gallium oxide skin on the surface of the bulk liquid, and making them undesirable for large arrays in an oxygen environment. Mercury (Hg) can be selected as the liquid metal. Unlike gallium alloys, mercury does not form an oxide skin, and thus remains as a true liquid during actuation [38].

Polytetrafluoroethylene (PTFE) tubing can be used to fill the liquid metal and the carrier fluid. PTFE tube has a nonwetting surface which allows mercury to readily flow through the tubing without leaving residues [38]. Mineral oil can be chosen as the carrier fluid to separate the mercury droplets. Another possible



(a)



(b)

Figure 6.1: Proposed reflectarray unit cell design using liquid-tunable technology
(a) top view and (b) side view.

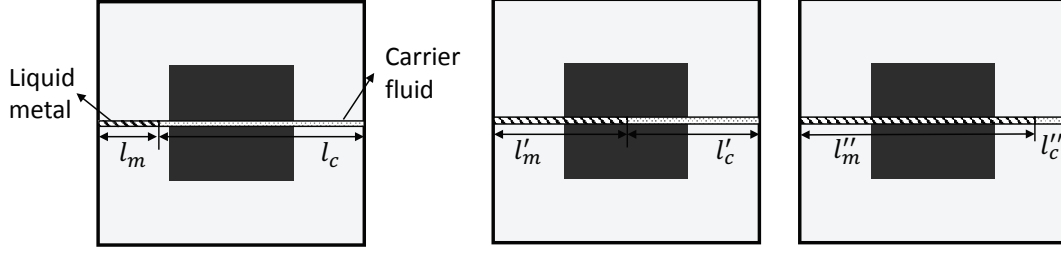


Figure 6.2: The tube is filled with liquid metal slug to change the effective capacitance of the unit cell.

option is to use the air to separate the mercury droplets in the PTFE tube, by using a needle tubing or micro pump to control the moving of the mercury slug [124].

The PTFE tube is embedded in the substrate. In the tube, the liquid mercury, having a length l_m , can be modeled as a capacitor (C_m), while the carrier fluid of mineral oil, having a length l_c , can be modeled as an inductor (L_c). The tuning mechanism depends on the variable capacitance (C_m) and inductance (L_c), whose values are determined by the relative position of the mercury to the microstrip patch, as shown in Figure 6.2. The moving of the mercury slug in the tube can be realized through a pressure-driven flow mechanism or using a micro pump. The reflection phases of the unit cell can be simulated using the WGS method in HFSS, in which the length of the mercury in the tube is changed gradually and the reflection phase is calculated. For proof of concept, the pressure-driven flow device which controls the moving of the mercury slug can be simplified and not included in the unit cell simulation.

Reference List

- [1] “IEEE standard definitions of terms for antennas,” *IEEE Std 145-1993*, pp. 1–32, April 2013.
- [2] C. A. Balanis, *Antenna theory: analysis and design*. John Wiley & Sons, 2012.
- [3] Y. Rahmat-Samii, “Reflector antennas,” in *Antenna Handbook*. Springer, 1988, pp. 949–1072.
- [4] J. Huang, *Reflectarray antenna*. Wiley Online Library, 2008.
- [5] D. Berry, R. Malech, and W. Kennedy, “The reflectarray antenna,” *Antennas and Propagation, IEEE Transactions on*, vol. AP-11, pp. 645–651, 1963.
- [6] D. M. Pozar, S. D. Targonski, and H. Syrigos, “Design of millimeter wave microstrip reflectarrays,” *Antennas and Propagation, IEEE Transactions on*, vol. 45, no. 2, pp. 287–296, 1997.
- [7] C. Malagisi, “Microstrip disc element reflect array,” in *EASCON’78; Electronics and Aerospace Systems Convention*, vol. 1, 1978, pp. 186–192.
- [8] H. R. Phelan, “Spiraphase reflectarray for multitarget radar,” *Microwave Journal*, vol. 20, p. 67, 1977.
- [9] T. Metzler and D. Schaubert, “Scattering from a stub loaded microstrip antenna,” in *Antennas and Propagation Society International Symposium, 1989. AP-S. Digest*. IEEE, 1989, pp. 446–449.
- [10] A. W. Robinson, M. E. Bialkowski, and H. J. Song, “An x-band passive reflect-array using dual-feed aperture-coupled patch antennas,” in *Microwave Conference, 1999 Asia Pacific*, vol. 3. IEEE, 1999, pp. 906–909.
- [11] E. Carrasco, M. Barba, and J. Encinar, “Aperture-coupled reflectarray element with wide range of phase delay,” *Electronics Letters*, vol. 42, no. 12, pp. 667–668, 2006.
- [12] J. Encinar and J. Zornoza, “Broadband design of three-layer printed reflectarrays,” *Antennas and Propagation, IEEE Transactions on*, vol. 51, no. 7, pp. 1662–1664, 2003.
- [13] D. Pozar and T. Metzler, “Analysis of a reflectarray antenna using microstrip patches of variable size,” *Electronics Letters*, vol. 29, no. 8, pp. 657–658, 1993.

- [14] M. E. Bialkowski and K. H. Sayidmarie, "Investigations into phase characteristics of a single-layer reflectarray employing patch or ring elements of variable size," *Antennas and Propagation, IEEE Transactions on*, vol. 56, no. 11, pp. 3366–3372, 2008.
- [15] D. M. Pozar and S. D. Targonski, "A microstrip reflectarray using crossed dipoles," in *Antennas and Propagation Society International Symposium, 1998. IEEE*, vol. 2. IEEE, 1998, pp. 1008–1011.
- [16] N. Misran, R. Cahill, and V. Fusco, "Design optimisation of ring elements for broadband reflectarray antennas," *IEE Proceedings-Microwaves, Antennas and Propagation*, vol. 150, no. 6, pp. 440–444, 2003.
- [17] J. Encinar, "Design of a dual frequency reflectarray using microstrip stacked patches of variable size," *Electronics Letters*, vol. 32, no. 12, pp. 1049–1050, 1996.
- [18] —, "Design of two-layer printed reflectarrays using patches of variable size," *Antennas and Propagation, IEEE Transactions on*, vol. 49, no. 10, pp. 1403–1410, 2001.
- [19] C. Han, C. Rodenbeck, J. Huang, and K. Chang, "A C/Ka dual frequency dual layer circularly polarized reflectarray antenna with microstrip ring elements," *IEEE Trans Antennas Propag*, vol. 52, no. 11, pp. 2871–2876, 2004.
- [20] S.-H. Hsu, C. Han, J. Huang, and K. Chang, "An offset linear-array-fed Ku/Ka dual-band reflectarray for planet cloud/precipitation radar," *IEEE Trans Antennas Propag*, vol. 55, no. 11, pp. 3114–3122, 2007.
- [21] J. Huang and R. Pogorzelski, "A ka-band microstrip reflectarray with elements having variable rotation angles," *Antennas and Propagation, IEEE Transactions on*, vol. 46, no. 5, pp. 650–656, 1998.
- [22] B. Subbarao, V. Srinivasan, V. Fusco, and R. Cahill, "Element suitability for circularly polarised phase agile reflectarray applications," in *Microwaves, Antennas and Propagation, IEE Proceedings*, vol. 151, no. 4. IET, 2004, pp. 287–292.
- [23] A. E. Martynyuk, J. Martinez Lopez, and N. A. Martynyuk, "Spiraphase-type reflectarrays based on loaded ring slot resonators," *Antennas and Propagation, IEEE Transactions on*, vol. 52, no. 1, pp. 142–153, 2004.
- [24] B. Strassner, C. Han, and K. Chang, "Circularly polarized reflectarray with microstrip ring elements having variable rotation angles," *Antennas and Propagation, IEEE Transactions on*, vol. 52, no. 4, pp. 1122–1125, 2004.

- [25] S. V. Hum, M. Okoniewski, and R. J. Davies, "Modeling and design of electronically tunable reflectarrays," *Antennas and Propagation, IEEE Transactions on*, vol. 55, no. 8, pp. 2200–2210, 2007.
- [26] M. Riel and J. Laurin, "Design of an electronically beam scanning reflectarray using aperture-coupled elements," *Antennas and Propagation, IEEE Transactions on*, vol. 55, no. 5, pp. 1260–1266, 2007.
- [27] L. Boccia, G. Amendola, and G. Di Massa, "Performance improvement for a varactor-loaded reflectarray element," *Antennas and Propagation, IEEE Transactions on*, vol. 58, no. 2, pp. 585–589, 2010.
- [28] M. Barba, E. Carrasco, J. E. Page, and J. A. Encinar, "Electronic controllable reflectarray elements in x band," *Frequenz*, vol. 61, no. 9-10, pp. 203–206, 2007.
- [29] P. Dumon, C. Apert, D. Belot, T. Dousset, and C. Renard, "A novel reflectarray for smart x-band satellite antenna," in *Antennas and Propagation Society International Symposium, 2007 IEEE*. IEEE, 2007, pp. 5885–5888.
- [30] C. Liu and S. V. Hum, "An electronically tunable single-layer reflectarray antenna element with improved bandwidth," *Antennas and Wireless Propagation Letters, IEEE*, vol. 9, pp. 1241–1244, 2010.
- [31] J. Perruisseau-Carrier and A. Skriverviky, "Monolithic mems-based reflectarray cell digitally reconfigurable over a 360 phase range," *Antennas and Wireless Propagation Letters, IEEE*, vol. 7, pp. 138–141, 2008.
- [32] H. Rajagopalan, Y. Rahmat-Samii, and W. A. Imbriale, "Rf mems actuated reconfigurable reflectarray patch-slot element," *Antennas and Propagation, IEEE Transactions on*, vol. 56, no. 12, pp. 3689–3699, 2008.
- [33] J. P. Gianvittorio and Y. Rahmat-Samii, "Reconfigurable patch antennas for steerable reflectarray applications," *Antennas and Propagation, IEEE Transactions on*, vol. 54, no. 5, pp. 1388–1392, 2006.
- [34] W. Hu, R. Cahill, J. A. Encinar, R. Dickie, H. Gamble, V. Fusco, and N. Grant, "Design and measurement of reconfigurable millimeter wave reflectarray cells with nematic liquid crystal," *Antennas and Propagation, IEEE Transactions on*, vol. 56, no. 10, pp. 3112–3117, 2008.
- [35] C. Weil, S. Muller, P. Scheele, Y. Kryvoschapka, G. Lussem, P. Best, and R. Jakoby, "Ferroelectric-and liquid crystal-tunable microwave phase shifters," in *Microwave Conference, 2003. 33rd European*, vol. 3. IEEE, 2003, pp. 1431–1434.

- [36] R. R. Romanofsky, "Advances in scanning reflectarray antennas based on ferroelectric thin-film phase shifters for deep-space communications," *Proceedings of the IEEE*, vol. 95, no. 10, pp. 1968–1975, 2007.
- [37] M. Li, B. Yu, and N. Behdad, "Liquid-tunable frequency selective surfaces," *Microwave and Wireless Components Letters, IEEE*, vol. 20, no. 8, pp. 423–425, 2010.
- [38] B. J. Lei, A. Zamora, T. F. Chun, A. T. Ohta, and W. A. Shiroma, "A wide-band, pressure-driven, liquid-tunable frequency selective surface," *IEEE microwave and wireless components letters*, vol. 21, no. 9, pp. 465–467, 2011.
- [39] J. A. Encinar and J. A. Zornoza, "Three-layer printed reflectarrays for contoured beam space applications," *Antennas and Propagation, IEEE Transactions on*, vol. 52, no. 5, pp. 1138–1148, 2004.
- [40] J. A. Zornoza, R. Leberer, J. A. Encinar, and W. Menzel, "Folded multi-layer microstrip reflectarray with shaped pattern," *Antennas and Propagation, IEEE Transactions on*, vol. 54, no. 2, pp. 510–518, 2006.
- [41] J. A. Encinar, L. S. Datashvili, J. A. Zornoza, M. Arrebola, M. Sierra-Castañer, J. L. Besada-Sanmartin, H. Baier, and H. Legay, "Dual-polarization dual-coverage reflectarray for space applications," *Antennas and Propagation, IEEE Transactions on*, vol. 54, no. 10, pp. 2827–2837, 2006.
- [42] A. Trastoy, F. Ares, and E. Moreno, "Phase-only synthesis of non-/spl phi/-symmetric patterns for reflectarray antennas with circular boundary," *Antennas and Wireless Propagation Letters, IEEE*, vol. 3, no. 1, pp. 246–248, 2004.
- [43] J. Encinar, L. Datashvili, H. Baier, M. Arrebola, M. Sierra-Castaner, J. Besada, H. Legay, and G. Toso, "Breadboard of a three-layer printed reflectarray for dual polarisation and dual coverage," in *Proc. 28th ESA Antenna Workshop on Space Antenna Systems and Techniques, Noordwijk, The Netherlands*, vol. 31, 2005, pp. 443–448.
- [44] M. Arrebola, J. A. Encinar, and M. Barba, "Multifed printed reflectarray with three simultaneous shaped beams for lmds central station antenna," *Antennas and Propagation, IEEE Transactions on*, vol. 56, no. 6, pp. 1518–1527, 2008.
- [45] L. L. MIT. Multimission phased-array radar (MPAR). [Online]. Available: <http://www.ll.mit.edu/mission/aviation/faawxsystems/mpar.html>

- [46] N. NOAA. Multi-function phased array radar (*MPAR*). [Online]. Available: <http://www.nssl.noaa.gov/tools/radar/mpar/>
- [47] G. Zhang, R. J. Doviak, D. S. Zrnic, R. Palmer, L. Lei, and Y. Al-Rashid, "Polarimetric phased-array radar for weather measurement: A planar or cylindrical configuration?" *Journal of Atmospheric and Oceanic Technology*, vol. 28, no. 1, pp. 63–73, 2011.
- [48] Y. Zhang, Y. Pan, S. Wang, Q. Zhao, D. Zrnic, and R. J. Doviak, "Reconfigurable and scalable array element design for polarimetric multifunctional par," in *Radar Conference (RADAR), 2011 IEEE*. IEEE, 2011, pp. 175–179.
- [49] S. Perera, Y. Pan, Q. Zhao, Y. Zhang, D. Zmic, and R. Doviak, "A fully reconfigurable polarimetric phased array testbed: Antenna integration and initial measurements," in *Phased Array Systems Technology, 2013 IEEE International Symposium on*, Oct 2013, pp. 799–806.
- [50] R. D. Palmer, "Status report on the development of the *CPPAR* demonstrator," 2013. [Online]. Available: <http://www.ofcm.noaa.gov/wg-mpar/meetings/2013-03/04%20CPPAR.pdf>
- [51] S. Perera, Y. Pan, Y. Zhang, X. Yu, D. Zrnic, and R. J. Doviak, "A fully reconfigurable polarimetric phased array antenna testbed," *International Journal of Antennas and Propagation*, vol. 2014, 2014.
- [52] A. Kelkar, "Flaps: conformal phased reflecting surfaces," in *Radar Conference, 1991., Proceedings of the 1991 IEEE National*. IEEE, 1991, pp. 58–62.
- [53] J. Huang, "Bandwidth study of microstrip reflectarray and a novel phased reflectarray concept," in *Antennas and Propagation Society International Symposium, 1995. AP-S. Digest*, vol. 1. IEEE, 1995, pp. 582–585.
- [54] Y. Pan, Y. Zhang, and S. Karimkashi, "Broadband low-cost reflectarray for multi-mission radar applications," in *Radar Conference (RADAR), 2012 IEEE*, May 2012, pp. 0613–0617.
- [55] D. Pozar, "Bandwidth of reflectarrays," *Electronics Letters*, vol. 39, no. 21, pp. 1490–1491, 2003.
- [56] M. E. Bialkowski and K. H. Sayidmarie, "Bandwidth considerations for a microstrip reflectarray," *Progress In Electromagnetics Research B*, vol. 3, pp. 173–187, 2008.
- [57] K.-L. Wong, *Compact and broadband microstrip antennas*. Wiley. com, 2004, vol. 168.

- [58] L. J. Chu, "Physical limitations of omni-directional antennas," *Journal of applied physics*, vol. 19, no. 12, pp. 1163–1175, 1948.
- [59] J. R. James, P. S. Hall, and C. Wood, *Microstrip antenna*. IET, 1981.
- [60] S. Long and M. Walton, "A dual-frequency stacked circular-disc antenna," *Antennas and Propagation, IEEE Transactions on*, vol. 27, no. 2, pp. 270–273, 1979.
- [61] A. Henderson, J. James, and C. Hall, "Bandwidth extension techniques in printed conformal antennas," in *Military Microwaves' 86*, vol. 1, 1986, pp. 329–334.
- [62] D. M. Pozar and B. Kaufman, "Increasing the bandwidth of a microstrip antenna by proximity coupling," *Electronics Letters*, vol. 23, no. 8, pp. 368–369, 1987.
- [63] C.-K. Wu and K.-L. Wong, "Broadband microstrip antenna with directly coupled and parasitic patches," *Microwave and Optical Technology Letters*, vol. 22, no. 5, pp. 348–349, 1999.
- [64] T. M. Au and K. M. Luk, "Effect of parasitic element on the characteristics of microstrip antenna," *Antennas and Propagation, IEEE Transactions on*, vol. 39, no. 8, pp. 1247–1251, 1991.
- [65] K. Tong, T. Au, K. Luk, and K. Lee, "Two-layer five-patch broadband microstrip antennas," *Electronics Letters*, vol. 31, no. 19, pp. 1621–1622, 1995.
- [66] N. Herscovici, "A wide-band single-layer patch antenna," *Antennas and Propagation, IEEE Transactions on*, vol. 46, no. 4, pp. 471–474, 1998.
- [67] R. Jedlicka, M. Poe, and K. Carver, "Measured mutual coupling between microstrip antennas," *Antennas and Propagation, IEEE Transactions on*, vol. 29, no. 1, pp. 147–149, 1981.
- [68] R. D. Javor, X.-D. Wu, and K. Chang, "Design and performance of a microstrip reflectarray antenna," *Antennas and Propagation, IEEE Transactions on*, vol. 43, no. 9, pp. 932–939, 1995.
- [69] F. Venneri, G. Angiulli, and G. Di Massa, "Design of microstrip reflect array using data from isolated patch analysis," *Microwave and Optical Technology Letters*, vol. 34, no. 6, pp. 411–414, 2002.
- [70] D. Pozar and D. H. Schaubert, "Analysis of an infinite array of rectangular microstrip patches with idealized probe feeds," *Antennas and Propagation, IEEE Transactions on*, vol. 32, no. 10, pp. 1101–1107, 1984.

- [71] D. M. Pozar, "Analysis of an infinite phased array of aperture coupled microstrip patches," *Antennas and Propagation, IEEE Transactions on*, vol. 37, no. 4, pp. 418–425, 1989.
- [72] D. Pozar, "Microstrip reflectarrays myths and realities," in *JINA, International Symposium on Antennas*, 2004, pp. 175–179.
- [73] F. Tsai and M. Bialkowski, "Designing a 161-element ku-band microstrip reflectarray of variable size patches using an equivalent unit cell waveguide approach," *Antennas and Propagation, IEEE Transactions on*, vol. 51, no. 10, pp. 2953–2962, 2003.
- [74] S. Targonski and D. Pozar, "Analysis and design of a microstrip reflectarray using patches of variable size," in *Antennas and Propagation Society International Symposium, 1994. AP-S. Digest*, vol. 3. IEEE, 1994, pp. 1820–1823.
- [75] S. Orfanidis, *Electromagnetic Waves and Antennas*, 2002. [Online]. Available: <http://www.ece.rutgers.edu/orfanidi/ewa/>
- [76] J. Huang, "Analysis of a microstrip reflectarray antenna for microspacecraft applications," *TDA Progress Report*, pp. 153–173, 1995.
- [77] CST. [Online]. Available: www.cst.com
- [78] —, "Electrically large applications and integral equation solver." [Online]. Available: <https://www.cst.com/Content/Events/UGM2009/6-1-3-Electrically-Large-Applications-and-Integral-Equation-solver.pdf>
- [79] L. Greengard and V. Rokhlin, "A new version of the fast multipole method for the laplace equation in three dimensions," *Acta numerica*, vol. 6, pp. 229–269, 1997.
- [80] W. C. Chew, J.-M. Jin, C.-C. Lu, E. Michielssen, and J. M. Song, "Fast solution methods in electromagnetics," *Antennas and Propagation, IEEE Transactions on*, vol. 45, no. 3, pp. 533–543, 1997.
- [81] J. Song, C.-C. Lu, and W. C. Chew, "Multilevel fast multipole algorithm for electromagnetic scattering by large complex objects," *Antennas and Propagation, IEEE Transactions on*, vol. 45, no. 10, pp. 1488–1493, 1997.
- [82] W. Rusch, "The current state of the reflector antenna art," *IEEE Trans. Antennas and Propag.*, vol. 32, no. 4, pp. 313–329, 1984.
- [83] W. Rusch, L. Welch, and G. Mires, "Observation-point-dependent blocking shadows on a reflector antenna," *IEEE Trans. Antennas and Propag.*, vol. 37, no. 6, pp. 690–697, 1989.

- [84] A. Moldsvor and P. Kildal, "Analysis of aperture blockage in reflector antennas by using obstacle-located blockage currents," *IEEE Trans. Antennas and Propag.*, vol. 40, no. 1, pp. 100–102, 1992.
- [85] Y. Pan and Y. Zhang, "Analysis of blockage effects in a center-fed reflectarray," *Microwave and Optical Technology Letters*, vol. 55, no. 8, pp. 1921–1926, 2013.
- [86] H. Haddad, J. Hanlen, and R. Munson, "Microstrip reflectarray for satellite communication and radar cross-section enhancement or reduction," Aug. 4 1987, uS Patent 4,684,952. [Online]. Available: <https://www.google.com/patents/US4684952>
- [87] Y. J. Guo and S. K. Barton, "Phase correcting zonal reflector incorporating rings," *Antennas and Propagation, IEEE Transactions on*, vol. 43, no. 4, pp. 350–355, 1995.
- [88] R. J. Doviak and D. S. Zrnic, *Doppler radar and weather observations*. Dover Publications, 2006.
- [89] D. Zrnic, V. Melnidov, and R. Doviak, "Issues and challenges for polarimetric measurement of weather with an agile beam phased array radar," *NOAA/NSSL report*, 117 pp., 2012.
- [90] D. Zrnic, R. Doviak, G. Zhang, and A. Ryzhkov, "Bias in differential reflectivity due to cross coupling through the radiation patterns of polarimetric weather radars." *Journal of Atmospheric & Oceanic Technology*, vol. 27, no. 10, 2010.
- [91] Y. Pan and Y. Zhang, "A reflectarray design with gapped ring elements and reduced cross-polarization for polarimetric radar," in *Phased Array Systems Technology, 2013 IEEE International Symposium on*, Oct 2013, pp. 124–128.
- [92] Y. Pan, Y. Zhang, and X. Yu, "A reflectarray design with reduced cross-polarization for polarimetric radar," *Microwave and Optical Technology Letters*, vol. 56, no. 8, pp. 1879–1883, 2014.
- [93] Antenna theory. [Online]. Available: <http://www.antenna-theory.com/>
- [94] A. Ludwig, "The definition of cross polarization," *IEEE Transactions on Antennas and Propagation*, vol. 21, no. 1, pp. 116–119, 1973.
- [95] I. Koffman, "Feed polarization for parallel currents in reflectors generated by conic sections," *Antennas and Propagation, IEEE Transactions on*, vol. 14, no. 1, pp. 37–40, 1966.

- [96] G. Knittel, “Comments on “the definition of cross polarization”,” *Antennas and Propagation, IEEE Transactions on*, vol. 21, no. 6, pp. 917–918, 1973.
- [97] Y. Rahmat-Samii, “Single patch and sixteen-element array antenna design for polarimetric radar at S band,” in *Project Report to University of Oklahoma, Antenna Research, Analysis and Measurement Laboratory (ARAM), UCLA*, January 2012.
- [98] D.-C. Chang and M.-C. Huang, “Multiple-polarization microstrip reflectarray antenna with high efficiency and low cross-polarization,” *Antennas and Propagation, IEEE Transactions on*, vol. 43, no. 8, pp. 829–834, 1995.
- [99] H. Hasani, M. Kamyab, and A. Mirkamali, “Low cross-polarization reflectarray antenna,” *Antennas and Propagation, IEEE Transactions on*, vol. 59, no. 5, pp. 1752–1756, 2011.
- [100] E. Carrasco, J. Encinar, M. Barba, R. Vincenti, and R. Sorrentino, “Dual-polarization reflectarray elements for ku-band tx/rx portable terminal antenna,” in *Antennas and Propagation (EuCAP), 2010 Proceedings of the Fourth European Conference on*, 2010, pp. 1–5.
- [101] C. Tienda, J. A. Encinar, M. Barba, and M. Arrebola, “Reduction of cross-polarization in offset reflectarrays using two layers of varying-sized patches,” *Microwave and Optical Technology Letters*, vol. 54, no. 11, pp. 2449–2454, 2012.
- [102] K. Chang, L.-H. Hsieh, and J. Wiley, *Microwave ring circuits and related structures*. J. Wiley, 2004.
- [103] M. Hajian, B. Kuijpers, K. Buisman, A. Akhnoukh, M. Plek, L. de Vreede, J. Zijdeveld, and L. Ligthart, “Reconfigurable scan-beam hollow patch reflectarray antenna loaded with tunable capacitor,” *Microwave and Optical Technology Letters*, vol. 51, no. 2, pp. 367–374, 2009.
- [104] M. Zawadzki and J. Huang, “A dual-band reflectarray for X and Ka bands,” 2003.
- [105] M. R. Chaharmir, J. Shaker, N. Gagnon, and D. Lee, “Design of broadband, single layer dual-band large reflectarray using multi open loop elements,” *IEEE Trans Antennas Propag*, vol. 58, no. 9, pp. 2875–2883, 2010.
- [106] Y. Pan, Y. Zhang, and X. Yu, “A X/Ku dual-band reflectarray design with cosecant squared shaped beam,” *Microwave and Optical Technology Letters*, vol. 56, no. 9, pp. 2028–2034, 2014.

- [107] R. Voges and J. Butler, "Phase optimization of antenna array gain with constrained amplitude excitation," *Antennas and Propagation, IEEE Transactions on*, vol. 20, no. 4, pp. 432–436, 1972.
- [108] H. Steyskal, "Simple method for pattern nulling by phase perturbation," *IEEE Transactions on Antennas and Propagation*, vol. 31, pp. 163–166, 1983.
- [109] F. Watanabe, N. Goto, A. Nagayama, and G. Yoshida, "A pattern synthesis of circular arrays by phase adjustment," *Antennas and Propagation, IEEE Transactions on*, vol. 28, no. 6, pp. 857–863, 1980.
- [110] J. F. DeFord and O. P. Gandhi, "Phase-only synthesis of minimum peak sidelobe patterns for linear and planar arrays," *Antennas and Propagation, IEEE Transactions on*, vol. 36, no. 2, pp. 191–201, 1988.
- [111] F. K. Povolotsky and T. P. Sydorova, "Phase synthesis of antennas for a given radiation pattern in one plane using piecewise linear aperture phase distribution," *Antennas and Propagation, IEEE Transactions on*, vol. 47, no. 9, pp. 1449–1453, 1999.
- [112] K. Hirasawa, "The application of a biquadratic programming method to phase only optimization of antenna arrays," *Antennas and Propagation, IEEE Transactions on*, vol. 36, no. 11, pp. 1545–1550, 1988.
- [113] A. Trastoy, F. Ares, and E. Moreno, "Phase-only control of antenna sum and shaped patterns through null perturbation," *Antennas and Propagation Magazine, IEEE*, vol. 43, no. 6, pp. 45–54, 2001.
- [114] A. Kondrat'ev and A. Khzmalyan, "Phase-only synthesis of antenna arrays for a given amplitude radiation pattern," *Journal of communications technology & electronics*, vol. 41, no. 10, pp. 859–866, 1996.
- [115] L. I. Vaskelainen, "Phase synthesis of conformal array antennas," *Antennas and Propagation, IEEE Transactions on*, vol. 48, no. 6, pp. 987–991, 2000.
- [116] G. M. Kautz, "Phase-only shaped beam synthesis via technique of approximated beam addition," *Antennas and Propagation, IEEE Transactions on*, vol. 47, no. 5, pp. 887–894, 1999.
- [117] O. M. Bucci, G. D'Elia, G. Mazzarella, and G. Panariello, "Antenna pattern synthesis: A new general approach," *Proceedings of the IEEE*, vol. 82, no. 3, pp. 358–371, 1994.
- [118] O. Bucci and G. D'elia, "Power synthesis of reconfigurable conformal arrays with phase-only control," *IEE Proceedings-Microwaves, Antennas and Propagation*, vol. 145, no. 1, pp. 131–136, 1998.

- [119] O. Bucci, G. Franceschetti, G. Mazzarella, and G. Panariello, "Intersection approach to array pattern synthesis," in *Microwaves, Antennas and Propagation, IEE Proceedings H*, vol. 137, no. 6. IET, 1990, pp. 349–357.
- [120] O. M. Bucci, G. Mazzarella, and G. Panariello, "Reconfigurable arrays by phase-only control," *Antennas and Propagation, IEEE Transactions on*, vol. 39, no. 7, pp. 919–925, 1991.
- [121] D. Pozar, S. Targonski, and R. Pokuls, "A shaped-beam microstrip patch reflectarray," *Antennas and Propagation, IEEE Transactions on*, vol. 47, no. 7, pp. 1167–1173, 1999.
- [122] A. Chakraborty, B. Das, and G. Sanyal, "Determination of phase functions for a desired one-dimensional pattern," *IEEE Trans Antennas Propag*, vol. 29, no. 3, pp. 502–506, 1981.
- [123] —, "Beam shaping using nonlinear phase distribution in a uniformly spaced array," *IEEE Trans Antennas Propag*, vol. 30, no. 5, pp. 1031–1034, 1982.
- [124] J. D. Barrera and G. H. Huff, "An adaptive siw filter using vertically-orientated fluidic material perturbations," in *Adaptive Hardware and Systems (AHS), 2010 NASA/ESA Conference on*. IEEE, 2010, pp. 205–208.

Appendix A

List of Acronyms and Abbreviations

ARRC	Advanced Radar Research Center
AUT	Antenna Under Test
CPAD	Configurable Phased Array Demonstrator
CPPAR	Cylindrical Polarimetric Phased Array Radar
DLB	Data-link Blockage
DBS	Direct Broadcast Satellite
EM	Electromagnetic
FSS	Frequency Selective Surfaces
GBSAA	Ground Based Sense and Avoid
HPBW	Half Power Beamwidth
IB	Integrated Blockage
LC	Liquid Crystal
LMDS	Local Multipoint Distribution Service
MAP	Method of Approximation Programming
MEMS	Micro Electro Mechanical Systems
MLFMM	Multilevel Fast Multi-pole Method
MPAR	Multi-functional Phased Array Radars
MS	Master and Slave
OLB	Obstacle Located Blockage
PTFE	Polytetrafluoroethylene
RCS	Radar Cross Section

RF	Radio Frequency
RLB	Reflectarray Located Blockage
SLL	Sidelobe Levels
TR	Transmit Receive
VSWR	Voltage Standing Wave Ratio
WGS	Waveguide Simulation
ZB	Zero Blockage